

DEPARTMENT OF PHYSICS, UNIVERSITY OF JYVÄSKYLÄ  
RESEARCH REPORT No. ??/2019

**JET TRANSVERSE MOMENTUM DISTRIBUTIONS  
FROM RECONSTRUCTED JETS  
IN P-PB COLLISIONS AT  $\sqrt{s_{\text{NN}}} = 5.02 \text{ TeV}$**

**BY  
TOMAS SNELLMAN**

Academic Dissertation  
for the Degree of  
Doctor of Philosophy

*To be presented, by permission of the Faculty of Mathematics and Natural Sciences  
of the University of Jyväskylä, for public examination in Auditorium FYS 1  
of the University of Jyväskylä on June 19th, 2019, at 12 o'clock noon*



Jyväskylä, Finland  
June 2019

# Personal Contribution

Snellman, Tomas

Jet transverse momentum distributions from reconstructed jets in p–Pb collisions at  $\sqrt{s_{\text{NN}}} = 5.02$  TeV

Jyväskylä; University of Jyväskylä, 2019, ...

Department of Physics Research Report No. xx/2019

ISSN

ISBN

ISBN

**Keywords:** jet, jet shape, jet fragmentation, jet reconstruction, heavy ion, p–Pb, transverse momentum, ALICE, CERN, LHC

The main contributions of the author to the research presented in this thesis are listed below

- Jet fragmentation transverse momentum ( $j_T$ ) analysis for  $\sqrt{s_{\text{NN}}} = 5.02$  TeV p–Pb data
  - Implementation of the observable ( $j_T$ ) for jet analysis
  - Implementation and improvement of the perpendicular cone background method
  - Developing the random background method
  - Performing unfolding of detector effects on the data
  - Systematic uncertainty evaluation
  - Repetition of the analysis with PYTHIA and HERWIG Monte Carlo generators and comparison of model results and data
  - Comparison of results to  $j_T$  extracted from two-particle correlations
- Quality assurance (QA) of the Gas Electron Multiplier (GEM) foils that are built into the Time Projection Chamber (TPC) detector of the ALICE experiment. The work was performed at the Helsinki Institute of Physics.
- At CERN contributing to the maintenance of the level-0 trigger of the electromagnetic calorimeter at the ALICE experiment

<b>Author</b>	Tomas Snellman University of Jyväskylä Finland
<b>Supervisors</b>	Dr. Kim Dong Jo University of Jyväskylä Finland
	Prof. Jan Rak University of Jyväskylä Finland
<b>Reviewers</b>	Prof. Stefan Bathe Baruch College, CUNY USA
	Prof. Marcin Chrząszcz Instytut Fizyki Jądrowej PAN Poland
<b>Opponent</b>	Prof. Jamie Nagle University of Colorado Boulder USA

*In memory of my father*

## Acknowledgements

The work presented in this thesis has been carried out between 2014 and 2019 at the University of Jyväskylä, at the University of Helsinki and at CERN. I would like to open my thesis by acknowledging the help I have received from several directions which has made my graduation possible.

First, I thank my supervisors Dong Jo Kim and Jan Rak. Dong Jo for his continued guidance and patience and Jan for giving me the opportunity to work in this field.

Additionally from our research group I would like to highlight Sami Räsänen for his help in both practical and physics matters and providing feedback to my thesis. I would also like to thank all present and past members of the ALICE Jyväskylä group for providing a supportive working environment.

For helping me get acquainted with the ALICE EMCal trigger maintenance work I am grateful to Jussi Viinikainen and Martin Poghoysan.

I would also like to acknowledge the support to finalising my analysis from the Jet Physics Working Group, especially Leticia Cunqueiro Mendez, Tatsuya Chujo and Marco van Leeuwen.

I would like to thank the personnel of the Helsinki Institute of Physics detector laboratory for a pleasant working environment during my time in Helsinki and especially Erik Brückner, Timo Hildén and Essi Kangasaho for guiding me through the GEM quality assurance responsibilities.

I am grateful to Stefan Bathe and Marcin Chrząszcz for reviewing my thesis and providing useful comments and Jamie Nagle for agreeing to be my opponent.

A special thanks goes to my family for all the support I have received both before and during my academic career. Without my parents none of this would have been possible.

Finally I would like to acknowledge the financial support I have received from the University of Jyväskylä and the Helsinki Institute of Physics.

Jyväskylä, June 2019  
Tomas Snellman

# Contents

## Personal Contribution

### Acknowledgements

### Contents

<b>1</b>	<b>Introduction</b>	<b>1</b>
1.1	Quantum chromodynamics . . . . .	3
1.1.1	Foundation of QCD . . . . .	3
1.1.2	Asymptotic Freedom . . . . .	6
1.2	Heavy-ion physics . . . . .	9
1.3	Features of heavy-ion collisions . . . . .	11
1.3.1	Collision Geometry . . . . .	11
1.3.2	Collective motion . . . . .	15
1.4	Hard processes . . . . .	22
1.4.1	pQCD factorization . . . . .	22
1.4.2	Jet showering . . . . .	24
1.4.3	Soft gluon radiation and angular ordering . . . . .	25
1.4.4	Jet hadronisation . . . . .	27
1.4.5	Interactions between jet and medium . . . . .	31
1.4.6	New paradigm of jet Quenching . . . . .	35
1.5	QGP in Small systems . . . . .	40
1.5.1	Collective phenomena . . . . .	40
1.5.2	Absence of jet quenching . . . . .	41
1.5.3	Centrality determination in small systems . . . . .	44
<b>2</b>	<b>Experimental Setup</b>	<b>47</b>
2.1	CERN . . . . .	47
2.2	Large Hadron Collider . . . . .	49
2.2.1	LHC experiments . . . . .	50
2.3	ALICE . . . . .	50

2.3.1	Tracking detectors . . . . .	52
2.3.2	TPC . . . . .	53
2.3.3	Particle identification . . . . .	54
2.3.4	Electromagnetic Calorimeters . . . . .	55
2.3.5	Forward and trigger detectors . . . . .	57
2.3.6	Muon spectrometer . . . . .	58
2.3.7	Triggers . . . . .	59
2.4	TPC upgrade . . . . .	60
2.4.1	ALICE upgrade during LS2 . . . . .	60
2.4.2	TPC upgrade . . . . .	61
<b>3</b>	<b>Event and track selection</b>	<b>64</b>
3.1	Event selection . . . . .	64
3.2	Track reconstruction . . . . .	64
3.3	Cluster selection . . . . .	68
<b>4</b>	<b>Analysis method</b>	<b>70</b>
4.1	Jet Finding . . . . .	70
4.1.1	Anti $k_T$ algorithm . . . . .	70
4.2	Definition of $j_T$ . . . . .	72
4.3	Unfolding detector effects . . . . .	74
4.3.1	Bayesian unfolding . . . . .	75
4.3.2	Pseudo-experiment Monte Carlo . . . . .	77
4.3.3	Pythia Response matrices . . . . .	78
4.3.4	Unfolding closure test . . . . .	79
4.4	Background . . . . .	83
4.4.1	Perpendicular cone background . . . . .	83
4.4.2	Random background . . . . .	85
4.5	Fitting . . . . .	86
<b>5</b>	<b>Systematic uncertainties</b>	<b>88</b>
5.1	Background . . . . .	88
5.2	Unfolding . . . . .	91
5.2.1	Effect of number of iterations . . . . .	91
5.2.2	Effect of different prior . . . . .	91
5.2.3	Effect of $p_T$ truncation . . . . .	91
5.3	Tracking . . . . .	94
5.4	EMCal clusters . . . . .	95
5.5	Summary of systematic uncertainties . . . . .	97

<b>6</b>	<b>Results</b>	<b>98</b>
6.1	High multiplicity events	101
<b>7</b>	<b>Discussions</b>	<b>103</b>
7.1	Comparing dihadron and jet $j_T$ results	103
7.1.1	Different $R$ parameters	105
7.1.2	Leading tracks versus jet as reference	106
<b>8</b>	<b>Summary</b>	<b>109</b>
<b>Appendices</b>		<b>111</b>
A	Commonly Used Abbreviations	112
B	Additional graphs	114

# Chapter 1

## Introduction

This thesis focuses on studying Quantum Chromodynamics (QCD) [1], a part of the standard model of particle physics [2], which is the theory describing the strong interactions. Strong interaction is the force responsible for interactions that holds the nucleus of an atom together. Fundamentally it describes the interactions between quarks and gluons, the elementary constituents of the building blocks of the nucleus, protons and neutrons. Because of specifics of this interaction quarks and gluons, together dubbed partons, can never be seen free [3]. Under ordinary conditions they are confined into bound states called hadrons. In extreme conditions they can form a medium of asymptotically free quarks and gluons, quark-gluon plasma (QGP) [4].

Indirectly partons can be observed in high energy particle collisions as jets, collimated showers of particles [5]. The physics of these jets is the primary topic discussed in this thesis. Understanding jets is important when one is interested in the processes that produce the partons that eventually fragment into jets. By themselves jets can provide an insight into QCD when the fragmentation is studied. Jets can also be used as probes of the QGP medium.

Experimentally jets can be studied with jet reconstruction algorithms which group observed tracks, in essence undoing the showering process, to find a reasonable estimate of the initial parton. That is also the case in this thesis. The main observable studied is the jet fragmentation transverse momentum  $j_T$  which is defined as the perpendicular component of the momentum of jet constituents with respect to the jet axis, the best estimate of the initial parton. As such  $j_T$  measures the transverse nudge that fragmentation products receive.

The analysis studies collisions between protons and lead nuclei. Originally these were meant to be a reference for lead-lead collisions to rule out possible cold nuclear matter effects [6]; effects caused by the regular 'cold' nuclear matter of a nucleus as opposed to QGP. However, p–Pb collisions have provided interesting physics by themselves. Many of the collective phenomena that in Pb–Pb collisions were

attributed to QGP have been observed also in high multiplicity p–Pb collisions [7] and even in ultra high multiplicity pp collisions [7]. However observables of jet modification show no conclusive signals in p–Pb collisions [6, 7].

This thesis is organised as follows: Section 1 first gives a general introduction into the history and properties of QCD and heavy-ion physics. It is followed by a description of hard processes, jet fragmentation and hadronisation and how these processes might look like in a heavy-ion environment. Finally there is a discussion on the physics of small systems.

The experimental setup that was used to collect the data in this thesis is described in Section 2. It starts by explaining the accelerator facilities at CERN and LHC in more detail. This is followed by a description of the ALICE experiment and its sub-detectors. A part of Section 2 is dedicated to coming upgrades of ALICE as this is a timely topic. In 2019-2020 ALICE will be upgraded and I have made a personal contribution to the TPC upgrade.

Section 3 gives a description of the event, track and cluster selection criteria used in the analysis. This is followed in Section 4 by the specific analysis methods used in this thesis. First the jet reconstruction algorithm used, anti- $k_T$ , is described. Section 4 continues by introducing the  $j_T$  observable, how it is obtained and what methods are used to estimate background contribution and correct for detector effects. Finally the fitting method used for the final results is described. Section 5 gives the different systematic uncertainties that arise from the analysis.

Finally the results from the analysis are presented in Section 6. The results are compared to PYTHIA and Herwig Monte Carlo generators. Further discussion of the results is given in Section 7 when the results are compared to  $j_T$  results obtained with a different analysis method. Section 8 summarises the main results and gives an outlook for future.

## 1.1 Quantum chromodynamics

### 1.1.1 Foundation of QCD

The universe is governed by four basic interactions: gravity, electromagnetic, weak and strong interactions. Gravity is best described by the theory of general relativity [8]. The standard model of particle physics [2] includes the remaining three interactions, electromagnetic, weak and strong interactions. The standard model is a quantum field theory where local gauge symmetries dictate particle interactions [5].

The first interaction included in the standard model was the electromagnetic interaction. The foundations of quantum field theory and Quantum Electrodynamics (QED) were already laid out by the work by Dirac in 1927 [9]. The full theory of QED was formulated in 1946-1949 by Tomonaga [10], Schwinger [11, 12] and Feynman [13]

Motivated by the success of a quantum field theory approach for the electromagnetic interaction physicists started working on the remaining interactions. However, the weak and strong nuclear interactions proved more challenging to formulate [14]. In the end the weak interaction was unified with the electromagnetic interaction into the electroweak theory. The final theory was formulated by Glashow [15], Salam [16] and Weinberg [17].

The theory of strong interactions became to be known as Quantum Chromodynamics (QCD). The search for a theory of strong interactions began already after the formulation of QED and drew further inspiration when new particle accelerators were introduced in the 1950s. These were powerful enough to conduct particle physics research while before this the main source of particle physics had been the study of cosmic rays. From cosmic ray studies positrons, neutrons and muons had been discovered in the 1930s and charged pions were discovered in 1947 [18, 19]. The neutral pion was discovered in 1950 [20].

These new accelerators included the Bevalac accelerator which was commissioned at the Lawrence Berkeley National Laboratory (LBNL) in 1954. Bevalac was followed by the Super Proton Synchrotron (SPS) at CERN in 1959 and by the Alternating Gradient Synchrotron (AGS) at the Brookhaven National Laboratory (BNL) in 1960. The most powerful of these was the AGS which could reach energies of up to 33 GeV with proton beams. With these accelerators a host of new particles were discovered by the beginning of the 1960s. The most notable were antiprotons [21], antineutrons [22],  $\Delta$ -particles and the six hyperons ( $\Xi^0$  [23],  $\Xi^-$  [24],  $\Sigma^\pm$  [25],  $\Sigma^0$  [26] and  $\Lambda$  [27]).

Physicists started searching for symmetries between these newly observed particles. Already in 1932 Heisenberg [28] had used an SU(2) symmetry in his isospin model to group protons and neutrons, as apart from electrical charge these behave

almost identically. In 1962 this was extended by Gell-Mann and Ne’eman [29] to the SU(3) symmetry based organisation of particles. In this SU(3) model hadrons sharing the same spin and parity numbers were grouped into octets. This lead to the discovery of the  $\Omega^-$  [30] baryon as the SU(3) decouplet that included heavier baryons was missing a baryon.

In the SU(3) symmetry group the simplest representation is a triplet where particles would have electric charges  $2/3$  or  $-1/3$ . However, no particles with fractional charge had been detected. Although they still didn’t consider these to be real particles, Gell-Mann [31] and Zweig [32] proposed in 1964 that baryons and mesons would be bound states of these three hypothetical triplet particles. Now we know that these are the  $u$ ,  $d$  and  $s$  quarks. The term quark was coined by Gell-Mann while Zweig had called them aces.

This original quark model still had a problem as it violated the Pauli exclusion principle. Because of the antisymmetry of fermion wave functions no two similar fermions can share the exact same quantum numbers. However, in a particle comprised of three identical (same flavour) quarks, like the  $\Omega^-$  particle, at least two quarks would have the same quantum numbers, as the only variable quantum number, spin, can have two values for quarks with spin  $1/2$ . This problem was solved by the addition of another quantum number, colour, which separated quarks of the same species. The idea of colour had been originally presented already in 1964 by Greenberg [33]. A model combining quarks and colour was presented in 1971 by Gell-Mann and Fritzsch [34]. In the new colour model the baryonic wave function became

$$(qqq) \rightarrow (q_r q_g q_b - q_g q_r q_b + q_b q_r q_g - q_r q_b q_g + q_g q_b q_r - q_b q_g q_r), \quad (1.1)$$

Experimentally the colour model could be confirmed by observables like the decay rate of a neutral pion and the Drell-Ratio. When taking colour into account the neutral pion decay rate is

$$\Lambda(\pi^0 \rightarrow \gamma\gamma) = \frac{\alpha^2}{2\pi} \frac{N_c^2}{3^2} \frac{m_\pi^3}{f_\pi^2}, \quad (1.2)$$

where  $N_c$  is the number of colours,  $m_\pi$  is the mass of pion and  $f_\pi$  is the pion decay constant. For  $N_c = 3$  this decay rate is 7.75 eV while the measured value is  $(7.86 \pm 0.54)$  eV [35].

The Drell-Ratio  $D$  [36] combines both the colour information and the number of quarks species. Defined as

$$D = \frac{\sigma(e^+ + e^- \rightarrow \text{hadrons})}{\sigma(e^+ + e^- \rightarrow \mu^+ + \mu^-)} = N_c \sum_f Q_f^2, \quad (1.3)$$

where  $Q_f$  are the effective charges of individual quark flavours. This ratio has the numerical value 2 when the lightest quarks  $u$ ,  $d$  and  $s$  are included. For collision energies exceeding the threshold of heavy quark ( $c$  and  $b$ ) production processes the ratio increases to  $^{10}/_3$  (for  $f = u, d, s, c$ ) and  $^{11}/_3$  (for  $f = u, d, s, c, b$ ). So far the energy threshold ( $\sqrt{s} \approx 350$  GeV) of  $t\bar{t}$  production, has not been reached by any  $e^+e^-$  colliders.

In the colour model only colour neutral states are possible which explains why no free quarks had been observed. The simplest ways of producing a colour neutral object are the hadrons which can be observed, i.e. (anti)baryons and mesons, the combinations of either three (anti)quarks or a quark-antiquark pair respectively. Although the hunt for more exotic combinations has been going on for decades, only in 2019 did LHCb produce conclusive evidence of the observation of a pentaquark [37], a state which consists of 4 quarks and one antiquark.

First experimental indication of the existence of quarks came in 1969 when a series of experiments at the Stanford Linear Accelerator Center (SLAC) revealed that protons and neutrons appeared to have some substructure [38, 39]. For this discovery they eventually received the Nobel Prize in Physics in 1990 [40]. Bjorken demonstrated that these results could be explained if protons and neutrons were composed of virtually noninteracting pointlike particles [41, 42]. Feynman [43] interpreted these objects as real particles and suggested they would be the quarks of Gell-Mann's model. At the time, however, this seemed mysterious; if all strongly interacting particles, hadrons, were composed of quarks, then quarks should surely be strongly interacting themselves. Why would they appear to be almost free inside hadrons? This turned out to be a key clue in formulating the theory of strong interactions [14].

With the inclusion of colour the final quantum field theory of QCD could be formed rapidly between 1972-1974. A significant contribution was the work done by Gross, Wilczek, Politzer and George for non-abelian gauge field theories [1, 44–47]. The work showed that quarks would indeed be asymptotically free in a non-abelian theory, which explained the results from SLAC. In 2004 Gross, Wilczek and Politzer received the Nobel Prize in Physics for their work [48]. The role of gluons as the particles mediating the strong interaction was presented by Fritzsch, Gell-Mann and Leutwyler in 1973 [49].

The quark model was extended in 1974 when the discovery of the charm quark and the first charmed hadron,  $J/\Psi$ , was simultaneously published by teams from the SLAC [50], from Brookhaven National Laboratory [51] and from the ADONE collider in Frascati, Italy [52]. In 1976 the Nobel Prize in Physics was awarded to Richter and Ting for the discovery of the charm quark [53]. The existence of a fourth quark had already been speculated in 1964 by Bjorken and Glashow [54], but a proper prediction was provided by Glashow, Iliopoulos and Maiani in 1970 [15]

based on symmetries between leptons and quarks in weak interactions.

However, the mediating particles, gluons, had not been directly seen in any experiments. The existence could be inferred from observing that the quarks only carried about half of the momentum of protons [55]. Direct evidence was first seen in 1979 at the Positron-Electron Tandem Ring Accelerator (PETRA) at DESY [56–58] in the form of a three jet event, where the third jet came from a gluon.

The two remaining quarks, bottom and top, were introduced by Kobayashi and Maskawa in 1973 to explain CP-violation [59]. For this they received the Nobel Prize in Physics in 2008 [60]. Bottom quark was discovered soon after, in 1977, at Fermilab [61]. The heaviest quark, top quark, would eventually be discovered in 1995 by the CDF [62] and DØ [63] experiments at Fermilab.

### 1.1.2 Asymptotic Freedom

In Quantum Electrodynamics (QED) the vacuum becomes polarised in the vicinity of a charge. Virtual particle-antiparticle pairs populate the surroundings of the centre charge. The net effect is that the field at any finite distance is partially cancelled. Closer to the central charge one sees less of the vacuum effect and the effective charge increases. With increasing distance to the charge the effective charge weakens until the QED coupling constant reaches the fine-structure constant  $\alpha = \frac{1}{137}$  [5].

There is screening also in QCD because of the colour charges. However, as QCD is a non-abelian theory gluons can interact also with other gluons. The mediating particles of QED, photons, are neutral and thus can't interact with other photons. The self-interaction of gluons leads to the antiscreening of the colour charge which dominates over the screening effect. As the distance to the central charge increases, virtual gluons of the vacuum cause the coupling constant to grow larger. If the distance between colour charges, quarks, gets large enough the interaction is strong enough to produce a new quark-antiquark pair. Thus no free colour charges can be seen. On the other hand, at very small distances the coupling constant approaches zero. This is known as asymptotic freedom [5].

Extending the idea of asymptotic freedom Collins predicted in 1975 [64] a state where individual quarks and gluons would no longer be bound to hadrons. This state of bulk QCD matter, which can be seen as a separate phase of hadronic matter, was later coined Quark-Gluon Plasma (QGP) by Edward Shuryak in 1980 [4]. With some assumptions a phase diagram of hadronic matter can be drawn. Figure 1.1 shows a schematic view of this phase diagram.

At a time of  $10^{-6}$ s after the Big Bang the conditions in the early universe preferred the existence of QGP instead of hadronic matter. Nowadays the properties of QGP can be explored in laboratories, through collisions of heavy atomic nuclei

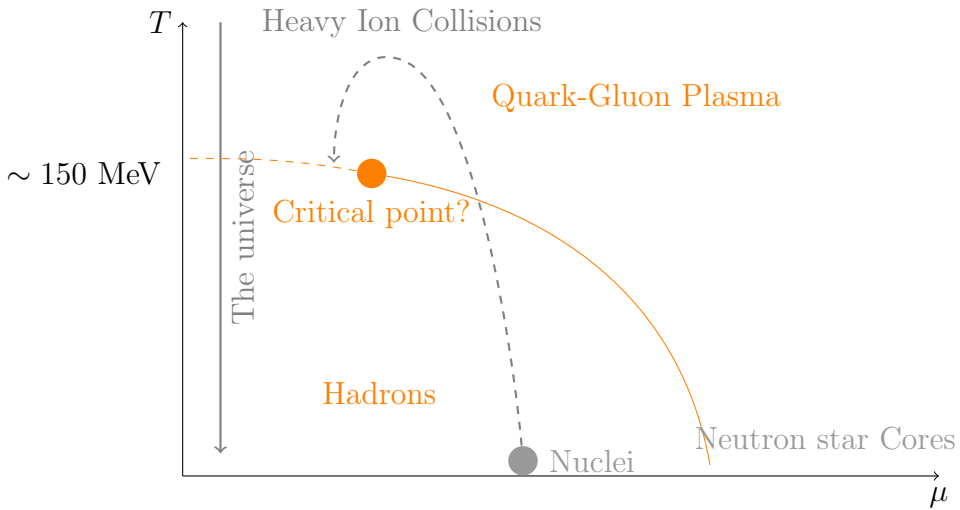


Figure 1.1: A schematic illustration of the phase diagram of QCD matter. The  $x$ -axis, showing the quark chemical potential  $\mu$ , represents the imbalance between quarks and antiquarks. Along the  $x$ -axis the temperature is zero. Along the vertical axis the temperature increases, which takes us through the crossover from a hadronic gas to quark-gluon plasma. With low  $\mu$  this is the regime explored by high-energy heavy-ion colliders and also the trajectory taken by the universe as it cooled after the Big Bang. The conditions in neutron stars correspond to the lower right corner, with low  $T$  and high  $\mu$ .

at ultra-relativistic energies. The phase transition between QGP and ordinary hadronic matter is the only phase transition in a quantum field theory that can be studied by any current or foreseeable technology. Thus the study of QGP in extreme conditions is of high interest.

One important property of QGP is the shear viscosity to entropy ratio,  $\eta/s$ . It is believed that among all substances in nature this ratio has a universal minimum value of  $1/4\pi \approx 0.08$ . In the strong coupling of certain gauge theories this is reached [65]. Figure 1.2 shows the temperature dependance of  $\eta/s$  for several substances. For all cases the  $\eta/s$  ratio has a minimum value in the vicinity of the critical temperature,  $T_c$  [66]. Therefore studying the  $\eta/s$  ratio in QGP matter could also probe the critical point of QCD matter.

In  $\sqrt{s_{NN}} = 200$  GeV Au–Au collisions at RHIC  $\eta/s$  has been estimated to be  $0.09 \pm 0.015$  [66], which suggests that at least at some point during the evolution the matter is close to the critical point of QCD.

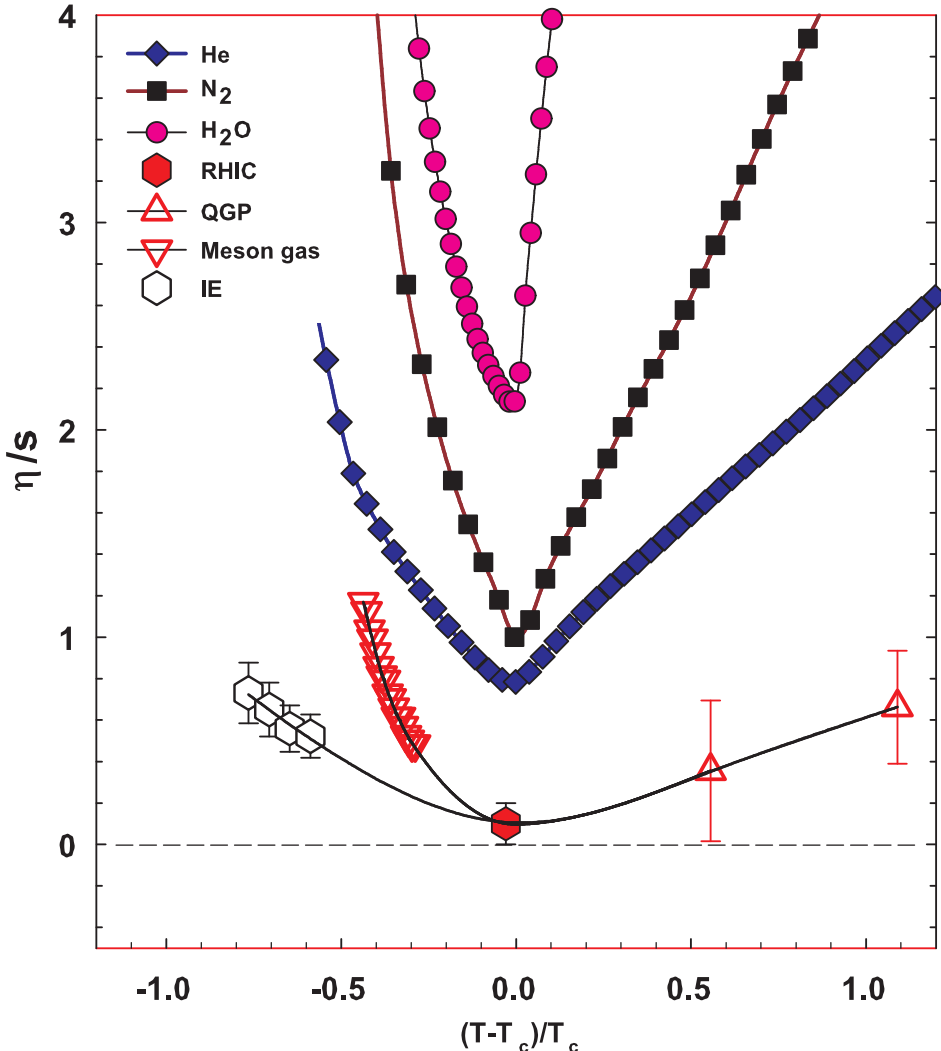


Figure 1.2: The figure shows  $\eta/s$  as a function of  $(T - T_c)/T_c$  for several substances as indicated. The lines are drawn to guide the eye. The  $\eta/s = 0.09 \pm 0.015$  value at RHIC is estimated from Au–Au collisions at  $\sqrt{s_{NN}} = 200$  GeV. The calculations assume a value  $T_c = 170$  MeV for nuclear matter. This figure has been reprinted from [66] with kind permission from the American Physical Society.

## 1.2 Heavy-ion physics

Quark Gluon Plasma (QGP) can be experimentally studied by colliding heavy-ions at high energies. Nowadays research of heavy-ion collisions is mainly performed at two particle colliders; The Relativistic Heavy-Ion Collider (RHIC) at BNL in New York, USA and the Large Hadron Collider (LHC) at CERN in Switzerland. Energy densities at these colliders are assumed to be large enough to produce QGP and indeed convincing evidence of QGP has been seen at both colliders. Complimentary research with heavy nuclei is also performed at the Super Proton Synchrotron (SPS) at CERN.

The first heavy-ion collisions were performed in fixed target experiments at the Bevalac experiment at the Lawrence Berkeley National Laboratory [67] and at the Joint Institute for Nuclear Research in Dubna [68], which reached energies of up to 1 GeV per nucleon. These were followed in 1986 by the Super Proton Synchrotron (SPS) at CERN which collided oxygen beams with fixed lead targets reaching a centre-of-mass energy per colliding nucleon pair ( $\sqrt{s_{NN}}$ ) of 19.4 GeV [69]. However, no decisive evidence of QGP was found in these initial experiments. In 1994 SPS introduced a heavier lead beam to produce Pb–Pb collisions at  $\sqrt{s_{NN}} \approx 17$  GeV. Simultaneously the Alternating Gradient Synchrotron (AGS) at BNL started colliding ions like  $^{32}\text{S}$  with a fixed target at energies of up to 28 GeV [70]. In 2000 CERN [71] presented compelling evidence for the existence of a new state of matter in SPS. Today SPS is used for fixed-target experiments with 400 GeV proton beams. One of these is the SPS heavy-ion and Neutrino Experiment (SHINE) [72], which tries to search for the critical point of strongly interacting matter.

The next significant addition was the Relativistic Heavy-Ion Collider (RHIC) at BNL in New York, USA which started operating in 2000 and keeps operating to this day. Instead of using fixed targets, RHIC can collide two accelerated beams, significantly increasing the potential centre-of-mass energy. In Au–Au collisions RHIC can reach a centre-of-mass energy per nucleon pair of 200 GeV. The experiments at RHIC have provided a lot of convincing evidence that QGP was created [73–76].

The newest addition to the group of heavy-ion accelerators is the Large Hadron Collider (LHC) at CERN, Switzerland. Primarily used for proton-proton collisions LHC started operating in November 2009. A year later, in November 2010, first Pb–Pb heavy-ion runs began at  $\sqrt{s_{NN}} = 2.76$  TeV. Since then LHC has provided both Pb–Pb and p–Pb collisions and a short period of Xe–Xe collisions. Table 1.1 shows a summary of these. Among the main experiments at LHC, ALICE (a Large Ion Collider Experiment) is dedicated to heavy-ion physics. The all-purpose nature of CMS (Compact Muon Solenoid) and ATLAS (a Toroidal LHC Apparatus) make them well suited also for many heavy-ion studies and they have active heavy-ion

programs. The fourth main experiment, LHCb, uses its SMOG system [77] to perform unique fixed target collisions with heavy ions, complementing the other experiments.

Table 1.1: Summary of datasets. The integrated luminosities are from ALICE.

Run 1 (2009-2013)			Run 2 (2015-2018)		
	pp	p–Pb	Pb–Pb	pp	p–Pb
pp	0.90 TeV	$\sim 200 \mu\text{b}^{-1}$		5.02 TeV	$\sim 1.3 \text{ pb}^{-1}$
	2.76 TeV	$\sim 100 \text{ nb}^{-1}$		13.00 TeV	$\sim 25 \text{ pb}^{-1}$
	7.00 TeV	$\sim 1.5 \text{ pb}^{-1}$		5.02 TeV	$\sim 3 \text{ nb}^{-1}$
	8.00 TeV	$\sim 2.5 \text{ pb}^{-1}$		8.16 TeV	$\sim 25 \text{ nb}^{-1}$
p–Pb	5.02 TeV	$\sim 15 \text{ nb}^{-1}$	Xe–Xe	5.44 TeV	$\sim 0.3 \mu\text{b}^{-1}$
Pb–Pb	2.76 TeV	$\sim 75 \mu\text{b}^{-1}$	Pb–Pb	5.02 TeV	$\sim 1 \text{ nb}^{-1}$

## 1.3 Features of heavy-ion collisions

### 1.3.1 Collision Geometry

Since atomic nuclei have a significant transverse size, a collision between nuclei has geometric properties that provide insight into the collision dynamics. One illustration of a heavy-ion collision is shown in Figure 1.3. The main defining parameter of a collision is the vector connecting the centres of the two colliding nuclei at their closest approach, which is known as the impact parameter  $\vec{b}$ .

The impact parameter with the beam direction defines the reaction plane, which has an angle  $\Psi_{RP}$  in the experimental reference frame, which is fixed by the detector setup. This reaction plane angle can be estimated with the event plane method [78] since particle production changes as a function of the angle with respect to the reaction plane.

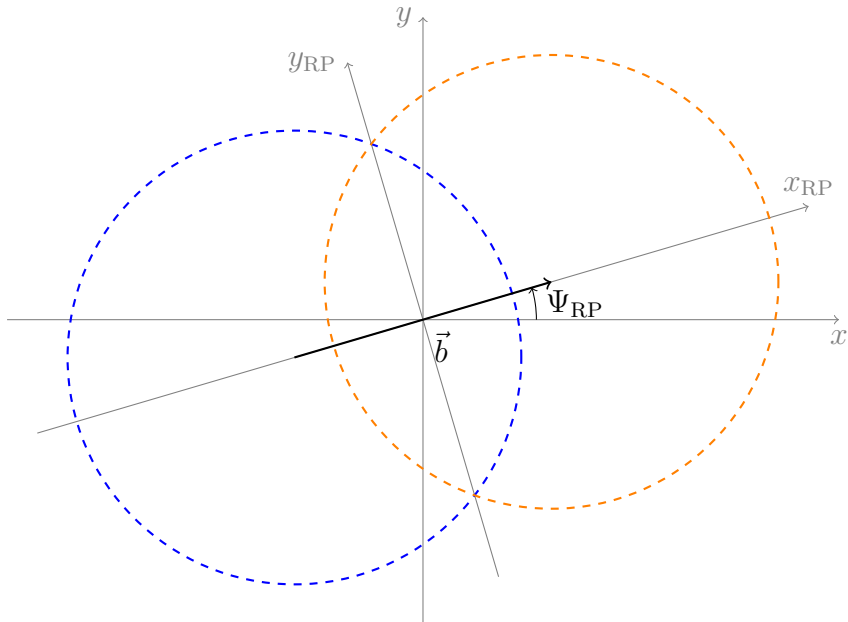


Figure 1.3: The definition of the impact parameter and the reaction plane. The  $x-y$  plane represents a coordinate system fixed by the experiment. The dashed circles are the two colliding nuclei.  $x_{RP}$  is the reaction plane and  $\Psi_{RP}$  gives its angle.

Although the length of the impact parameter can be used to quantise the centrality of a heavy-ion collisions in theoretical models, it is not practical in an experimental setup. Any connections between  $\vec{b}$  and experimental observables is model-dependent. For a comparison of results between different experiments and models, one needs a general definition for centrality.

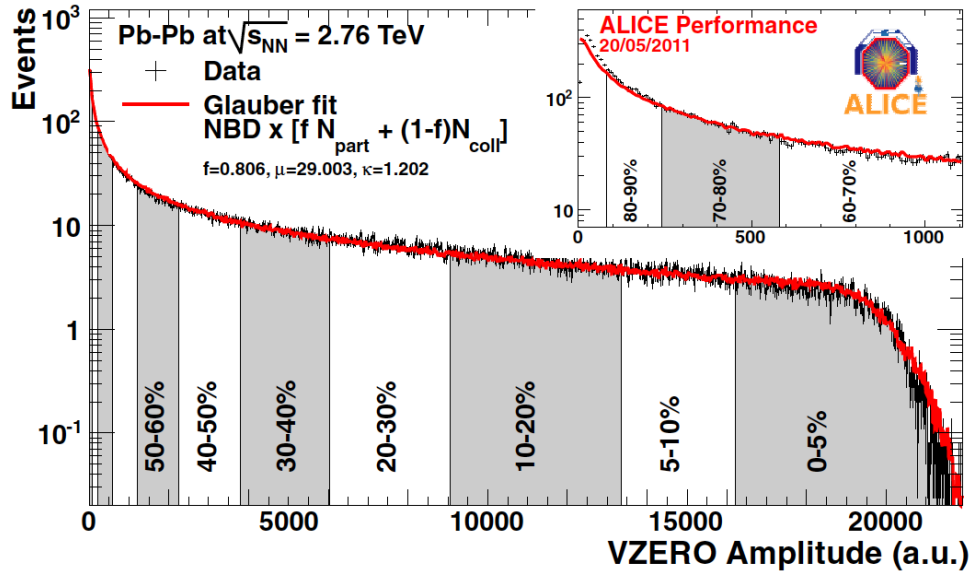


Figure 1.4: An illustration of the multiplicity distribution which is divided into centrality bins in ALICE measurements. The red line shows the fit of the Glauber calculation to the measurement. Figure from [79].

In practice this definition is provided by dividing events into percentile bins by the observed multiplicity of produced particles. In a heavy-ion collision the total multiplicity can be related to the number of participants. Small centrality percentages correspond to central events with the highest multiplicity while peripheral collisions have lower multiplicities and thus higher centrality percentages. Figure 1.4 shows an observed multiplicity distribution from ALICE measurements [79] with the centrality bin division. The distribution is fitted using a phenomenological approach based on a Glauber Monte Carlo calculation [80].

The Glauber Model is often used to model the nuclear geometry in a heavy-ion collision. The model was originally introduced already in 1958 [81] and the modern terminology and tools were introduced in 1976 by Białas, Bleszyński, and Czyż [82] to model inelastic nuclear collisions.

The model starts by defining the thickness function which is the integral of the nuclear density over a line going through the nucleus with minimum distance  $s$  from the centre of the nucleus

$$T_A(s) = \int_{-\infty}^{\infty} dz \rho(\sqrt{s^2 + z^2}), \quad (1.4)$$

where  $\rho(\sqrt{s^2 + z^2})$  is the number density of nuclear matter. This can be experimentally determined by studying the nuclear charge distribution in low-energy

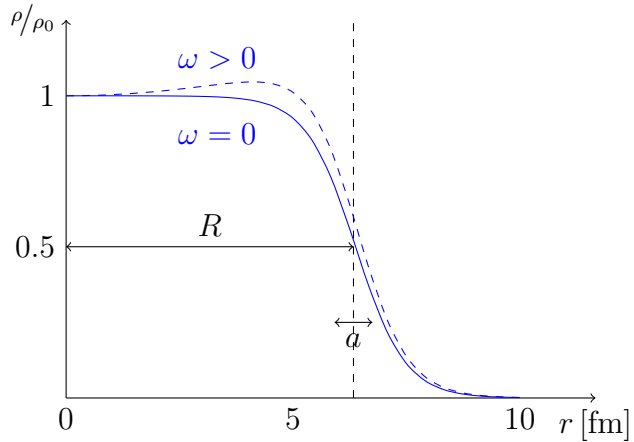


Figure 1.5: Woods-saxon distribution, with typical values for a Pb nucleus,  $a = 0.55\text{fm}$  and  $R = 6.6\text{fm}$ .

electron-nucleus scattering experiments [80, 83]. For a spherically symmetric nucleus a good approximation is given by the Woods-Saxon potential [84]

$$\rho(r) = \frac{\rho_0(1 + \omega r^2/R^2)}{1 + \exp(\frac{r-R}{a})}, \quad (1.5)$$

where  $\rho_0$  is the nucleon density in the centre of the nucleus,  $R$  is the nuclear radius,  $a$  parametrizes the depth of the skin and  $\omega$  can be used to introduce a surface excess. Figure 1.5 shows how this distribution looks like with parameters observed for lead nuclei. With  $\omega = 0$  the density changes only slightly as a function of  $r$  until it quickly drops to almost 0 around  $R$ . The slope and length of the transition region is given by  $a$ .

The integral over the overlap area of two thickness functions of colliding nuclei defines the overlap function

$$T_{AB}(\vec{b}) = \int d^2s T_A(\vec{s}) T_B(\vec{s} - \vec{b}). \quad (1.6)$$

In essence this is the material that takes part in the collision for a given impact parameter  $\vec{b}$ . The average overlap function,  $\langle T_{AA} \rangle$ , in an A-A collisions is given by [85]

$$\langle T_{AA} \rangle = \frac{\int T_{AA}(b) db}{\int (1 - e^{-\sigma_{pp}^{inel} T_{AA}(b)}) db}. \quad (1.7)$$

Using  $\langle T_{AA} \rangle$  one can calculate the mean number of binary collisions

$$\langle N_{coll} \rangle = \sigma_{pp}^{inel} \langle T_{AA} \rangle, \quad (1.8)$$

where the total inelastic cross-section,  $\sigma_{pp}^{inel}$ , gives the probability of two individual nucleons interacting. As every binary collision has an equal probability for direct production of high-momentum particles the number of high momentum tracks is proportional to  $\langle N_{coll} \rangle$  [84, 86, 87]. This requires knowledge of  $\sigma_{inel}^{NN}$ , which can be measured in proton-proton collisions with different energies. At the LHC the most precise cross section measurements come from TOTEM [88].

Contrary to hard particles, soft particle production is based on the number of participants [86]. It can be assumed that participating nucleons get excited and, since the time scales are too short for any reaction to happen in the nucleons, it does not matter how many interactions a single nucleon experiences. After the interactions excited nucleons produce a predictable number of soft particles. The average number of participants,  $\langle N_{part} \rangle$  can be calculated from the Glauber model as

$$\begin{aligned} \langle N_{part}^{AB}(\vec{b}) \rangle &= \int d^2 s T_A(\vec{s}) \left[ 1 - \left[ 1 - \sigma_{NN} \frac{T_B(\vec{s} - \vec{b})}{B} \right]^B \right] \\ &+ \int d^2 s T_B(\vec{s}) \left[ 1 - \left[ 1 - \sigma_{NN} \frac{T_A(\vec{s} - \vec{b})}{A} \right]^A \right]. \end{aligned} \quad (1.9)$$

In practice the Glauber model can be implemented in two common ways. Simple analytical expression can be obtained from the optical approximation. These include the nucleus-nucleus interaction cross-section, the number of interacting nucleons and the number of nucleon-nucleon collisions on average. In the optical Glauber it is assumed that the nucleons move independently during the crossing of the nuclei and they will be essentially undeflected.

With increased appreciation for the physics emerging from fluctuations in the collision geometry the Glauber Monte Carlo (GMC) approach has provided a way to get a better description of heavy-ion collisions. In GMC nucleons are distributed randomly according to the nuclear density distribution [84]. In the simplest model nucleons of two nuclei will interact if their distance in the orthogonal plane,  $d$  is small enough, i.e.

$$d < \sqrt{\sigma_{inel}^{NN}}. \quad (1.10)$$

The number of participants and binary collisions can be calculated per event. By simulating many heavy-ion collisions one can then determine both average values

and the fluctuation around the average. The results of one GMC Pb–Pb event with impact parameter  $b = 9.8$  fm is shown in Figure 1.6.

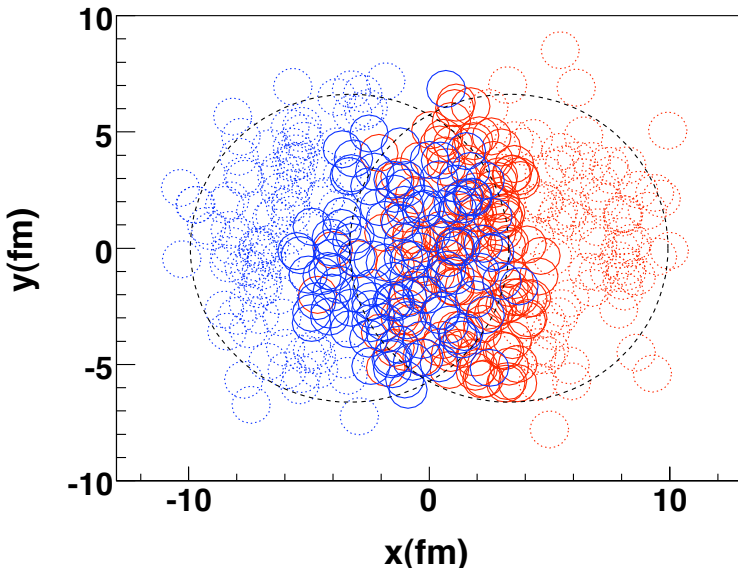


Figure 1.6: The figure shows a Pb–Pb collision in a Glauber Monte Carlo simulation. The big circles with black dotted boundaries outline the two colliding nuclei. Small blue and red circles represent nucleons with different colours for the two nuclei. Circles with solid boundaries are participants i.e. there is an overlap with at least one nucleon from the other nucleus. Circles with dotted boundaries are spectators which do not take part in the collision [89].

### 1.3.2 Collective motion

For most cases the evolution of a heavy-ion event can be separated into four stages. A schematic illustration of the evolution of a heavy-ion collision with this division is shown in Figure 1.7. Stage 1 is the pre-equilibrium stage, the phase immediately after the collision. It is commonly assumed to last about  $1 \text{ fm}/c$  in proper time  $\tau$ .

During the second stage the system has thermal equilibrium or at least a near-equilibrium. This lasts about  $5 - 10 \text{ fm}/c$  until the temperature of the system decreases enough for the system to lose its deconfined, strongly coupled state and hadronisation occurs. During stage 2 the matter is driven outwards by the large pressure gradient from the centre of the collision to the vacuum outside the collision volume.

During stage 3 the hadrons still interact with each other. This ends when

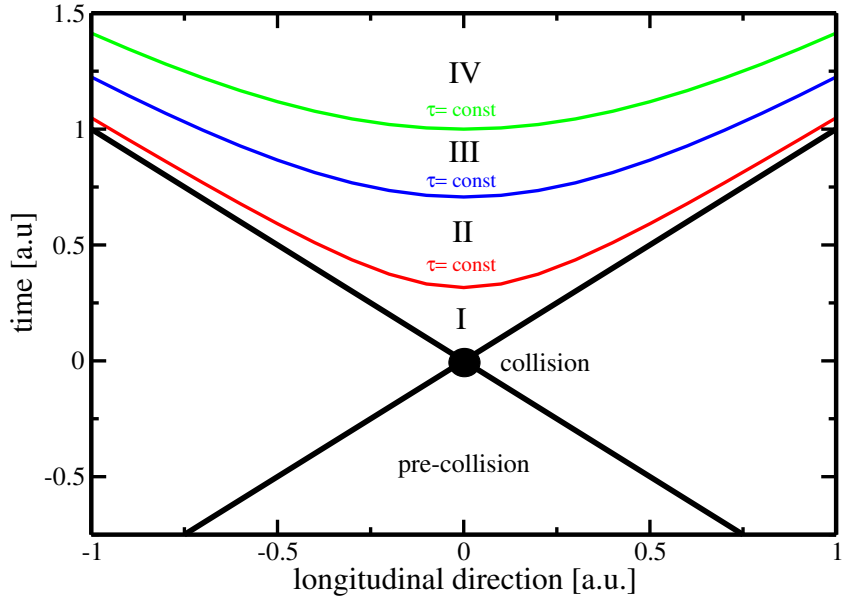


Figure 1.7: Schematic representation of a heavy-ion collision as a function of time and the longitudinal coordinate  $z$ . The various stages of the evolution are separated by hyperbolic curves which are defined by fixed proper time  $\tau = \sqrt{t^2 - z^2}$ . Figure from [90].

hadron scattering becomes rare and in the final phase hadrons become free streaming until they reach the detector.

In a heavy-ion collision the bulk collective particle production that is emitted from the QGP medium is referred to as flow. During hadronisation the pressure-driven expansion of QGP turns into the flow of mainly low-momentum particles. Since the expansion is close to isotropic the resulting particle flow is isotropic with small anisotropies of the order of 10% at most. The isotropic component of flow is referred to as radial flow. Figure 1.8 shows the transverse momentum spectra  $dN/dp_T$  in heavy-ion collisions.

The geometry of the heavy-ion collision produces an anisotropic component to the collective motion. Figure 1.9 gives illustrations of collisions with different impact parameters. In a non-central heavy-ion collision, with a large impact parameter, the impact zone has an elliptical shape in the transverse plane. In a central collision, with a small impact parameter, the overlap region is almost circular.

During the evolution of the QGP medium this asymmetry of the impact zone is transformed into the asymmetry of particle production in momentum space. The distance from high pressure, the collision centre to low pressure, vacuum outside the impact zone varies. It is smallest in the direction of the impact parameter  $\vec{b}$

and thus the pressure gradient is strongest in this direction, in-plane. The higher pressure gradient will produce more collective flow as compared to the out-of-plane direction [92–94]. Figure 1.9 illustrates the difference in impact zone and resulting flow.

Flow anisotropy is typically parametrised in the form of a Fourier composition

$$E \frac{d^3N}{dp^3} = \frac{1}{2\pi} \frac{d^2N}{dp_T d\eta} \left( 1 + \sum_{n=1}^{\infty} 2v_n(p_T, \eta) \cos(n(\phi - \Psi_n)) \right), \quad (1.11)$$

where the overall normalisation,  $\frac{1}{2\pi} \frac{d^2N}{dp_T d\eta}$ , gives the strength of radial flow,  $\Psi_n$  gives the rotation angle of the component  $n$  contribution, and the coefficients  $v_n$  give the relative contributions of anisotropic flow components. The coefficients

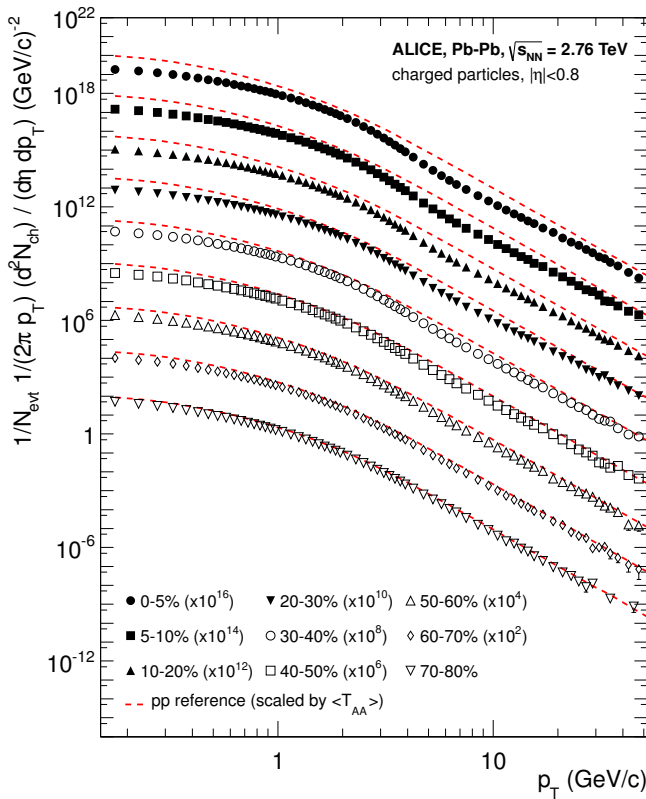


Figure 1.8: The radial flow is represented by the charged particle spectra for different centrality classes given in the legend. The dashed lines show proton-proton reference spectra which are scaled by the nuclear overlap function determined for each centrality class. For clarity the distributions and the reference spectra are offset by arbitrary factors. Figure from [91].

can depend on both transverse momentum  $p_T$  and pseudorapidity  $\eta$ . As in general Fourier analysis is known as harmonic analysis the components are often referred to as harmonic flow components. Elliptic flow, i.e. flow with two maxima, is represented by  $v_2$  and  $v_3$  represents triangular flow while the first coefficient,  $v_1$ , is connected to directed flow [95]. Because of momentum conservation directed flow is in total assumed to be zero. In certain rapidity or momentum regions it can be nonzero but it must be canceled by other regions.

In a peripheral collision  $v_2$  is the dominant part of anisotropic flow as it arises from the asymmetric geometry of the collision region. For a long time the odd harmonics were considered to be negligible, because they would require a more complex asymmetry. In 2007 Mishra *et al.* [96] argued that inhomogeneities in the initial state density would lead to non-zero  $v_n$  values for  $v_3$  and other higher harmonics. As the colliding nuclei are not static objects, the arrangement of the nucleons at the time of a collision is random [97]. Therefore the shape of the collision zone is not symmetric but rather more complex. On the other hand, inside the collision zone the created medium is not homogenous. Instead the medium includes hot spots with higher density. It is expected that higher harmonics of  $v_n$  would be suppressed more by viscous effects and thus the shape of  $v_n$  as a function

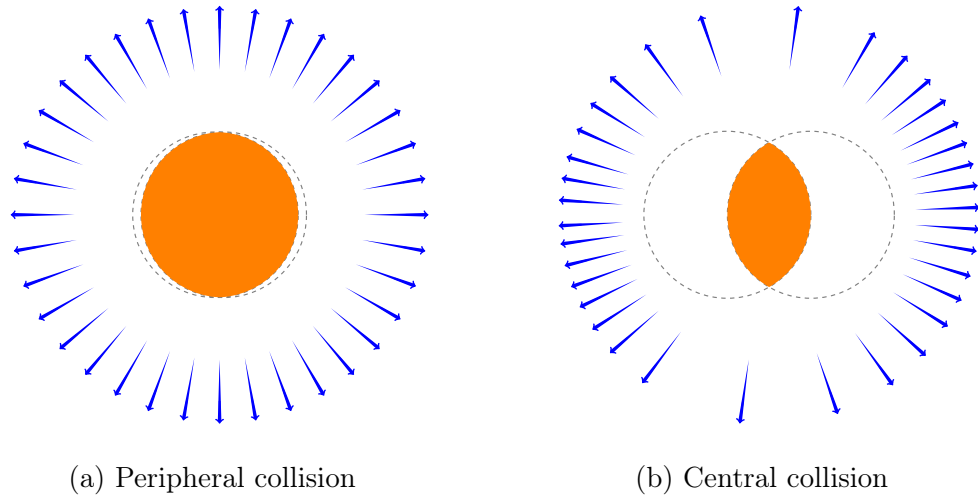


Figure 1.9: Illustration of elliptic flow in central and peripheral collisions. The density of the arrows represent the strength of flow in the corresponding azimuthal direction as seen in the detectors. In a peripheral collision momentum the difference in pressure gradients gives a strong flow into the in-plane direction while the flow into the out-of-plane direction is small. In a central collision flow is more isotropic and dominated by higher harmonics. In the figure the difference is exaggerated and the difference in total multiplicity is not taken into account.

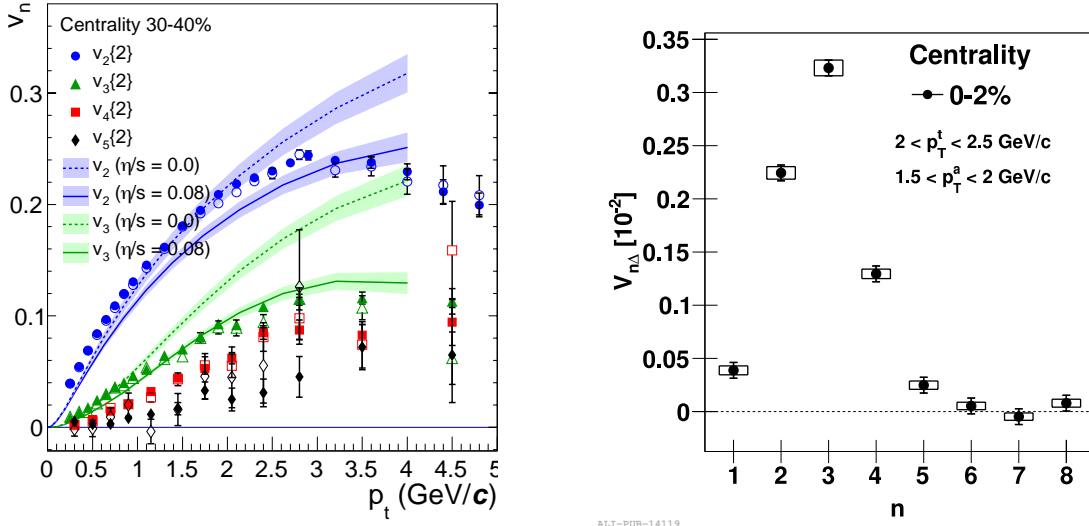


Figure 1.10: Flow measurements of higher harmonics. *left:* ALICE measurement of  $v_2, v_3, v_4, v_5$  as a function of transverse momentum. Two-particle correlations are used to obtain the harmonic coefficients. The full and open symbols are for different  $\Delta\eta$  separation between the particles ( $\Delta\eta > 0.2$  and  $\Delta\eta > 1.0$ ). The observations are compared to hydrodynamic calculations [100] with varying values of the shear viscosity to entropy ratio  $\eta/s$ . Figure from [101]. *right:* Amplitude of  $v_n$  coefficients as a function of  $n$  for the 2% most central collisions as measured by ALICE. Figure from [102].

of  $n$  could be used to study  $\eta/s$  [98].

The first one to predict anisotropic flow in heavy-ion collisions was Ollitrault in 1992 [92] and the first experimental studies were conducted in 1993 at the AGS [99]. Instead of the Fourier composition these initial studies used alternative approaches. In AGS the reaction plane angle in one rapidity region was observed to be correlated with the particle production in another rapidity region. The first ones to introduce the Fourier decomposition were Voloshin and Zhang in 1996 [95].

Figure 1.10 shows measurements of different harmonics coefficients. The left panel shows the flow coefficients in peripheral collisions as a function of track  $p_T$  as measured by ALICE [101]. As shown on the right hand panel of Figure 1.10 the  $v_n$  values decrease in central collisions as a function of  $n$  for  $n > 3$ . In peripheral collisions the elliptic flow component  $v_2$  will be larger.

In Figure 1.10 the results are compared to predictions from hydrodynamic calculations [100]. In general the measured collective flow in heavy-ion collisions has

been successfully modelled with the relativistic version of hydrodynamics. The power of this approach lies in its simplicity and generality. Hydrodynamic calculations only require that the system reaches at least local thermal equilibrium. For this the system must have a mean free path that is shorter than the length scales of interest, which is assumed to hold for the strongly coupled QGP phase of a heavy-ion collision [90].

The first approaches using the relativistic version of hydrodynamics were performed already in the 1950's [103], before QCD was discovered. The early studies used it to model proton-proton collisions. For the use of heavy-ion collisions hydrodynamics has been under development since the 1980's. One early example is the study of boost-invariant longitudinal expansion and infinite transverse flow by Bjorken [104]. Later studies added finite size and dynamically generated transverse size [105, 106].

Over the years understanding of the properties of the QGP has been improved with the help of new data from LHC and RHIC and theoretical developments. For example, as shown in Figure 1.11(a), the quantification of the temperature dependence of the shear viscosity over entropy ratio,  $\eta/s$  has been tested with an event-by-event model [107] that combines viscous hydrodynamic calculations with the Eskola-Kajantie-Ruuskanen-Tuominen (EKRT) model for initial conditions.

The initial density profiles for hydrodynamic simulations are calculated using a next-to-leading order perturbative-QCD (pQCD) and the EKRT model [108, 109]. The following space-time evolution is described by relativistic dissipative fluid dynamics. The simulation is performed using different parametrisations of the temperature dependence of the shear viscosity to entropy density ratio  $\eta/s(T)$ .

This model has been observed to give a good description of the charged hadron multiplicity and of the low- $p_T$  region of the charged hadron spectra both at RHIC and at LHC [107]. Each of the different  $\eta/s(T)$  parametrisations were adjusted to reproduce the measured  $v_n$  from central to mid-peripheral collisions. Previous measurements [110] have ruled out models where the temperature of the phase transition is larger than for "param1". The two sets of parameters which described most of the data are labeled as "best fits" in Figure 1.11(a). For the "param1" parametrisation the phase transition from the hadronic to the QGP phase occurs at the lowest temperature, around 150 MeV. This parametrisation is also characterised by a moderate slope in  $\eta/s(T)$  which decreases (increases) in the hadronic (QGP) phase.

The estimation of the  $\eta/s(T)$  dependence has been also studied with a Bayesian analysis, which is applied to form the initial conditions with no assumptions on the physical mechanisms of entropy production [111]. The robust statistical analytical methods allow calibrating the model to data in a multi-dimensional parameter space. In addition to finding the most likely combination of input parameters,

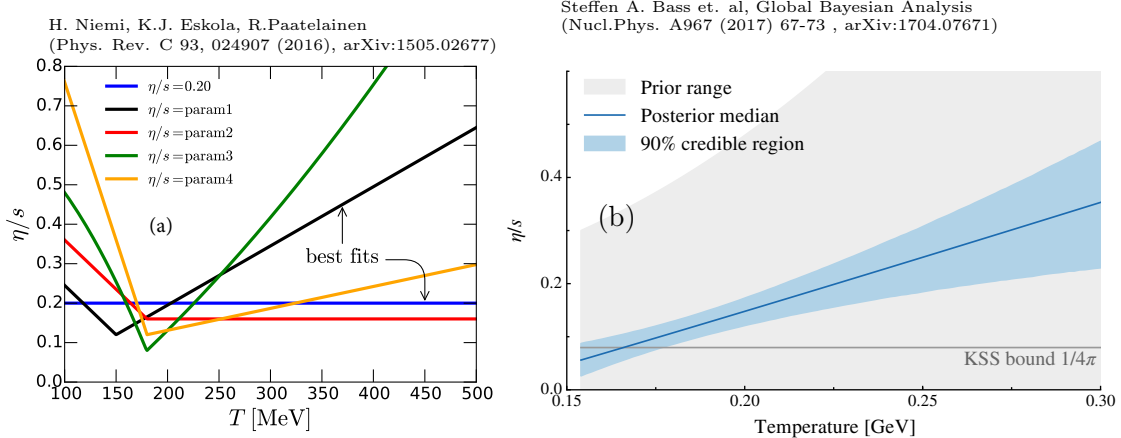


Figure 1.11: Temperature dependence of  $\eta/s$ . *left*: Different parametrisations of  $\eta/s(T)$  that have been tested in hydrodynamical simulations. *right*: Result of a global Bayesian analysis narrowing down the possible  $\eta/s(T)$  behaviour. These figures have been reprinted from [107] and [111] with kind permissions from the American Physical Society.

the Bayesian statistical method provides the full uncertainty quantification in the form of posterior probability distributions for all the parameters. The  $\eta/s(T)$  parametrisation resulting from this analysis is shown in Figure 1.11(b).

Based on these model calculations, the phase transition from the hadronic to the QGP phase occurs at the lowest temperature, around 150 MeV. Although the temperature dependence of the  $\eta/s$  is still not well established, the calculations generally suggest a minimum value of  $\eta/s$  from 0.08 to 0.12, close to the universal limit  $1/(4\pi)$  [65].

Recently, several advancements have been made in order to further constrain the temperature dependence of  $\eta/s$ . New observables, such as the symmetric cumulants [110, 112], have provided detailed information on the temperature dependence over the evolution of the QGP. Furthermore, the non-linear formalism has resulted in remarkable new constraints on the initial conditions [113], and the  $\eta/s$  at the freeze-out conditions, which is among the least understood parts of hydrodynamic calculations.

## 1.4 Hard processes

### 1.4.1 pQCD factorization

The term Hard Scattering is used for the scattering of two point-like constituents (partons) of colliding nucleons, when the momentum transfer  $Q^2$  is large ( $Q \gg \Lambda_{\text{QCD}}$ ). Figure 1.12 shows the incoming partons, quarks or gluons, as they exchange a space-like virtual gluon and produce two highly virtual outgoing partons. The outgoing partons will eventually fragment into collimated showers of partons, referred to as jets.

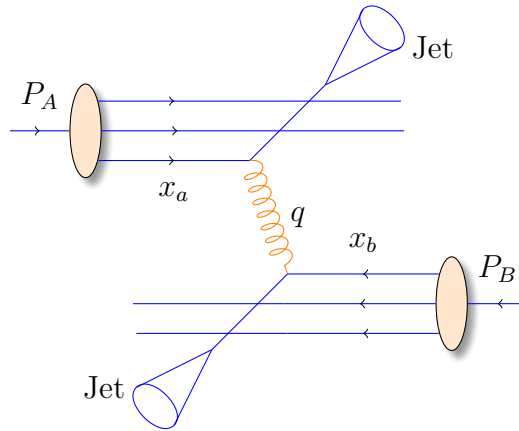


Figure 1.12: Schematic view of hard scattering process between two protons, producing two jets

Historically one would study hard scatterings foremost with inclusive hadron spectra. In this context hadron production from hard scatterings can be factorised into three components; the parton distribution functions  $f_a$ ,  $f_b$  that give the probability of getting a parton with momentum fraction  $x$  of the proton, the cross section of the elementary scattering  $ab \rightarrow cd$ , and the fragmentation functions,  $D_{h/c}^0$ , that give the probability of getting hadron  $h$  from the parton.

$$\frac{d\sigma_{pp}^h}{dy d^2 p_T} = K \sum_{abcd} \int dx_a dx_b f_a(x_a, Q^2) f_b(x_b, Q^2) \frac{d\sigma}{dt}(ab \rightarrow cd) \frac{D_{h/c}^0}{\pi z_c}, \quad (1.12)$$

where  $K$  is normalisation constant and

$$x_{a,b} = \frac{|p_{a,b}|}{|p_{\text{proton}}|}. \quad (1.13)$$

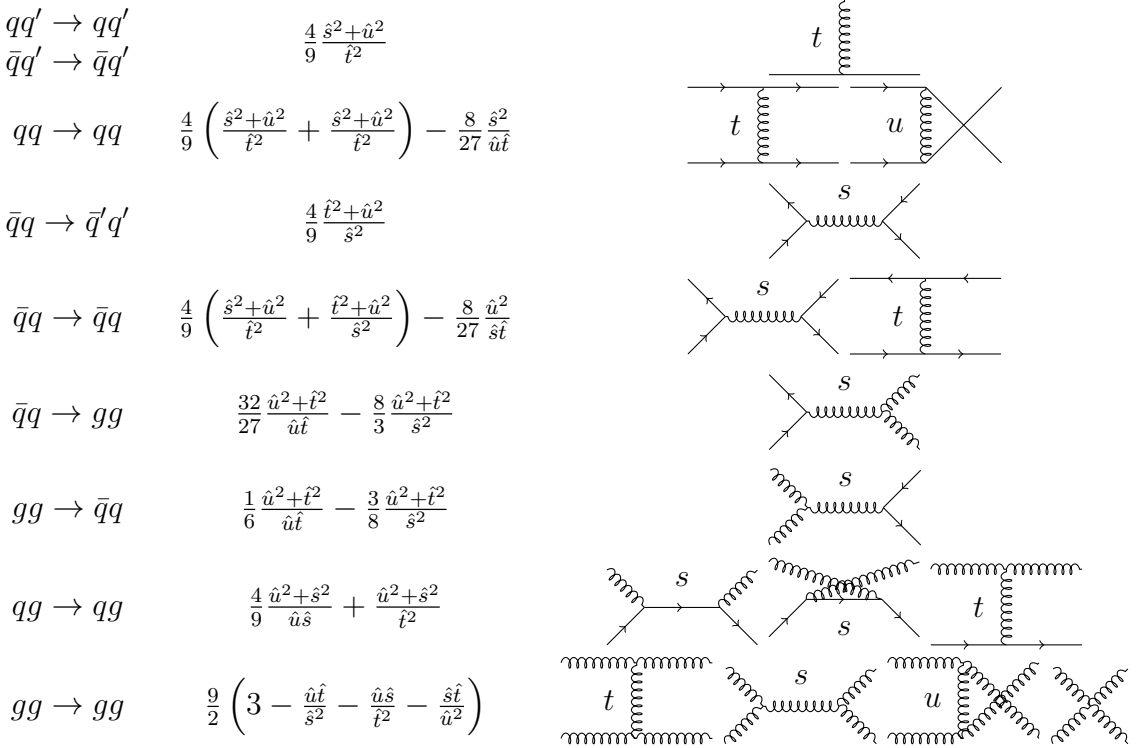


Figure 1.13: The basic pQCD processes and their quadratic matrix elements

Parton distribution functions will be discussed further in the following section. The elementary cross section  $ab \rightarrow cd$  can be calculated from QCD. A summary of the first order  $2 \rightarrow 2$  processes in QCD is shown in Figure 1.13.

The final component in the factorization, fragmentation functions, describe the distribution of the fractional momenta of fragments radiated from the outgoing parton. In a leading order picture, it can be interpreted as the probability that the observed final state originates from a given parton [114]. Like the PDFs they are non-perturbative and must be determined experimentally. Most measurements come from  $e^+e^-$  collisions where the kinematics are better controlled.

## Parton Distribution Function

Parton Distribution Functions (PDFs)  $f_a(x)$  give the differential probability for parton  $a$  to carry momentum fraction  $x$  of the proton momentum. As the PDFs cannot be calculated from first principles they are measured in Deeply Inelastic Scattering (DIS) experiments [115] and are extrapolated to the relevant momentum scales using the Dokshitzer-Gribov-Lipatov-Altarelli-Parisi (DGLAP) evolution scheme [116–118]:

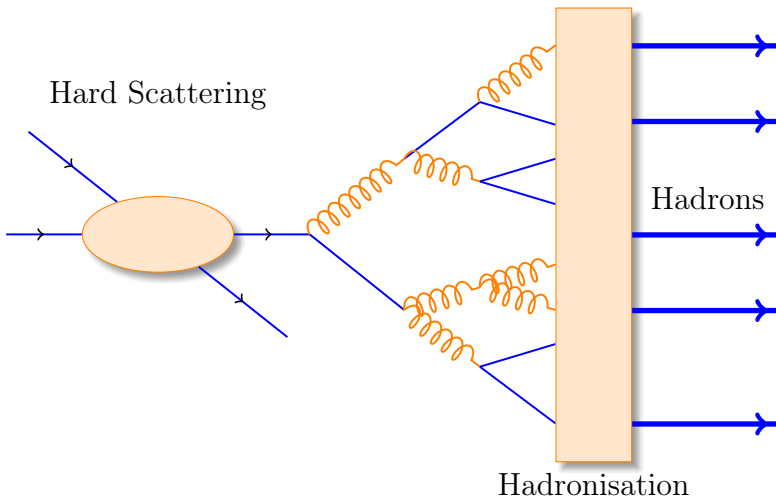


Figure 1.14: An illustration of jet showering. The highly virtual parton from the hard scattering will produce a shower of softer partons. When the virtuality is low enough the shower will go through a hadronisation process that produces the hadrons, which will be eventually observed in the detector.

$$\mu_F^2 \frac{\partial f_i(x, \mu_F^2)}{\partial \mu_F^2} = \sum_j \frac{\alpha_s(\mu_F)}{2\pi} \int_x^1 \frac{dz}{z} P_{ij}(z) f_j\left(\frac{x}{z}, \mu_F^2\right), \quad (1.14)$$

where  $\alpha_s$  is the coupling constant of the strong interaction and  $\mu_F$  is a factorization scale. The splitting functions  $P_{ij}$  describe the probability to radiate parton  $i$  with momentum fraction  $x$  from parton  $j$ . Different theory interpretation and experimental data gives rise to different PDF's. Thus there are several commonly used PDF sets: CTEQ [119], HERAPDF [120], PDF4LHC [121], etc.

### 1.4.2 Jet showering

More detailed studies of the hard processes require a formulation of the showering process. The full picture is a complicated  $2 \rightarrow n$  scattering, but it is typically seen as a series of  $1 \rightarrow 2$  splittings with decreasing virtuality following the initial  $2 \rightarrow 2$  hard scattering [122].

To first order the cascade is governed by the DGLAP evolution equation [116–118]

$$dP_a(z, Q^2) = \frac{dQ^2}{Q^2} \frac{\alpha_s}{2\pi} P_{a \rightarrow bc}(z) dz, \quad (1.15)$$

which gives the differential probability that parton  $a$  (mother) will branch to two partons  $b$  and  $c$  (daughters), at a virtuality scale  $Q^2$ . Daughter  $b$  takes a fraction

$z$  of the parton  $a$  energy and daughter  $c$  takes energy fraction  $1 - z$ . The splittings kernels  $P_{a \rightarrow bc}(z)$  are

$$P_{q \rightarrow qg}(z) = \frac{4}{3} \frac{1+z^2}{1-z} \quad (1.16)$$

$$P_{g \rightarrow gg}(z) = 3 \frac{(1-z)(1-z)^2}{z(1-z)} \quad (1.17)$$

$$P_{g \rightarrow q\bar{q}}(z) = \frac{n_f}{2} (z^2 + (1-z)^2), \quad (1.18)$$

where  $n_f$  is the kinematically allowed number of quark flavours. There is some freedom in how the evolution variable  $Q^2$  is chosen. As long as  $Q^2 = f(z)m^2$  and  $f(z)$  is a positive and a smooth function it holds that

$$\frac{dQ^2}{Q^2} dz = \frac{dm^2}{m^2} dz, \quad (1.19)$$

where  $m$  is the on-shell mass of a particle. Of the Monte Carlo generators used in this thesis PYTHIA uses  $m^2$  as the evolution variable [123], while HERWIG uses an energy-weighted emission angle  $E^2(1 - \cos \theta) \approx m^2/(z(1-z))$  [124].

Formally Equation 1.15 corresponds to the emission of an infinite number of partons. However very soft and collinear gluons need not be considered and one can introduce an effective cut-off scale  $Q_0$ , usually taken to be of the order of 1 GeV.

Going further one approach is to introduce time ordering, i.e. to decide which of the emissions occurs first. This is done in the form of a Sudakov form factor [125]

$$P_a^{no}(Q_{\max}^2, Q^2) = \exp \left( - \int_{Q^2}^{Q_{\max}^2} \int_{z_{\min}}^{z_{\max}} dP_a(z', Q'^2) \right), \quad (1.20)$$

which gives the probability that no emissions occur between the initial maximum scale  $Q_{\max}^2$  and a given  $Q^2$  and within limits  $z_{\min} < z < z_{\max}$ . Thus the probability for the first branching to occur at  $Q^2 = Q_a^2$  is given by

$$d\Delta_a(z, Q_a^2, Q_{\max}^2) = dP_a(z, Q_a^2) P_a^{no}(Q_{\max}^2, Q_a^2). \quad (1.21)$$

Partons  $b$  and  $c$  that were produced will further branch with maximum virtuality scale  $Q_{\max}^2$  given by  $Q_a^2$ . Similarly their daughters will continue branching until the cutoff scale is reached, thus producing a shower.

### 1.4.3 Soft gluon radiation and angular ordering

When a gluon splits into two quarks one of the produced quarks can emit a soft gluon as seen in Figure 1.15. In the laboratory frame the time it takes for a gluon to be emitted from a quark can be estimated to be [126]

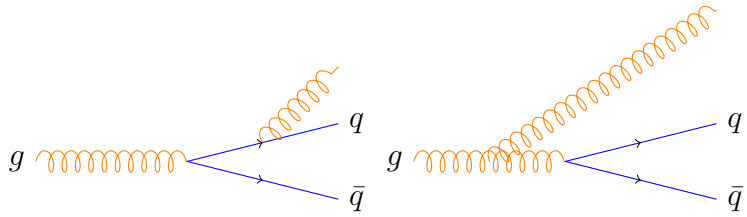


Figure 1.15: Soft gluon production

$$t_{\text{emit}} \approx \frac{1}{E_q}, \quad (1.22)$$

where the energy of the quark is given by  $E_q$ . In the rest frame of the quark its energy is set by its virtuality  $M_{\text{virt}}$ . With the assumption that the quark is massless the Lorentz factor from the rest frame to the laboratory frame is

$$\gamma = \frac{E_q}{M_{\text{virt}}}. \quad (1.23)$$

Thus the emission time can be written as

$$t_{\text{emit}} \approx \frac{E_q}{M_{\text{virt}}^2} = \frac{E_q}{(k + p)^2}, \quad (1.24)$$

where  $k$  and  $p$  are the quark and gluon four-momenta after the gluon emission. As the square of a four-momentum is Lorentz invariant, this can be expanded in the laboratory frame. Taking the end products as massless, this can be given in a form where the gluon emission time is expressed by the opening angle  $\theta_{kq}$  between the quark and the gluon

$$t_{\text{emit}} \approx \frac{1}{k\theta_{kq}^2}. \quad (1.25)$$

The transverse wavelength of the emitted gluon is  $\lambda_{\perp}^{-1} = k_{\perp} \approx k\theta_{kq}$ . This gives

$$t_{\text{emit}} \approx \frac{\lambda_{\perp}}{\theta_{kq}}. \quad (1.26)$$

The secondary gluon can only probe the quark of the earlier splitting if the transverse wavelength is smaller than the transverse separation of the produced  $q\bar{q}$  pair, which is given by

$$r_{\perp}^{q\bar{q}} \approx \theta_{q\bar{q}} t_{\text{emit}} \approx \lambda_{\perp} \frac{\theta_{q\bar{q}}}{\theta_{kq}}. \quad (1.27)$$

Thus in order for the emission to probe the individual quark, the opening angle of the  $q\bar{q}$  splitting,  $\theta_{q\bar{q}}$ , must be larger than  $\theta_{kq}$ . If the opening angle  $\theta_{kq}$  is larger, the gluon can't distinguish between the quark and the antiquark, and it can only probe the state of the system before the splitting. Thus it is indistinguishable from a gluon emitted by the primary gluon.

This leads to the angular ordering of soft gluon radiation. Every radiated gluon must be at a smaller angle than the previous one. The angular ordering effect can be calculated in all orders [126] and in the DGLAP formalism one can select the evolution variable  $Q^2$  in a way that ensures angular ordering as is done in the Herwig MC generator [124]. In PYTHIA 8 this is strictly not included, but the transverse momentum ordered showers can describe the soft gluon emissions with similar accuracy as the angular ordered showers [125].

#### 1.4.4 Jet hadronisation

When the virtuality of the shower is low enough, the shower starts to hadronise. In this regime the parton shower reaches an energy scale close to  $\Lambda_{\text{QCD}}$  and the perturbative description is no longer valid. Thus the hadronisation stage must be described in a non-perturbative manner. In general hadronisation is assumed to be universal, i.e. it should be independent of the collision energy and the collision system.

The simplest model that is used in several theory approaches is the local parton-hadron duality hypothesis [127]. In this hypothesis it is assumed that there exists a low virtuality scale  $Q_0$  in which the hadronisation happens, that does not depend on the scale of the primary hard process. At this scale the partons transform into hadrons and their quantum numbers and flow of momentum directly gives those of the hadrons, with only small normalising corrections.

The next sections will present more complicated hadronisation models used in Monte Carlo generators, PYTHIA and Herwig.

#### Lund string model

One common implementation in MC generators is the Lund string fragmentation algorithm [128]. This is also used in the PYTHIA generator. The string model utilises the colour confinement property of QCD. The strong force between particles is expected to stay constant over large distances [125]. This can be modelled by imagining a colour flux tube being extended between outgoing partons as illustrated in Figure 1.16(a) for a  $q\bar{q}$ -pair. In the model the tube has a uniform transverse diameter of about 1 fm along its length. This leads to a linearly rising potential  $V(r) = \kappa r$  with the string constant  $\kappa$  describing the amount of energy

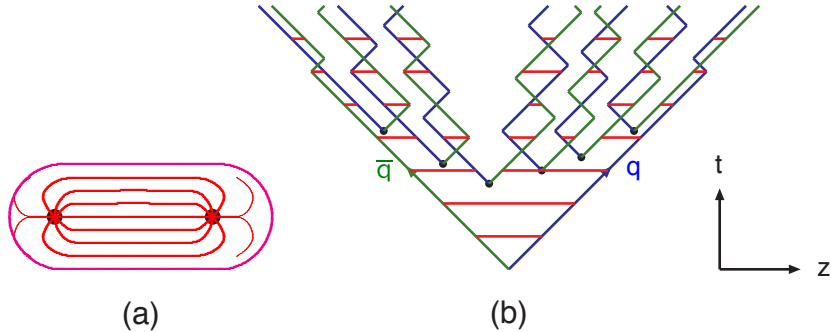


Figure 1.16: (a) A flux tube spanned between a quark and an antiquark. (b) The motion and breakup of a string system, with the two transverse degrees of freedom suppressed (diagonal lines are (anti)quarks, horizontal ones snapshots of the string field). This figure has been reprinted from [125] with kind permission from Elsevier.

per unit length. A value of  $\kappa \approx 1 \text{ GeV/fm} \approx 0.2 \text{ GeV}^2$  can be obtained from hadron mass spectroscopy [125].

The evolution of string fragmentation is illustrated schematically in Figure 1.16(b). The evolution is shown in the light cone presentation, i.e. the initial quark and antiquark are moving in opposite directions at the speed of light. The horizontal red line illustrates the string between the quark-antiquark pair. The string begins to stretch which continues until the potential energy stored in the string is large enough and it breaks, which forms a new quark-antiquark pair. If the original pair was  $q\bar{q}$  and the produced pair is  $q'\bar{q}'$ , these form new pairs,  $q\bar{q}'$  and  $q'\bar{q}$ .

Since these produced pairs are also moving away from each other, the strings between them will also stretch and can eventually break, creating even more pairs. This evolution proceeds until the invariant mass of the system becomes small enough and a group of final state mesons is formed.

To mathematically model the string the Lund model uses a massless relativistic string that has no transverse degrees of freedom. When a string breaks the pair is created at one point and the pair then tunnels out to a classically allowed region. Therefore the probability to create a new quark-antiquark pair is proportional to the tunnelling probability [128]

$$P_{\text{tunnelling}} \propto \exp\left(\frac{-\pi m_{\text{T}}^2}{\kappa}\right) = \exp\left(\frac{-\pi m^2}{\kappa}\right) \left(\frac{-\pi p_{\text{T}}^2}{\kappa}\right), \quad (1.28)$$

where the transverse mass  $m_{\text{T}}$  is defined as  $m_{\text{T}}^2 = m^2 + p_{\text{T}}^2$ . Here transverse refers to the plane transverse to the string axis. This equation gives a flavour-independent

Gaussian  $p_T$ -distribution for the created  $q\bar{q}$  pairs.

In this formalism the string fragmentation would only produce mesons, but we know that also baryons are created in the process. To produce baryons the model introduces a probability for the creation of a diquark-antidiquark pair instead of a quark-antiquark pair when a string breaks.

An iterative procedure is used to determine the kinematics of string breakages. The string fragmentation can be considered in any order, as there is no natural ordering. One can begin from the quark leg and proceed towards the  $\bar{q}$  leg, or vice versa. In this way the string fragmentation has left-right symmetry. To break the string into a hadron and the remaining system, the Lund model defines a symmetric fragmentation function as

$$f(z) \propto \frac{1}{z} (1-z)^a \exp\left(-\frac{bm_T^2}{z}\right), \quad (1.29)$$

where  $z$  is the fraction of light-cone momentum  $p^+$  that the hadron obtains in the string breakage,  $m_T$  is the transverse mass of the hadron and  $a$  and  $b$  are tuneable model parameters. For heavy quarks this is modified as

$$f(z) \propto \frac{1}{z^{1+bm_Q^2}} (1-z)^a \exp\left(-\frac{bm_\perp^2}{z}\right). \quad (1.30)$$

Thus the process starts from the quark leg of a  $q\bar{q}$  system and then considers the breaking into a new  $q'\bar{q}'$  pair closest to the  $q$ -leg. After this breakage there is a meson  $q\bar{q}'$  and a remainder system spanning from  $q'\bar{q}$ . This process continues until the antiquark leg is reached. Small corrections are required for the final two hadrons coming from a string as Equation (1.29) assumes that the mass of the remainder system is large.

One additional possibility one must consider is that a string can have such a low mass that it cannot break at all. For these cases the string is transformed into a single hadron and if necessary energy and momentum are exchanged with other partons in the event.

Some of the produced hadrons are short-lived ones which can still decay. The final set of particles is obtained when these have decayed [123].

## Cluster model

Instead of a string model HERWIG [124] uses a cluster model for hadronisation. The advantage of cluster models is that they require a smaller number of parameters than string models. The model is based on the preconfinement property of parton showers, i.e. the colour structure of a shower at any evolution scale  $Q_0$  is such that colour singlet combinations of partons can be formed with an asymptotically universal invariant mass distribution. The invariant mass is independent

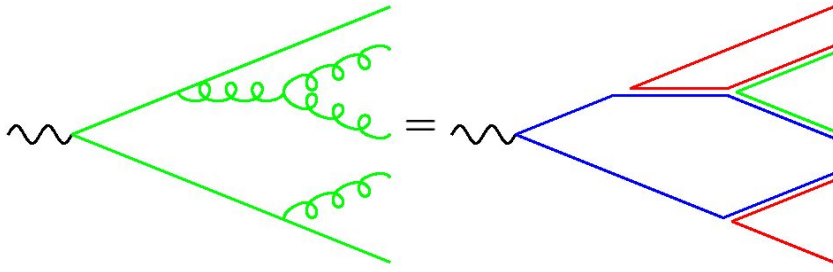


Figure 1.17: Colour structure of a parton shower to leading order in  $N_c$ . This figure has been reprinted from [125] with kind permission from Elsevier.

of the initial hard process scale  $Q$ , and depends only on  $Q_0$  and the QCD scale  $\Lambda_{\text{QCD}}$ , when  $Q \gg Q_0$  [125].

The cluster model starts by transforming all gluons non-perturbatively into  $q\bar{q}$  pairs, which requires that the gluons get a mass at least twice the lightest quark mass. When the gluons have been transformed into quarks, adjacent colour lines can be clustered into colour singlets that have mesonic quantum numbers. The sum of the momenta of partons defines the momentum of the entire cluster. The principle of colour-preconfinement states that the mass distribution of these clusters is independent of the hard scattering process and its centre-of-mass energy [124].

The mass of some of these initial clusters can be too large to reasonably describe an excited hadron and they must be split before they are allowed to decay. The condition to split cluster  $C$  is [124]

$$M_C^p \geq M_{\max}^p + (m_1 + m_2)^p, \quad (1.31)$$

where  $m_{1,2}$  are the masses of the constituents partons of the cluster.  $M_{\max}$  and  $p$  are parameters defined in the model. These have to be chosen separately for light, charmed and bottom quarks. When a cluster splits, a quark-antiquark pair is generated from the vacuum, which combined with the original quark-antiquark pair form two new clusters. This process continues until no clusters with masses fulfilling Equation 1.31 remain.

When all clusters have become light enough, the clusters into final state hadrons. If the mass of a cluster is high enough for decaying into a baryon-antibaryon pair, it can undergo either a mesonic or a baryonic decay. The probabilities of mesonic and baryonic decays are parameters in the model [124]. For a mesonic decay a quark-antiquark pair is generated from the vacuum and for baryonic decays a diquark-antidiquark pair is created. The exact products of the decay get chosen by the model and each cluster decays such that the decay is isotropic in the cluster rest frame. Any partons produced in the perturbative phase involved in the decay retain their original direction in the cluster rest frame. In cases where the cluster

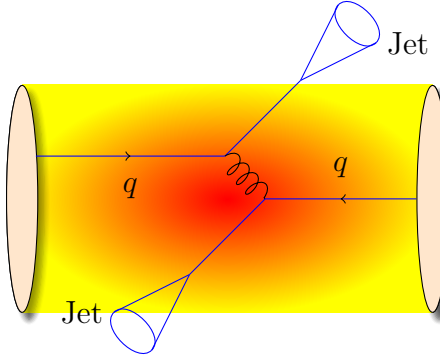


Figure 1.18: If hard scatterings happen in conjunction with QGP medium the produced jets must traverse the medium. Thus they are subject to interactions with the medium. Note that the dijet pair can be created anywhere within the medium volume and thus the two jets will have differing path lengths through the medium.

mass is too small for the cluster to decay into a pair of mesons, some energy and momentum is exchanged with nearby clusters so that it can decay into the lightest possible hadron. At the end the process gives a set of final state hadrons, some of which may be short-lived and decay before the end of the simulation [124].

#### 1.4.5 Interactions between jet and medium

Let us now look at what happens to jet production in heavy-ion collisions. Figure 1.18 shows a dijet produced inside QGP medium. High momentum particles are very rare and they are only produced in the initial collisions. In a heavy-ion collision, where a QGP medium is formed, the partons from a hard scattering are expected to interact strongly with the medium due to their colour charges and thus lose energy, either through gluon bremsstrahlung, or through collisions with medium partons [6]. This is referred to as jet quenching. Studying the modification of jets inside the medium gives another key approach to constraining the properties of QGP. Modification can be also observed in jet shapes, particle composition, fragmentation, splitting functions and many others.

#### Discovery of jet quenching via leading hadron suppression

First evidence of jet quenching comes from observing high  $p_T$  tracks, i.e. the leading hadrons of jets. In this picture jet energy loss in heavy-ion collisions is usually quantified with the nuclear modification factor  $R_{AA}$ , which is defined as

$$R_{AA}(p_T) = \frac{(1/N_{AA}^{evt}) dN^{AA}/dp_T}{\langle N_{coll} \rangle (1/N_{pp}^{evt}) dN^{pp}/dp_T} \quad (1.32)$$

where  $dN^{AA}/dp_T$  and  $dN^{pp}/dp_T$  are the observed spectra in heavy-ion and proton-proton collisions, respectively and  $\langle N_{coll} \rangle$  is the average number of binary nucleon-nucleon collisions in one heavy-ion event, which can be calculated from the Glauber model as shown in Section 1.3.1. When studying direct production of high  $p_T$  tracks a heavy-ion collision can be estimated relatively well to be only a combination of individual proton-proton collisions. At low  $p_T$  this scaling breaks down as the determining factor in direct production is the number of participants.

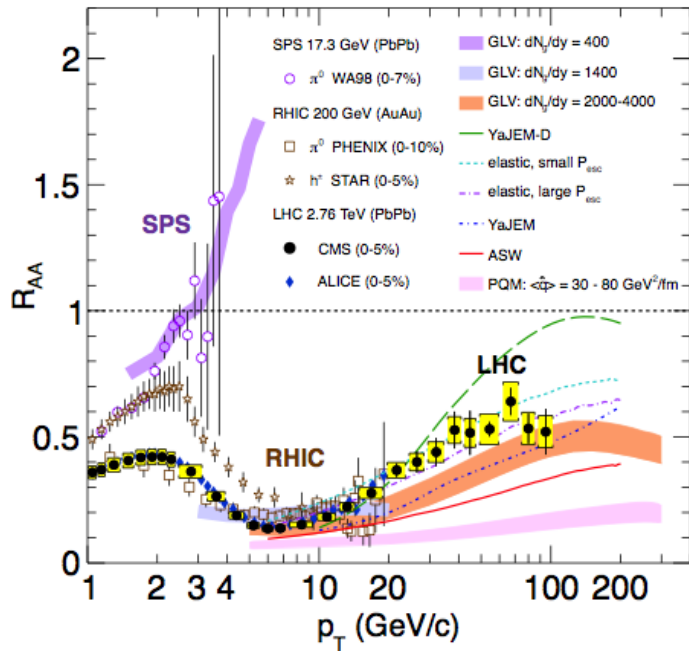


Figure 1.19: Measurements of the nuclear modification factor  $R_{AA}$  as a function of  $p_T$  in central heavy-ion collisions at three different centre-of-mass energies. Separate results are shown for different particle species [129–134] and the results are compared to predictions from several theoretical calculations [69, 135–139]. Figure from [134].

If the medium has no effect on high  $p_T$  particles the nuclear modification factor should be 1. As seen in Figure 1.19  $R_{AA}$  at RHIC and LHC has been observed to be as low as 0.2, which is a clear signal that jet quenching is happening. However, the physical interpretation is not that 80 % of high momentum tracks disappear, rather they are shifted to smaller momenta. The relation between the shift in momentum and  $R_{AA}$  depends thus on the steepness of the  $dN/dp_T$  spectrum. At

LHC energies the spectrum is flatter and thus the same  $R_{AA}$  value as in RHIC requires a larger momentum shift, which results from the larger temperature of the medium at LHC.

The reaction plane dependence of inclusive particle  $R_{AA}$  demonstrates that energy loss is path length dependent [140], as expected from models. The path length can be affected by collisions centrality and system size. However, the temperature and lifetime of the QGP also changes with changing centrality and system size. Thus to study different path lengths the angle relative to the reaction plane gives the cleanest signal, as the properties of medium remain the same. Additionally the study concluded that there is no suppression for path lengths below  $L = 2 \text{ fm}$ . Similar indications about path length dependence are given by jet  $v_2$  both at RHIC [141] and at LHC [142, 143].

### **QED Bremsstrahlung**

In modelling energy loss in QCD medium it is often useful to consider the analogy to the QED process, where an electron propagating through matter loses energy through photon Bremsstrahlung radiation. In the simplest case, each individual scattering centre results in a single emission of a photon. This is known as the Bethe-Heitler regime [144]. In this regime the energy spectrum of radiated photons  $dN/dE$  is proportional to  $1/E$ . However this radiation requires that the distance between scattering centres is larger than the formation length of the photon. When the scattering centres are closer than the formation length, the radiation process becomes suppressed. This phenomenon is known as the Landau-Pomeranchuk-Migdal (LPM) [145, 146] suppression. In this energy regime the radiated spectrum is proportional to  $1/\sqrt{E}$ .

Further suppression to low energy photons comes from the destructive interference leading to the suppression of Bremsstrahlung photons of  $E < \gamma\omega_p$ , where  $\omega_p$  is the plasma frequency of the radiator. This is known as Dielectric suppression. The photon energy distribution in this regime is proportional to the energy of the photon. A schematic view of the effect of these three regimes is shown in Figure 1.20.

### **Energy loss in QCD**

In QCD the radiative energy loss mechanism is given in terms of the transport coefficient  $\langle \hat{q} \rangle$ , which describes the average momentum transfer between the medium and parton [147]. The exact definition of this depends on the theoretical formalism used to describe the energy loss mechanism.

Similar to QED the simplest energy loss process is elastic QCD scattering off medium partons. In elastic scatterings a part of the energy of the scattered partons

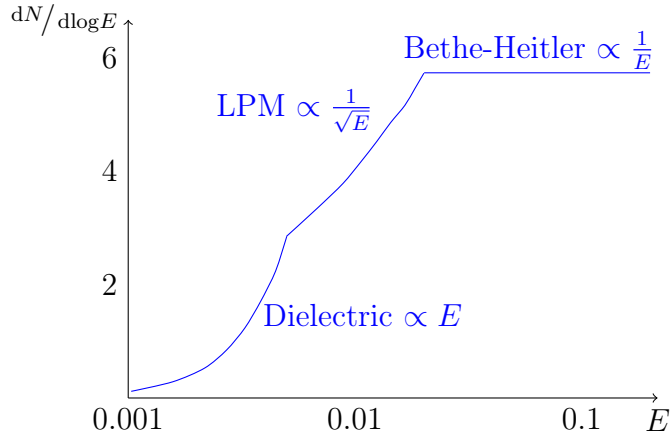


Figure 1.20: The expected bremsstrahlung spectrum for an electron propagating through material.

is absorbed by the thermal QGP medium and the energy of the initial parton is reduced. The mean energy loss caused by elastic scatterings can be estimated by

$$\langle \Delta E \rangle_{\text{el}} = \sigma \rho L \langle E \rangle_{\text{1scatt}} \propto L, \quad (1.33)$$

where  $\sigma$  is the interaction cross section,  $L$  is the path length through the medium, and  $\langle E \rangle_{\text{1scatt}}$  is the mean energy transfer of one individual scattering [148]. This requires that the energy transfer does not depend on the total energy of the parton ( $E$ ). The mean energy loss per path length is defined to be the transport coefficient

$$\langle \hat{q}_{\text{el}} \rangle = \frac{\langle \Delta E \rangle}{L}. \quad (1.34)$$

An alternative energy loss mechanism is medium-induced radiation. In QCD this radiation is mainly due to the elementary splitting processes,  $q \rightarrow qg_r$  and  $g \rightarrow gg_r$ . In the limit where the parton is moving with the speed of light, radiative energy loss is given by

$$\langle \Delta E \rangle_{\text{rad}} \propto T^3 L^2, \quad (1.35)$$

where  $L$  is again the path length through the medium and  $T$  is the medium temperature [149]. The different exponents of  $L$  in equations 1.33 and 1.35 indicate that radiative energy loss is dominant over elastic energy loss in a typical heavy-ion collision.

Several models have been used to attempt describing the mechanism of energy loss. The most used formalisms can be divided into four approaches.

In the Gyulassy-Levai-Vitev (GLV) [150] opacity expansion model the radiative energy loss is considered at a few scattering centres. Radiated gluons are constructed by pQCD calculations which sum up the relevant scattering amplitudes in terms of the number of scatterings. Another model using this opacity expansion approach is the ASW model by Armesto, Salgado and Wiedermann [151].

The second approach is the thermal effective theory formulation by Arnold, Moore and Yaffe (AMY) [152] uses dynamical scattering centres. The model uses leading order pQCD hard thermal loop effective field theory. In this model it is assumed that because of the high temperature of the QGP medium the coupling constant of the strong interaction can be treated as small. Partons, that propagate through the plasma, lose energy from both soft and hard scatterings.

These pQCD models consider the energy loss for a parton propagating through the medium. An alternative approach is the higher twist (HT) model by Wang and Guo [153] which considers the effect of energy loss on the energy scale evolution of fragmentation functions.

The fourth category includes the Monte Carlo methods. The PYTHIA event generator [154] is widely used in high-energy particle physics. Although primarily used for proton-proton collisions, PYTHIA was recently extended by the Angantyr [155] model which implements some features of heavy-ion collisions. Other Monte Carlo models based on PYTHIA describing the energy loss mechanism are PYQUEN [156] and Q-Pythia [157]. Other Monte Carlo models include JEWEL [158] and YaJEM [159].

#### 1.4.6 New paradigm of jet Quenching

As described in the previous sections the first indications of jet quenching, such as  $R_{AA}$ , looked essentially at the leading hadrons of jets, the hard part, ignoring the soft scale part of jet phenomena. However, experimental methods have since improved; jet reconstruction algorithms have become reliable in the LHC era. Instead of the leading hadron we can study the entire jet shower and its structure. In jet observables one must consider what happens to the lost energy. Radiated gluons may end up being clustered with the jet, depending on the radiation angle, the parameters of jet reconstruction and whether the gluon reaches equilibrium with the medium or not. Thus the suppression on the jet level is expected to be smaller. Figure 1.21 shows jet  $R_{AA}$  in central Pb–Pb collisions measured by ALICE, ATLAS and CMS and indeed jet  $R_{AA}$  is about 0.5 instead of 0.2.

Thus, on the level of the reconstructed jet, energy loss manifests itself as broadening and softening of the jet. This is seen for example in jet-hadron correlations. Figure 1.22 shows  $\Delta\eta$  correlations with the leading jet.  $\Delta\phi$  correlations have similar trends. Jets in heavy-ion collisions have been observed to be broader, than in proton-proton collisions. The strongest effect happens for low momentum tracks.

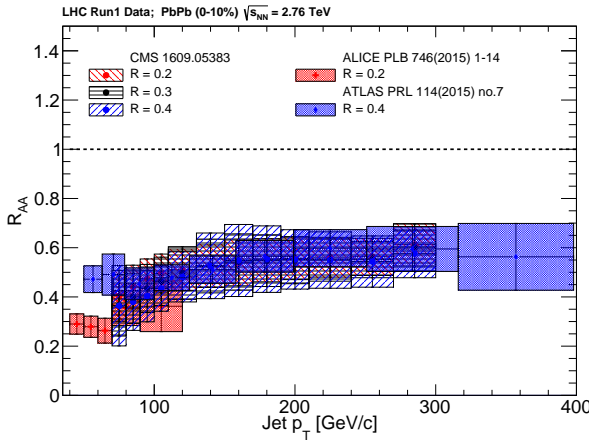


Figure 1.21: Reconstructed anti- $k_T$  jet  $R_{AA}$  from ALICE [160] with  $R = 0.2$  for  $|\eta| < 0.5$ , ATLAS [161] with  $R = 0.4$  for  $|\eta| < 2.1$ , and CMS [162] with  $R = 0.2, 0.3$  and  $0.4$  for  $|\eta| < 2.0$ . The ALICE and CMS data are consistent within uncertainties while the ATLAS data are higher. The experiments use slightly different methods in selecting jets and subtracting the underlying event contribution. Compared to ALICE and CMS the ATLAS technique could impose a survivor bias and lead to a higher jet  $R_{AA}$  at low momenta as argued in [6]. Figure from [6].

These observations are consistent with expectations from various energy loss models. Additionally it was observed that the broadening was stronger for subleading jets than for leading jets, which indicates a bias towards selecting less modified jets as the leading jet. Jet hadron correlations have also been studied at RHIC with similar conclusion [163].

### Phase-space view of the medium modified parton cascade

The new paradigm in jet quenching in heavy-ion collisions involves multi-scale problems [165, 166]. The elementary scattering and the subsequent branching process down to non-perturbative scales are dominated by hard scales in the vacuum as well as in the medium. Soft scales, of the order of the temperature of the medium, characterise the interactions of soft partons produced in the shower with the QGP. Soft scales also rule hadronisation, which is expected to take place in vacuum for sufficiently energetic probes, even though some modifications can persist from modifications of colour flow [167–169]. Understanding the contributions from the different processes to the jet shower evolution in medium and their scale dependence is crucial to constrain the dynamics of jet energy loss in the expanding medium, the role of colour coherence [170], and fundamental medium properties like temperature dependent transport coefficient [171, 172].

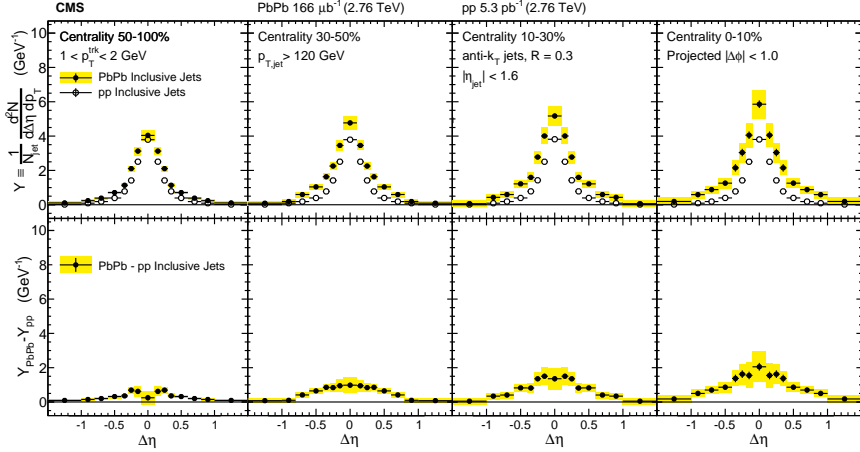


Figure 1.22: Measurement by CMS [164]. Symmetrized  $\Delta\eta$  distributions correlated with Pb–Pb and pp inclusive jets with  $p_T > 120 \text{ GeV}/c$  are shown in the top panels for tracks with  $1 < p_T < 2 \text{ GeV}/c$ . The difference between per-jet yields in Pb–Pb and pp collisions is shown in the bottom panels. These measurements indicate that the jet is broadened and softened, as expected. The effect is stronger in more central collisions.  $\Delta\phi$  correlations have similar trends. Figure from [164]

Let us now look at medium modification of jets in a  $\log(p) - \log(\theta)$  plane as shown in [165]. The different momentum and angular scales are subject to different physical phenomena. Figure 1.23 shows the relevant medium modification phenomena for different regions of the phase space at time  $t$ , when a jet propagates through a thermal cloud of temperature  $T$ . As in practice jets propagate over a finite path-length  $L$  in QCD matter, Figure 1.23 can be taken as a representation of the distribution of partonic jet fragments at moment  $t \approx L$ , when the jet escapes the medium [165].

The region marked as DGLAP is dominated by the primary vacuum splittings explained in section 1.4.2. This region is determined by  $\theta > \theta_{\text{vac}}$  with

$$\theta_{\text{vac}} \propto \frac{1}{\sqrt{p_T}}. \quad (1.36)$$

Medium-induced parton branching fills the  $\log p$ - $\log \theta$ -plane from the bottom up (in  $p$ ) and from the inside out (in  $\theta$ ). This is because transverse momentum  $k_\perp$  is acquired by Brownian motion in the medium, such that it depends on the time  $t$  and the transport coefficient  $\hat{q}$ ,  $k_\perp^2 \propto \hat{q}t$ . The formation time constraint  $t \geq p/k_\perp^2 \approx p/\hat{q}t$  implies that medium-induced quanta can be formed in the region  $p \leq k_{\text{form}}$  where

$$k_{\text{form}}(t) = \hat{q}t^2. \quad (1.37)$$

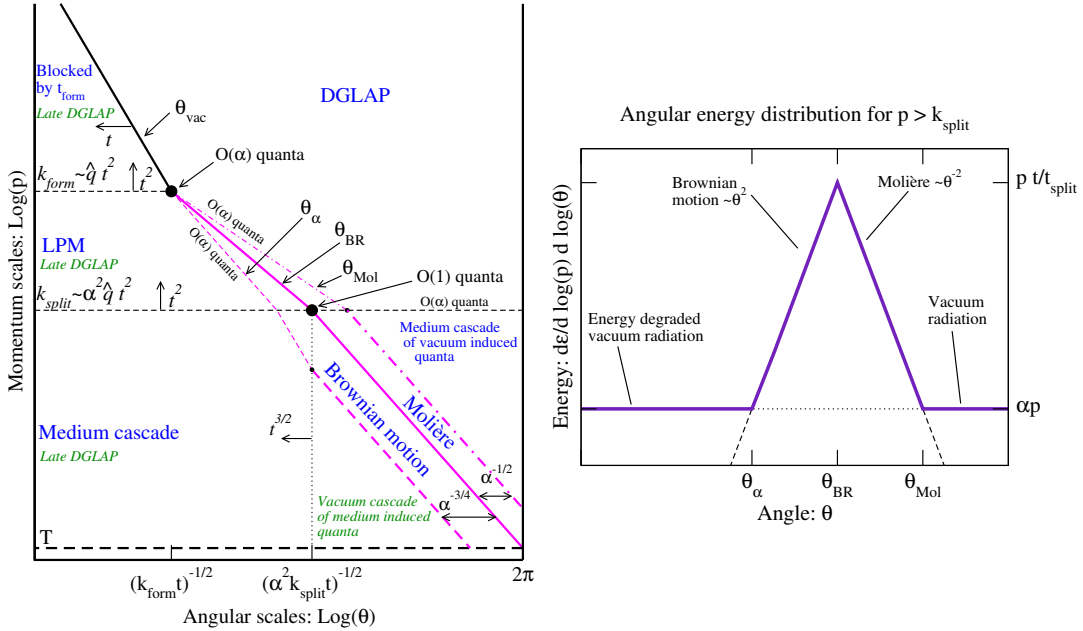


Figure 1.23: *Left:* Phase space view of dominant contributions in a medium-modified parton cascade. *Right:* The distribution of energy as a function of angle for a fixed momentum with  $p > k_{\text{split}}$ . Large angular scales  $\theta > \theta_{\text{Mol}}$  are dominated by DGLAP vacuum radiation from the leading parton at the scale  $Q$ . At  $\theta < \theta_\alpha$  the energy density is dominated by vacuum radiation of the leading parton after it has degraded its energy propagating through the medium. Areas  $\theta_\alpha < \theta < \theta_{\text{BR}}$  and  $\theta_{\text{BR}} < \theta < \theta_{\text{Mol}}$  are dominated by Brownian motion and rare large angle (Molière) scatterings with medium partons. Figures from [165].

For these splittees to survive without further splittings they must have

$$p \geq k_{\text{split}} \approx \alpha_s^2 k_{\text{form}}(t) \approx \alpha_s^2 \hat{q} t^2. \quad (1.38)$$

Thus the region marked as LPM in Figure 1.23 is filled by the primary medium-induced branchings. Fragments with  $p \leq k_{\text{split}}$  will have time to split further. An approximately equal splitting where both splittees get momentum  $p/2$  from the parent will degrade energy the most. These splittees will undergo the next splitting in an even shorter time scale producing even softer fragments. Momenta can continue cascading all the way to the thermal scale  $T$  of the medium within the same time scale within which the first splitting occurred. Thus filling the region marked as Medium cascade in Figure 1.23. Similarly splittees from vacuum radiation can cascade inside the medium when they have  $p \leq k_{\text{split}}$ , filling the bottom right corner of the  $\log p$ - $\log \theta$ -plane.

The angular distribution of the medium-induced radiation is driven by two

mechanisms; Multiple soft scatterings give rise to transverse Brownian motion, which determines the distribution at small angles. The typical angle reached in the LPM region is

$$\theta_{\text{BR}}(p) \approx \frac{\sqrt{\hat{q}t}}{p}, \text{ for } k_{\text{form}} > p > k_{\text{split}}, \quad (1.39)$$

while in the medium cascade region of the phase space this becomes

$$\theta_{\text{BR}}(p) \approx \left(\frac{T}{p}\right)^{\frac{3}{4}}. \quad (1.40)$$

Large angular scales cannot be reached by Brownian motion, but can arise from rare large angle scatterings with partons in the medium, described first by Molière [173]. The result is that medium-induced radiation is predominantly located in the bands marked as Brownian motion, where  $\theta_\alpha < \theta < \theta_{\text{BR}}$ , and Molière, where  $\theta_{\text{BR}} < \theta < \theta_{\text{Mol}}$  in Figure 1.23.

The hard parton will naturally continue radiating after it leaves the medium. As there is no longer kinematic limits set by the time scale, the vacuum radiation can extend to smaller angular scales in the phase space. The results is that the regions, where  $\theta < \theta_\alpha$ , marked as Late DGLAP in Figure 1.23 will be dominated by the late time vacuum radiation. Naturally also the splittees from medium-induced radiation will undergo the late stage vacuum radiation phase, filling the triangular region with small  $p$  and  $\theta < \theta_\alpha$ .

### Influence of jet on medium

Energy loss of hard partons is well established by experimental observations. Naturally energy can't just disappear, but is transferred to daughter partons or the medium. For radiation that stays inside the jet cone energy loss manifests itself as softening and broadening. If a daughter parton loses energy and becomes equilibrated with the medium it may no longer be correlated with the parent parton. This energy would then be distributed at distances far from the jet cone. There is some evidence for out-of-cone radiation by CMS [174], but the interpretation is not clear. Other possible phenomena include the mach cone and Molière scattering, but there is no experimental evidence for these. Evidence for all of these effects is difficult to find as the underlying event gives already a large and fluctuating background. Additionally its unclear how this energy would be different from the underlying event [6].

## 1.5 QGP in Small systems

After the existence of QGP in heavy-ion collisions has been established, attention has been turned to small systems. Proton-proton (pp) and proton-lead (p–Pb) collisions have been studied at LHC and RHIC has studied a host of different collision systems; namely proton–gold (p–Au) [175], deuteron–gold (d–Au) [176–179] and helium<sup>3</sup>–gold (<sup>3</sup>He–Au) [180] collisions starting from 2000.

Already before the era of modern colliders, collective behaviour in proton–proton collisions was considered by names like Heisenberg, Fermi and Bjorken [7]. Eventually there were some experimental searches of QGP in pp and  $p\bar{p}$  collisions in E735 at Tevatron [181] and MiniMAX [182]. However no conclusive evidence was found.

In the early years of RHIC these small systems were mostly considered as control measurement, for example in constraining nuclear modified parton distribution functions (nPDFs) that determine the initial gluon distributions that determine the first epoch of heavy-ion collisions [183, 184].

In 2010 ultrahigh-multiplicity pp collisions were studied at CMS [185]. The study found that particles had a weak but clear preference to be emitted along a common transverse  $\phi$  angle across all rapidities [186]. This seemed like similar to behaviour observed in A–A collisions, but it was argued that it could as well come from momentum correlations present in the earliest moments of the collision.

In 2012 LHC ran its first p–Pb data taking period. Around the same time d–Au data was re-examined at RHIC. Now it was revealed that most of the flow signatures attributed to hydrodynamic expansion in A–A collisions also existed in smaller systems.

### 1.5.1 Collective phenomena

The most rugged analysis of collective behaviour concerns the two (or more) particle correlations, often parametrised via the relative azimuthal angle and pseudorapidity differences,  $\Delta\phi$  and  $\Delta\eta$  respectively. Figure 1.24 shows two-particle correlations measurements in Pb–Pb, p–Pb and pp collisions at the LHC [187]. In Pb–Pb collisions long-range correlations dominate over short-range phenomena. This shows in the two ridges at  $\Delta\phi = 0$  and  $\Delta\phi = \pi$ . At  $\Delta\phi \approx \Delta\eta \approx 0$ , there is a peak coming from single jet fragmentation. Since the away-side jet can be spread out in  $\Delta\eta$ , this contribution disappears when compared to the flow contribution at the away side ridge. In p–Pb, and pp the near side peak is more distinguished and the away-side jet contribution starts to show. Still, one can see long-range correlations that seem like flow-like collective behaviour in both systems.

In addition to the two particle correlations, correlations have been observed in the form of  $v_n$  coefficients both at LHC [188] and at RHIC [175]. The results have

also been described with hydrodynamical models, although the applicability of said models might be questionable, because of the large Reynolds numbers in small systems [189, 190]. Figure 1.25 shows results for  $v_2$  in different collisions systems at RHIC as measured by PHENIX and Figure 1.26 shows the eccentricities and the resulting hydrodynamic evolution in the systems. These different systems provide also different initial geometries. d–Au collisions naturally have an ellipsoidal form, while a  ${}^3\text{He}$ –Au collision has a triangular form and thus produces larger triangular flow,  $v_3$  components.

Other observations that produce flow-like results include mass ordered  $v_2$  coefficients [192] and higher order harmonics coming from fluctuations in the initial geometry [188]. Thus all the major collective flow phenomena observed in heavy-ion collisions have been also identified in small systems.

One open question is identifying the point where flow-like correlations end. The question has proved challenging since low multiplicity events are dominated by non-flow phenomena. This makes observations in low multiplicity events model/method dependant. Different methods assess non-flow contributions differently. Thus some methods fail to observe a signal in cases, where others do and it is unclear whether this is true collective motion or it comes from non-flow contributions.

### 1.5.2 Absence of jet quenching

In A–A collisions, an important confirmation of the standard model comes from the energy loss of high  $p_T$  partons traversing the medium, as discussed in Section 1.4.5. Originally the interest in small systems was due to ruling out possible cold nuclear matter effects that might affect the results also in Pb–Pb. In 2003 the jet quenching effect was observed to disappear in d–Au collisions at

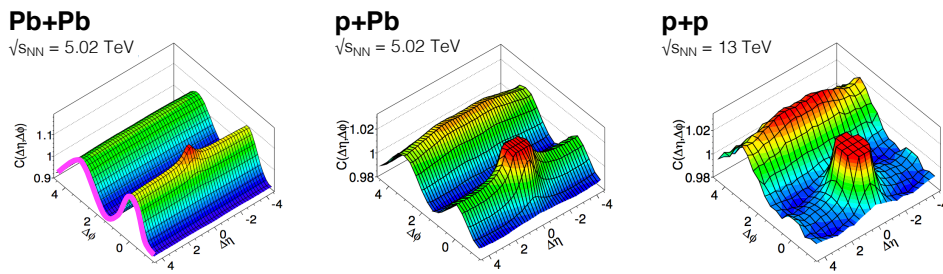


Figure 1.24: Two-particle correlation results in Pb–Pb , p–Pb , and pp collisions at the LHC [187]. This figure has been reprinted from [7] with kind permission from Annual Reviews.

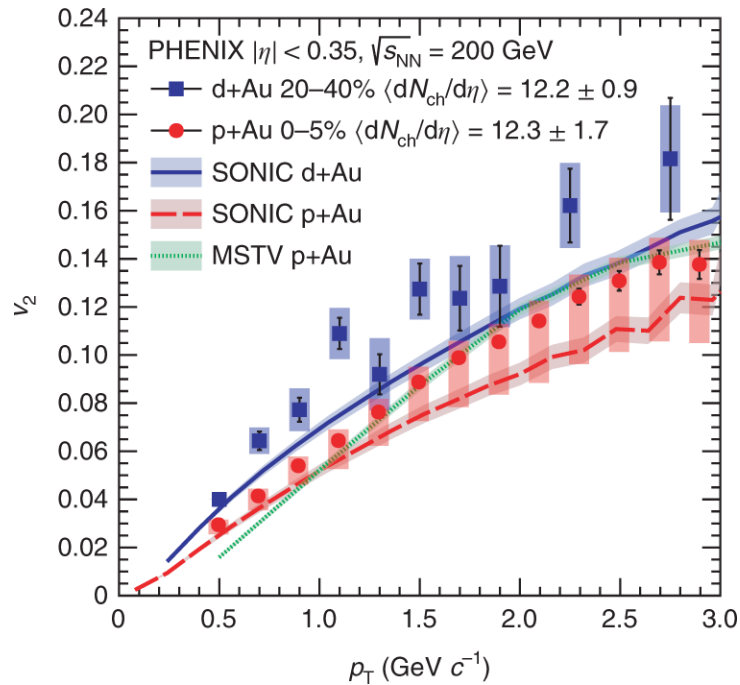


Figure 1.25: Comparison between hydrodynamic calculations and data from p–Au, d–Au and  ${}^3\text{He}$ –Au collisions. This figure has been reprinted from [191] with kind permission from Springer Nature.

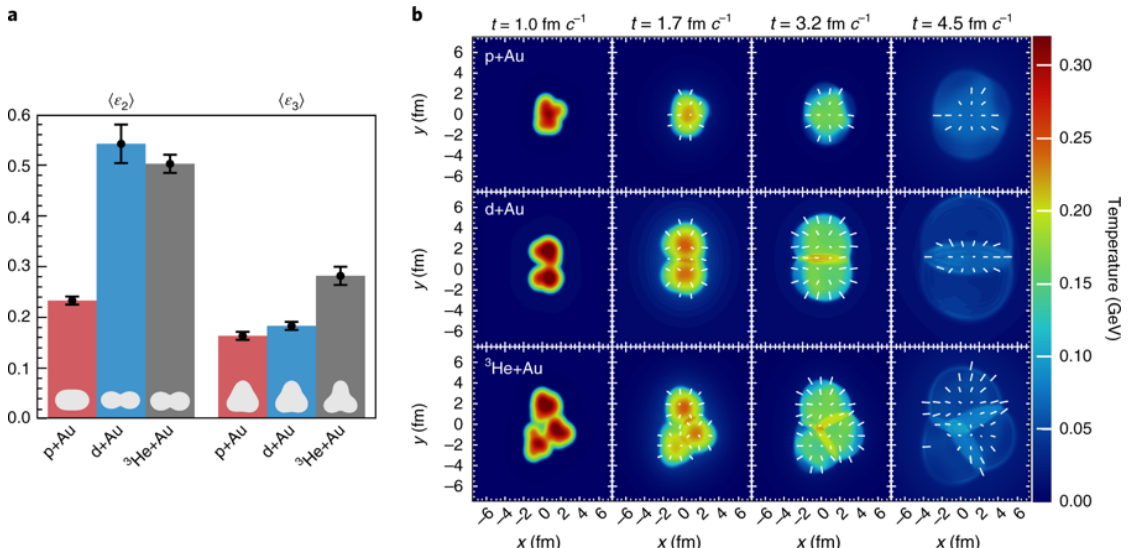


Figure 1.26: *left:* Eccentricities in different systems. *right:* Calculations of the initial energy density in small collision systems at RHIC and the resulting hydrodynamic evolution. This figure has been reprinted from [191] with kind permission from Springer Nature.

RHIC [176–179]. This was taken as an indication that no QGP was created. Similarly at LHC no jet modification has been observed in p–Pb collisions. Figure 1.27 shows the nuclear modification factor  $R_{pA}$  and  $v_2$  in p–Pb collisions as measured at the LHC [193, 194].

Now the lack of jet modification seems surprising considering the multitude of flow observations supporting the existence of QGP in small systems. One possible explanation is simply the size of medium. In Pb–Pb collision partons traversing through the medium lose energy to the medium. If the medium is very small there is limited time for interaction with the medium. Reaction plane dependent  $R_{AA}$  measurements [140] in Pb–Pb collisions indicated that 2 fm could be the minimum path length required for energy loss.

Some calculations [195–197] indicate that there should be modification in the most central p–Pb collisions, but selecting these in the analysis is complicated [7]. In Pb–Pb collisions most of the particle production comes from the medium and thus the total multiplicity is a good indicator of centrality. However in p–Pb collisions the total multiplicity is smaller and is more strongly influenced by jet phenomena. Events with jets have naturally larger multiplicities and are more likely to be classified as central events.

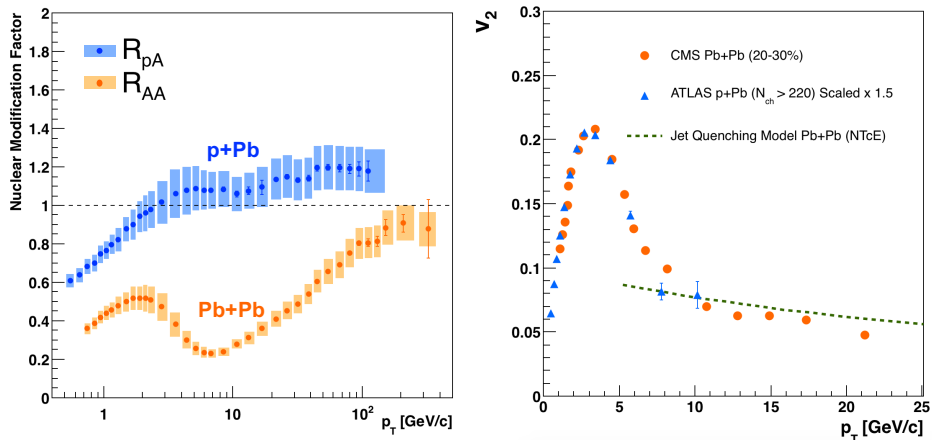


Figure 1.27: *left:* The nuclear modification factor  $R_{pA}$  in p–Pb collisions [193]. Compared to  $R_{AA}$   $R_{pA}$  shows no sign of modification. *right:* The  $v_2$  coefficient as a function of  $p_T$  in Pb–Pb and p–Pb collisions at the LHC [194, 198]. For shape comparison the p–Pb results have been scaled up by a factor 1.5. The green dotted curve [195] is a prediction from a jet quenching calculation where the anisotropy is driven by the directional dependence of the energy loss, rather than by hydrodynamic flow. This figure has been reprinted from [7] with kind permission from Annual Reviews.

So far the only observable indicative of jet quenching in p–Pb collisions is the high  $p_T v_2$ . In heavy-ion collisions this is not explained by hydrodynamics. Instead it is assumed to come from jet quenching with different path lengths through the medium in different directions. In Figure 1.27 ATLAS [194] and CMS [198] measurements of  $v_2$  in p–Pb and Pb–Pb collisions are shown. The p–Pb results seem to follow a very similar pattern. However, the non-flow effects in this high- $p_T$  region are not fully under control, so the physical interpretation is still under debate.

### 1.5.3 Centrality determination in small systems

In lead-lead collisions the total multiplicity of the event is a good indicator of the geometric centrality of the collision [84]. In proton-lead collisions the connection between multiplicity and centrality is less clear [199]. In p–Pb collisions the impact parameter is only loosely correlated to  $N_{\text{part}}$  or  $N_{\text{coll}}$ . Hence, although the term centrality is commonly used to refer to these measurements, the relevant parameters are  $N_{\text{part}}$  and  $N_{\text{coll}}$  [199].

As in Pb–Pb collisions the Glauber model [80] is generally used to calculate geometrical quantities of p–Pb collisions. In the Glauber model, the average number of participating nucleons  $N_{\text{part}}$  and the corresponding number of collisions  $N_{\text{coll}}$  are controlled by the impact parameter  $b$ . It is expected that fluctuations in the amount of matter in the collision region will change the number of produced

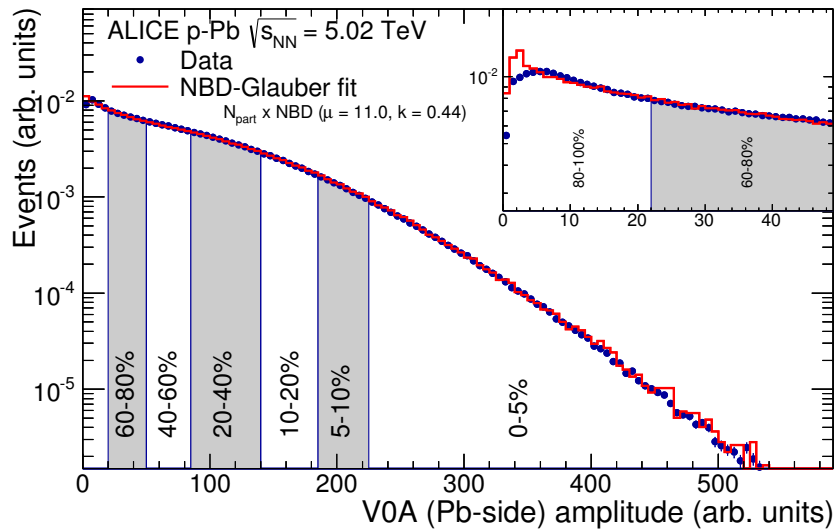


Figure 1.28: Distribution of the sum of amplitudes in p–Pb collisions in the V0A hodoscopes of ALICE (Pb-going side), as well as the NBD-Glauber fit. The vertical lines separate the centrality classes. Figure from [199].

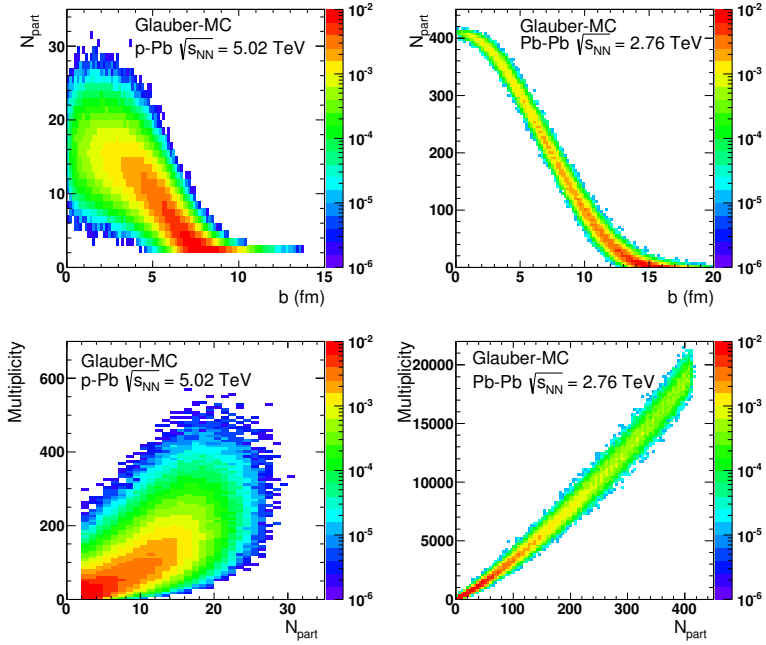


Figure 1.29: *Top*: Scatter plot of number of participating nucleons versus impact parameter; *Bottom*: Scatter plot of multiplicity versus the number of participating nucleons from the Glauber fit for V0A. The quantities are calculated with Glauber Monte Carlo simulations of p–Pb (left) and Pb–Pb (right) collisions. Figure from [199].

particles, and parameters such as  $N_{\text{part}}$  and  $N_{\text{coll}}$  have traditionally been used to describe those changes quantitatively, and to relate them to pp collisions. Figure 1.28 shows the measured V0A amplitude distribution in ALICE and the best NBD Glauber fit to the distribution [199].

The problem in p–Pb collisions is that fluctuations in multiplicity coming from for example hard scatterings are of the same order as the differences in multiplicity between centrality classes. In Pb–Pb collisions these multiplicity fluctuations have little influence on the centrality determination as the range of  $N_{\text{part}}$  or  $N_{\text{coll}}$  is large and both  $P(M|N_{\text{part}})$  and  $P(M|N_{\text{coll}})$  converge quickly to a Gaussian with a small width relative to the range of  $N_{\text{part}}/N_{\text{coll}}$ . This is illustrated in Figure 1.29. In practice selecting high multiplicity in p–Pb one chooses not only large average  $N_{\text{part}}$ , but also positive multiplicity fluctuations leading to deviations from the binary scaling of hard processes. These fluctuations are partly related to qualitatively different types of collisions. High multiplicity nucleon-nucleon collisions show a significantly higher mean transverse momentum. They can be understood either as harder collisions with larger momentum transfer  $Q^2$  or as nucleon-nucleon

collisions where multiple parton-parton interactions (MPI) take place.

For centrality estimation particularly useful are estimators from kinematic regions that are causally disconnected after the collision. The measurement of a correlation between them unambiguously establishes their connection to the common collision geometry. Typically these studies are performed with observables from well separated pseudorapidity ( $\eta$ ) intervals, e.g. at zero-degree (spectators, slow-nucleons, deuteron break-up probability) and multiplicity in the rapidity plateau.

In ALICE one centrality selection that is argued not to induce a bias on the binary scaling of hard processes is provided by the energy measurement with the Zero Degree Calorimeters (ZDC), due to their large  $\eta$ -separation from the central barrel detectors. They detect the "slow" nucleons produced in the interaction by nuclear de-excitation processes or knocked out by wounded nucleons [200].

In events containing high- $p_T$  particles, from hard scatterings, additional kinematic biases can arise. The contribution of high momentum tracks from hard processes to the overall multiplicity increases with increasing parton energy, which can introduce a correlation between the centrality estimator and the presence high- $p_T$  tracks in the event. In very peripheral collisions this contribution can dominate over the bulk production of soft collisions, pushing these events to higher multiplicities, which produces an effective veto veto on hard processes for peripheral collisions. For the nuclear modification factor this would lead to  $R_{p\text{Pb}} < 1$  [199].

# Chapter 2

## Experimental Setup

### 2.1 CERN

The European Organization for Nuclear Research (CERN), established in 1954, operates the largest particle physics laboratory in the world. In 2019 CERN consists of 22 member states. Additionally CERN has contacts with a number of associate member states and various individual institutions. The laboratory, also referred to as CERN, itself is located near Geneva at the border between Switzerland and France employs about 2500 people. Additionally some 12000 visiting scientists from over 600 institutions in over 70 countries come to CERN for their research [201].

The laboratory includes a series of accelerators, which are used to accelerate the particle beams used. A schematic view of the complex as of 2019 is shown in Figure 2.1. In the framework of this thesis the most important component is the Large Hadron Collider (LHC), the largest collider in the world. LHC will be discussed in more detail in Section 2.2. Other accelerators in the series are used to inject the particle beams into LHC, but they are also used in itself for various experimental studies.

The second largest accelerator is the Super Proton Synchrotron (SPS). It is the final step before the particle beam is injected into LHC. Commissioned in 1976, it was the largest accelerator at CERN until the Large Electron-Positron Collider (LEP) was finished in 1989. Originally it was used as a proton-antiproton collider and as such provided the data for the UA1 and UA2 experiments, which resulted in the discovery of the W and Z bosons [203]. At the moment there are several fixed target experiments utilising the beam from the SPS. These study the structure (COMPASS [204]) and properties (NA61/SHINE [205]) of hadrons, rare decays of kaons (NA62 [206]) and radiation processes in strong electromagnetic fields (NA63 [207]). Additionally the AWAKE (Advanced Proton Driven Plasma

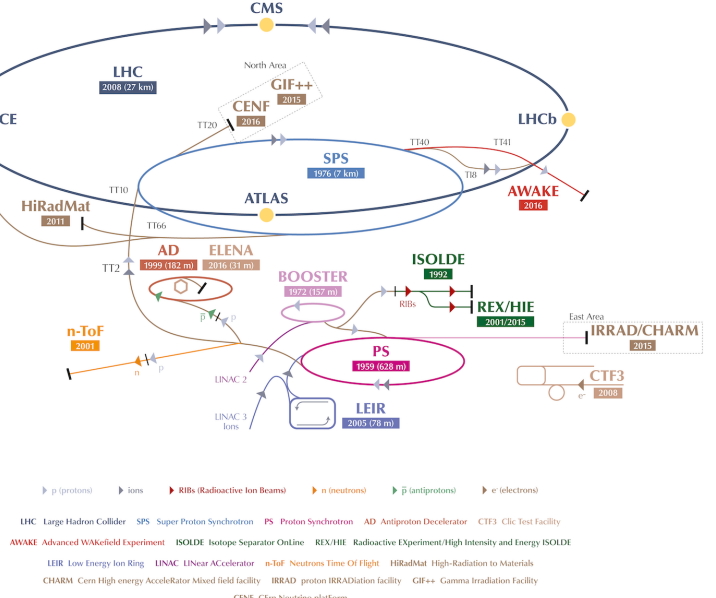


Figure 2.1: A schematic view of the accelerator complex at CERN. Before particles can be injected into the LHC they require a series of accelerators with increasing size. Until 2018 protons started their journey in LINAC2 (Linear Accelerator) and continue through the Booster, Proton Synchrotron (PS) and Super Proton Synchrotron (SPS). Between 2019 and 2020 LINAC2 will be replaced by LINAC4. Figure from [202].

Wakefield Acceleration Experiment) [208] and UA9 [209] experiments are used for accelerator research and development.

The third largest accelerator in CERN is the Proton Synchrotron (PS). Capable of accelerating beams up to an energy of 25 GeV PS provides the beam to SPS. Additionally PS has experiments for studying strong force (DIRAC [210]), the effect of cosmic rays on cloud formation (CLOUD [211]) and neutron-nucleus interactions (nTOF [212]).

Additionally PS provides the beam to the Antiproton Decelerator, which collides the beam with a block of metal to produce antiprotons. These are then decelerated in the decelerator into a useful low-energy beam, which is provided to a host of experiments studying the properties of antimatter.

PS gets proton beams from LINAC2 through BOOSTER and ion beams from LINAC3 through LEIR. From BOOSTER beams are also provided to the On-Line Isotope Mass Separator (ISOLDE). ISOLDE directs the beam into thick targets

to produce low energy beams of radioactive nuclei. These beams are used to study the properties of even the most exotic of atomic nuclei in a host of experiments.

More information of the various experiments at CERN can be found online in [213].

## 2.2 Large Hadron Collider

The Large Hadron Collider (LHC) [214, 215] with its circumference of 26.7 km is the largest accelerator at CERN and the largest particle collider ever built. The LHC is designed to accelerate protons up to an energy of 8 TeV and lead ions up to centre-of-mass energies of 5.02 TeV per nucleon. The design luminosity of the LHC is  $10^{34} \text{ cm}^{-2}\text{s}^{-1}$ . In 2017 it achieved a record peak luminosity of  $2 \cdot 10^{34} \text{ cm}^{-2}\text{s}^{-1}$  which was also reached in 2018. For lead beams luminosities of up to  $6 \cdot 10^{27} \text{ cm}^{-2}\text{s}^{-1}$  were reached in 2018. All this is achieved with a ring consisting of 1232 superconducting dipole magnets that keep particles in orbit.

The LHC receives beams with energies of 450 GeV from the SPS. In the LHC the particles are accelerated through the use of radio-frequency (RF) cavities. Inside these cavities electromagnetic waves become resonant and an electromagnetic field builds up. As it consists of electromagnetic waves, the field in the RF cavity oscillates. Charges passing through the cavity feel the overall force and are pushed forward along the accelerator. Particles must enter the cavity at the correct phase of oscillation to receive a forward push. When tuned correctly, the particles will feel zero accelerating potential when they have the exact correct energy. Particles with lower energies will be accelerated and particles with higher energies will be decelerated. This collects particles in distinct bunches. The RF oscillation frequency at the LHC is 400.8 MHz. Thus RF "buckets" are separated by 2.5 ns. However only 10 % are actually filled with particles, so the bunch spacing in the LHC is 25 ns, at a bunch frequency of 40 MHz [214].

With 7 TeV proton beams the dipole magnets used to bend the beam must produce a magnetic field of 8.33 T. This can be only achieved through making the magnets superconducting, which requires cooling them down with helium to a temperature of 1.9 K. The 1232 dipole magnets make up roughly 2/3 of the LHC circumference. The remaining part is made up of the RF cavities, various sensors and higher multipole magnets used to keep the beam focused. The most notable of these are the 392 quadrupole magnets [214].

The LHC is divided into eight sections, or octants, where each section has a distinct function. Octants 2 and 8 are used to inject beam into the LHC from SPS. The 2 beams are crossed in octants 1,2,5 and 8. The main experiments are built around these crossing points. Octants 3 and 7 are used for beam cleansing. This is achieved through collimators that scatter particles with too high momentum

or position offsets off from the beam. Octant 4 houses the RF cavities used for acceleration and octant 6 is used for dumping the beam. The beam dump is made up of two iron septum magnets, one for each beam, that will deflect the beam into an absorber away from machine components.

### 2.2.1 LHC experiments

As of 2018 there are four main experiments at the LHC; ALICE [216], ATLAS [217], CMS [218] and LHCb [219] and three smaller ones LHCf [220], TOTEM [221] and MoEDAL [222]. ALICE will be covered in detail in Section 2.3.

ATLAS (A Toroidal LHC ApparatuS) [217] and CMS (Compact Muon Solenoid) [218] are the two largest experiments at the LHC. They are both multipurpose experiments designed to look for a host of possible new physics signals, such as extra dimensions and dark matter particles. So far the biggest discovery made by the LHC is the discovery of the Standard Model Higgs boson, which was simultaneously published by ATLAS and CMS in 2012 [223, 224].

The LHCb (LHC beauty) experiment [219] is made for studying the bottom (beauty) quark. Main physics goals of the LHCb include the measurement of the parameters of CP violation with decays of hadrons containing the bottom quark. One of the most important results published by LHCb is the first measurement of  $B_s^0 \rightarrow \mu^+ \mu^-$  decay [225, 226], which was found to agree with the Standard Model predictions. More recently LHCb published the discovery of a pentaquark state [37].

In addition to the four large experiments the LHC serves three smaller experiments. LHCf (LHC forward) [220] is located at interaction point 1 with ATLAS. It uses particles thrown forwards from the collision point to simulate cosmic rays.

TOTEM (TOTal Elastic and diffractive cross section Measurement) is located near the CMS experiment at point 5. This allows it to measure particles emerging from CMS with small angles. TOTEM focuses on measuring the total, elastic and inelastic cross-sections in pp collisions [221].

The MoEDAL (Monopole and Exotics Detector At the LHC) experiment [222] is located at the interaction point 8 together with the LHCb experiment. MoEDAL attempts to hunt for signatures of magnetic monopoles, hypothetical particles that have a magnetic charge.

## 2.3 ALICE

ALICE (A Large Ion Collider Experiment) [216] is the dedicated heavy-ion experiment at the LHC. ALICE was designed to cope with the expected very high multiplicity production of heavy-ion collisions. The design allows measurement of

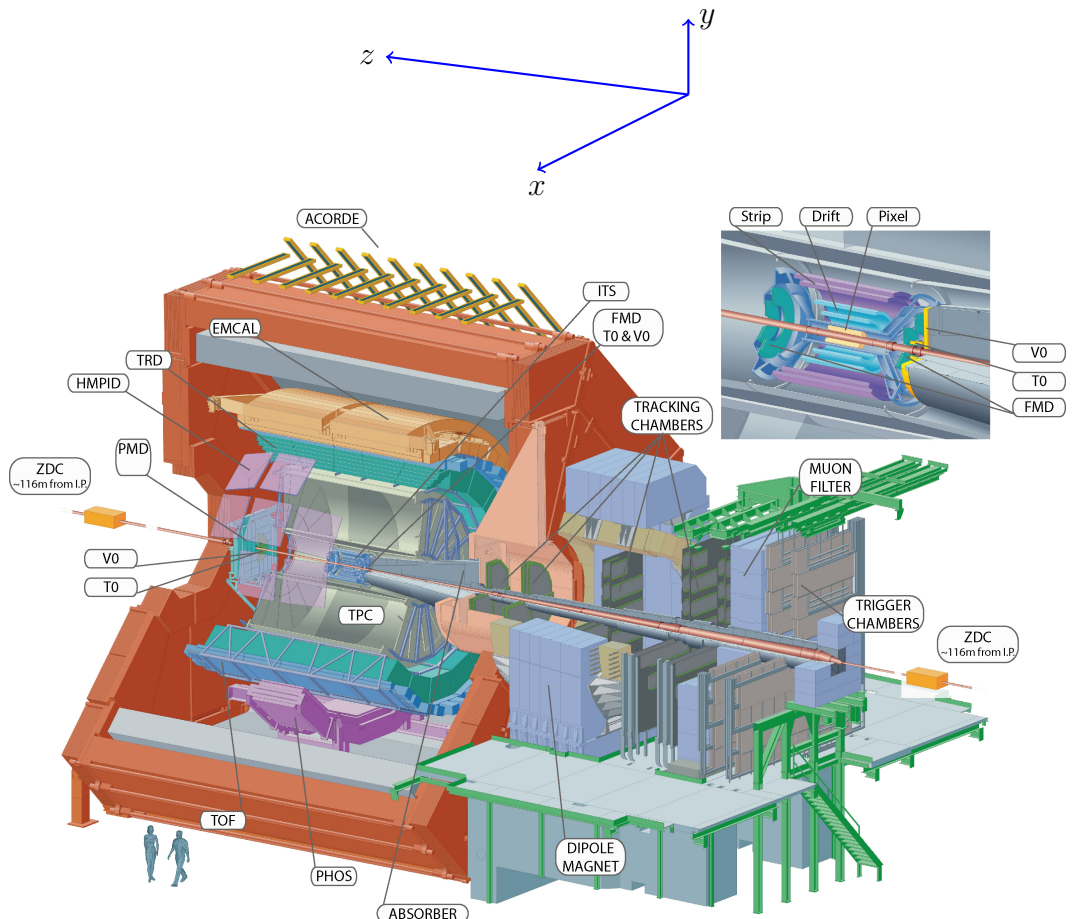


Figure 2.2: Schematic view of the ALICE detector with the definition of coordinates. The positive direction of  $z$  is also referred to as the A side and the negative direction as the C side.

a large number of low momentum tracks. The different detector subsystems are optimised to provide high momentum resolution and good particle identification capabilities over a wide momentum range.

A schematic view of the ALICE detector in 2018 is presented in Figure 2.2. This section will go through the composition of ALICE as it has been during run 2 between 2014 and 2018. The detector will go through significant upgrades during Long Shutdown 2 (LS2) in 2019-2020.

As in all the major high energy physics experiments the positioning of the detectors follows a layered structure. The first layer outside the interaction point consists of the tracking detectors. The main task of these detectors is to record the tracks of charged particles and to locate the position of the primary interaction

vertex accurately. To achieve this they need a very good spatial resolution close to the interaction point. Tracking detectors are such that they do not significantly alter the tracks of traversing particles. Thus they can be located in the innermost layers.

Calorimeters are designed to stop particles hitting them and thus use the absorption to measure the energy of the particles. Thus they must be located behind the tracking detectors. ALICE has two separate calorimeter systems, the electromagnetic calorimeters measure mainly electrons and photons, while the muon detection system measures muons.

### 2.3.1 Tracking detectors

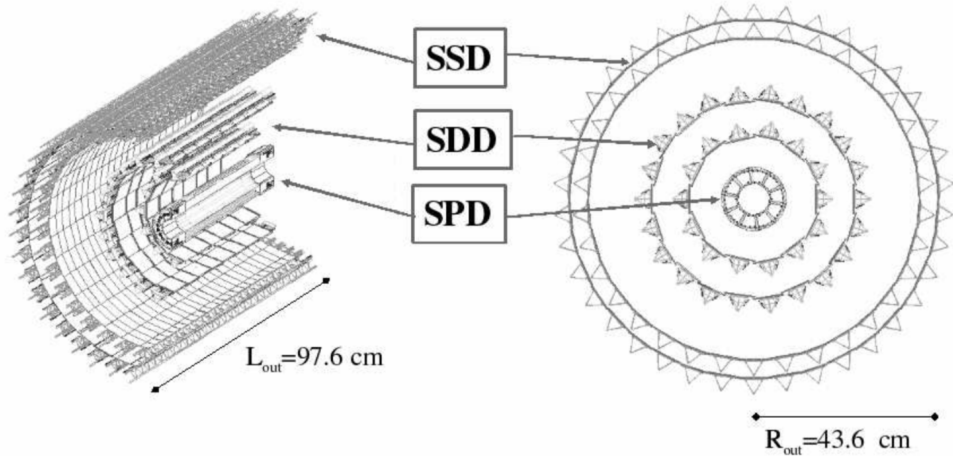


Figure 2.3: Schematic view of ALICE Inner Tracking System. Figure from [216].

The main design guideline for the tracking detectors in ALICE was the requirement to have good track separation and high granularity in the high multiplicity environment of heavy-ion collisions. Before the LHC started heavy-ion runs the most extreme estimates put the particle density at 8000 charged particles per unit of rapidity [216]. In reality the particle density turned out to be significantly smaller, about 1600 charged particles per rapidity unit [227].

The main tracking detector in ALICE is the Time Projection Chamber (TPC) [228]. TPC is discussed in more detail in Section 2.3.2.

Inside the TPC, just around the interaction point there is a set of six layers of silicon detectors, together called the Inner Tracking System (ITS) [229]. ITS can locate the primary vertex with a resolution better than  $100 \mu\text{m}$  and reconstruct the secondary vertices from decaying particles. It can provide tracking and particle

identification for particles with momenta below 200 MeV and complement the momentum and angle measurements of TPC. During long shutdown 2 in 2019-2020 the entire ITS will be replaced [230]. As of 2018 the two innermost layers are made of the Silicon Pixel Detector (SPD). As it is the closest detector to the interaction point it requires a very high spatial resolution. Thus the choice of pixel technology is natural. In heavy-ion collisions the particle density is around 50 particles per  $cm^2$ .

The next two layers together are the Silicon Drift Detector (SDD). The layers are made out of homogeneous neutron transmutation doped silicon, that is ionised when a charged track propagates through the material. Within a time  $5\ \mu s$  the generated electrons then drift to the collection anodes, where it is measured. This design gives very good multi-tracking capabilities and provides two out of the four  $dE/dx$  samples in the ITS.

The two remaining layers in the ITS are the Silicon Strip Detector (SSD). The strips is based on the same technology as silicon pixels, but by itself one layer only provides good resolution in one direction. Combining two crossing grids of strips provides 2 dimensional detection. Each charged particle will hit two intervening strips and their crossing location gives the position of the hit.

### 2.3.2 TPC

The Time Projection Chamber (TPC) is a cylindrical detector filled with  $88\ m^3$  of Ne – CO<sub>2</sub> (90/10 %) gas mixture. The gas is contained in a field cage that provides a uniform electric field of  $400\ V/cm$  along the z-axis. The gas content and field strength have been chosen for optimised charge transport, signal amplification and transparency for traversing particles [231]. Charged particles traversing through the TPC volume will ionise the gas along their path. This liberates electrons that drift towards the end plates of the cylinder. A schematic of the TPC is shown in Figure 2.4.

The field cage is separated into two detection volumes by the central high voltage electrode. Both sides have a drift length of 2.5 m and inner and outer diameters of 1.2 m and 5 m respectively. To provide the uniform electric field of  $400\ V/cm$  the central electrode must provide a potential of 100 kV. The maximum time required for electrons to drift through the chamber is about  $90\ \mu s$ .

When electrons reach the endplates of the main cylinder they enter the readout chambers. The readout section of both sides consists of 18 outer chambers and 18 inner chambers. Each of them is made of multiwire proportional chambers with cathode pad readouts. This design has been used in many TPCs before. During LS2 in 2019-2020, the multiwire chambers will be replaced by Gas Electron Multipliers (GEMs, see Section 2.4).

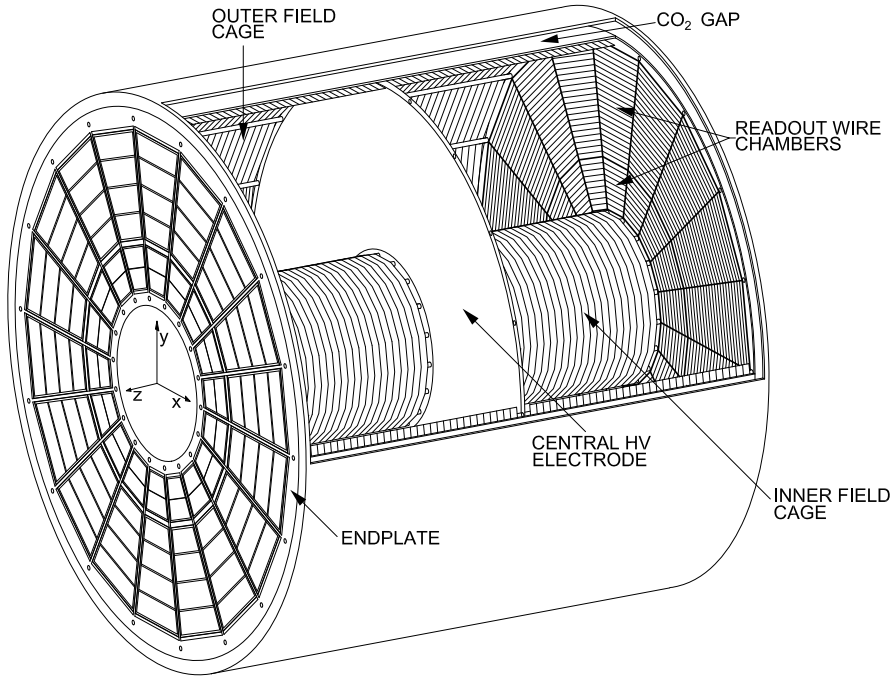


Figure 2.4: Schematic view of ALICE Time Projection Chamber. Figure from [231].

### 2.3.3 Particle identification

One guiding principle in the design of ALICE was to achieve good particle identification (PID) over a large momentum range and for several particle types. In ALICE there are several detectors taking part in the identification of particles. In addition to the specific particle identification detectors, the general purpose tracking detectors can be used for identification through the use of specific energy loss  $dE/dx$  of charged particles traversing through a medium and the transition radiation emitted by charged particles when crossing the boundary between two materials.

Energy loss measurements are provided by the last four layers of the ITS detector, i.e. the SDD and the SSD, thanks to their analog readout [232]. ITS can provide particle identification in the low  $p_T$  region, up to 1 GeV/c, and pions reconstructed in the standalone mode can be identified down to 100 MeV. Similar to ITS the TPC detector provides specific energy loss measurements. TPC can identify charged hadrons up to  $p_T$  1 – 2 GeV/c as well as light nuclei, He<sup>3</sup> and He<sup>4</sup>, providing the majority of PID information for ALICE.

One of the particle identification detectors is the Transition Radiation Detector (TRD) [233]. TRD is used to identify electrons with momenta larger than

$1\text{ GeV}/c$ . ALICE TRD is made of a composite layer of foam and fibres. Detection is based on the transition radiation which is produced when highly relativistic particles traverse the boundary between two materials that have different dielectric constants.

The average energy of emitted photons is approximately proportional to the Lorentz factor  $\gamma$  of the particle, which allows discriminating between electrons and pions. The TRD uses six layers of time expansion wire chambers filled with Xe/CO<sup>2</sup> to measure the emitted photons.

The Time-of-Flight (TOF) detector [234] uses a very simple physics principle, i.e. calculating the velocity of the particle using the time-of-flight between two points. Combining this with the momentum of the particle, obtained from the tracking detectors, one can calculate the mass of the particle, which identifies particles. Physically the detector consists of multigap resistive wire chambers, which are stacks of resistive plates spaced equally. This construction allows time-of-flight measurements with a resolution better than 100 ps and in large acceptance with high efficiency.

The third specific particle identification detector is the High Momentum Particle Identification (HMPID) detector [235]. The HMPID uses a ring imaging Cherenkov counter to identify particles with momenta larger than  $1\text{ GeV}/c$ . Particles moving through a material faster than the speed of light in a material will produce Cherenkov radiation. The velocity of the particle determines the angle at which the radiation is emitted. Thus the velocity of the particle is given by measuring this Cherenkov angle. This can be again used to calculate the mass of the particle, if the momentum is known. In HMPID the material is a liquid radiator and the photons are measured with multiwire proportional chambers in conjunction with photocathodes.

### 2.3.4 Electromagnetic Calorimeters

Calorimeters are used to measure the energy of particles. Electromagnetic calorimeters specialise in detecting particles that interact primarily through the electromagnetic interaction, in practice photons and electrons. They are required in many neutral meson [236] and direct photon [237] analyses. In addition the energy information enhances jet measurements [238], as some of jet fragments can't be detected with trackers.

ALICE has two electromagnetic calorimeter systems, the Photon Spectrometer (PHOS) [239] and the Electromagnetic Calorimeter (EMCal) [240]. PHOS is a homogeneous calorimeter that consists of scintillating PbWO<sub>4</sub> crystals, which generate a bremsstrahlung shower and produce scintillation light. The energy of the particle determines the amount of light produced. To improve the charged particle rejection, PHOS includes a charged particle veto detector (CPV) [239].

The high granularity build of PHOS allows measuring direct photons and neutral mesons well.

In comparison to PHOS, EMCAL is built with a coarser granularity, but a significantly larger acceptance, making it more suitable for jet physics. The acceptance of EMCAL in the azimuthal angle is  $80 \text{ deg} < \phi < 187 \text{ deg}$ . During long shutdown 1 in 2013-2015, EMCAL was complemented by the Di-jet calorimeter (DCal) [241], giving an additional acceptance region of  $260 \text{ deg} < \phi < 320 \text{ deg}$ . This provides partial back-to-back coverage.

EMCal is segmented into 10 full size super modules (SM), 5 for A side and 5 for C side, and two  $1/3$  sized SMs, one for each side. This segmentation can be seen in Figure 2.5. Each SM is divided into 24 strips, each covering full  $\phi$  (24 towers) and 2 towers in  $\eta$ . Each strip is composed of  $2 \times 2$  tower modules. Thus each full size super module includes 1152 towers and in total the EMCAL is made up of 12288 towers.

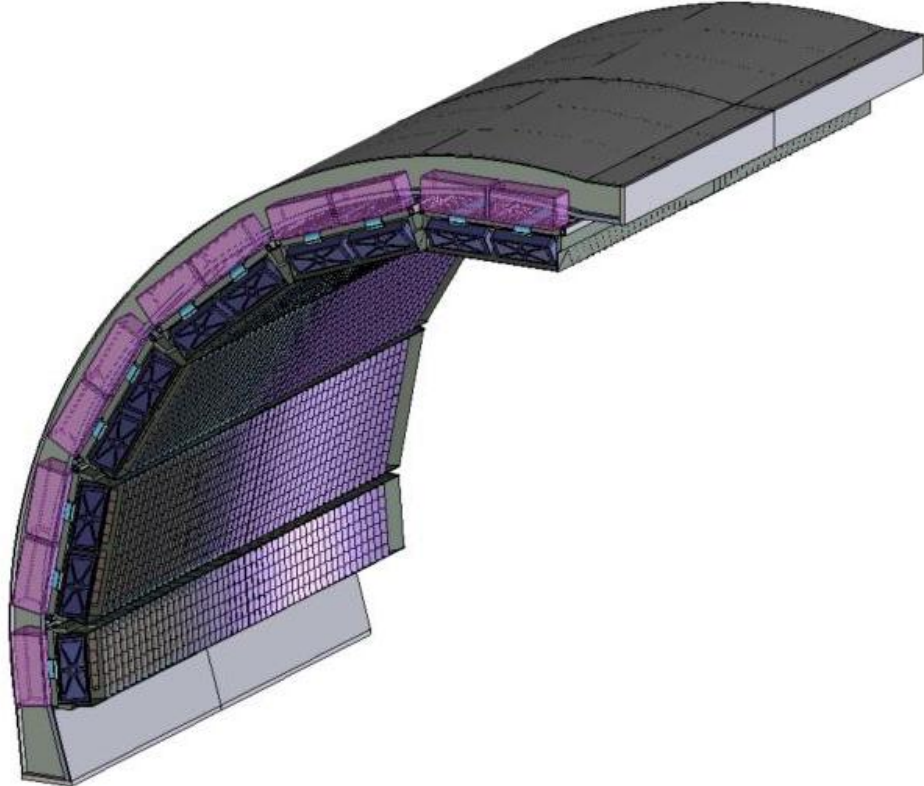


Figure 2.5: The EMCAL detector arc, where the segmentation into 10 full size and 2  $1/3$ -sized (5 and 1 per side) supermodules can be seen. Figure from [240]

The build of individual towers is shown in Figure 2.6. Each tower consists of 76

alternating layers of 1.44 mm lead and 77 layers of 1.76 mm scintillator material. The lead tiles produce a shower which turns into light in the scintillator tiles. Each tower scintillator is equipped with reflectors on all sides to provide better gain and isolation from other towers inside one module. The photons produced in the scintillators of the tower are collected by 36 longitudinally placed wave length shifting light guide fibres. The light is eventually directed to the Avalanche Photo Diodes (APD) for readout.

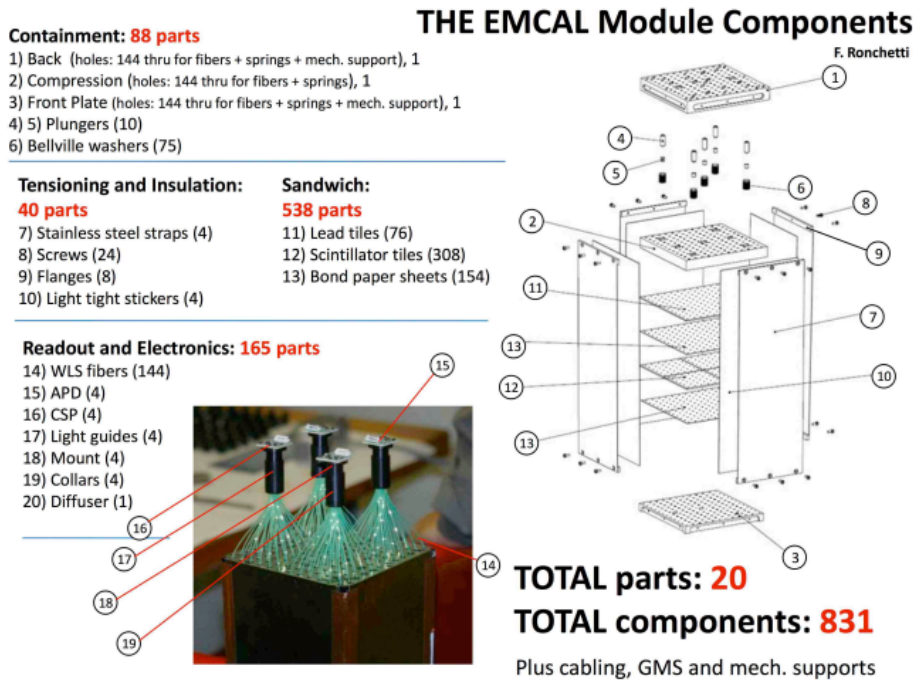


Figure 2.6: The exploded EMCAL tower view. Figure from [240].

### 2.3.5 Forward and trigger detectors

ALICE includes a few small and specialised detectors of importance. The T0 detector [242] is used to determine the event time with very good precision ( $< 25 \text{ ns}$ ). The detector consists of two sets of Cherenkov counters on both sides of the interaction point around the beam pipe. T0 is also used to obtain the luminosity measurement in ALICE.

A similar detector in the forward direction is the V0 [242], which consists of two arrays of segmented scintillator counters. Covering a range of  $-3.7 < \eta < -1.7$

and  $2.8 < \eta < 5.1$  V0 is used as a minimum bias trigger and for rejection of beam-gas background. Particle multiplicity in the forward direction can be related to the event centrality. Thus the main centrality information in Pb–Pb collisions comes from V0. The two sides of V0 are referred to as V0A (positive  $\eta$ ) and V0C (negative  $\eta$ ).

The multiplicity measurement of V0 is complemented by the Forward Multiplicity Detector (FMD) [242], which includes five rings of silicon strip detectors. FMD gives acceptance in the ranges  $-3.4 < \eta < -1.7$  and  $1.7 < \eta < 5.0$ .

During long shutdown 2 in 2019–2020, V0 and T0 will be replaced by the Fast Interaction Trigger (FIT) detector [243]. For historical reasons elements of FIT are also referred to as V0+ and T0+. FIT will allow centrality, event plane, luminosity and interaction time determination in the continuous readout mode, that ALICE will operate in after 2020.

For photon multiplicity measurement ALICE has the Photon Multiplicity Detector (PMD) [244]. PMD uses two planes of gas proportional counters with a cellular honeycomb structure. PMD gives the multiplicity and spatial distribution of photons in the region  $2.3 < \eta < 3.7$ .

The only hadronic calorimeters in ALICE are the Zero Degree Calorimeters (ZDC) [245]. ZDC consists of two sets of calorimeters which are located close to the beam pipe about 116 m from the interaction point. One set of calorimeters is made of brass, specialising in measuring protons, while the other, made of tungsten, is sensitive to neutrons.

ZDC is meant to detect spectators, i.e. partons of the colliding nuclei that do not interact with the other nucleus. If there are more spectators, the collisions is likely to be more peripheral. Thus ZDC gives information about the centrality of the event especially in proton-lead collisions [199], but also in Pb–Pb collisions [84].

During long shutdown 1 the ALICE Diffractive detector (AD) [246] was installed. AD consists of two sets of scintillators, one on both sides of the interaction point. These assemblies are situated about 17 m and 19.5 m away from the interaction point. The pseudorapidity coverage is  $-6.96 < \eta < -4.92$  and  $4.78 < \eta < 6.31$ . AD improves ALICE’s capability for diffractive physics measurements that require a large pseudorapidity gap. During long shutdown 2 AD will be updated and integrated as a part of the FIT detector.

Built atop of the ALICE magnet there is the ALICE Cosmic Ray Detector (ACORDE) [247], which is an array of 60 large scintillators. ACORDE is used as a trigger for cosmic rays for calibration and alignment.

### 2.3.6 Muon spectrometer

In heavy-ion physics muons are mainly used to measure the production of the heavy quark resonances such as  $J/\psi$ ,  $\Psi'$  and  $\Upsilon$ . In ALICE the muon spectrometer

is located outside the main magnet [248] in the forward direction on the C side. The muon spectrometer has three sections. The first section is the absorber which removes hadronic background before it can reach the remaining sections. After the absorber the muon tracker consists of ten high granularity plates of thin cathode strip tracking stations. After the muon tracker there is a layer of iron meant to filter out any remaining particles, other than muons. The muon trigger is located behind this layer. The trigger consists of four resistive plate chambers.

### 2.3.7 Triggers

High energy physics experiments need triggers to select interesting physics. Experiments such as CMS and ATLAS at CERN look for extremely rare events. To produce these rare events LHC provides up to 40 million events each second. Such amounts can't be recorded real-time as many detectors require some time for the readout, up to 1 ms/event in ALICE. Thus one uses triggers, i.e. a set of very fast hardware based decisions on which events are to be saved. Additionally one needs some confirmation that an event has even occurred to tell other detectors that the event needs to be recorded.

For ALICE the target event rates are 1 MHz for pp collisions, 0.1-2 kHz for Pb–Pb collisions and 200 kHz for the 2013 p–Pb collisions.

At ALICE the main system responsible for the trigger decisions is the ALICE Central Trigger Processor (CTP) [249]. The CTP generates three levels of hierarchical hardware triggers - Level 0, Level 1 and Level 2, (L0, L1 and L2 respectively) before an event is accepted and transmitted to the Data Acquisition system (DAQ). Afterwards additional software assessments are performed by the High Level Trigger (HLT).

Triggers can be roughly put into two classes, minimum bias triggers that make sure no empty events are recorded, and rare triggers that require specific signatures in ALICE detectors, such as large energy deposits in EMCal or two muons in the muon arm acceptance.

#### Minimum bias trigger

Several of the ALICE detectors are used to make the initial minimum bias trigger decisions. These include the SPD layers of ITS, V0 and T0. SPD can count the number of hits in the first two layers of ITS. Minimum bias pp collisions typically require at least one hit in either SPD or V0A/V0C. Similarly Pb–Pb triggers look at both V0 and SPD hits. The p–Pb data has been mainly triggered using V0 information.

## EMCal trigger

In addition to the minimum bias triggers, the most relevant trigger for this thesis is the EMCal trigger. Parts of the EMCal trigger has been developed at the University of Jyväskylä. Extensive details of the trigger and the development work can be found in the thesis of Jiří Král [250]. Personally I have contributed to the maintenance of the level 0 trigger.

ALICE EMCal provides two levels of trigger signal, L0 and L1, which allows triggering on either single shower deposits or integrated energy deposits in larger areas, i.e. jets [251]. As inputs the trigger gets exclusive sets of  $2 \times 2$  EMCal towers, to limit the number of channels that need to be processed. The L0 trigger then checks for energy deposits within a rolling window of  $2 \times 2$  trigger channels ( $4 \times 4$  towers). Areas of  $4 \times 4$  towers most probably will contain only a single shower or two adjacent showers coming from a single decayed  $\pi^0$ . Thus the trigger is called the single shower trigger.

For L0 the trigger decision is done in Trigger Region Units (TRU) that each cover  $4 \times 42$  channels ( $8 \times 48$  towers). The amplitude from the sliding window is compared to a constant threshold. Additionally a peak finding algorithm is implemented to define correctly the time of the signal maximum. A single bit OR decision of all individual TRUs is forwarded to the CTP as the EMCal L0 trigger decision.

The L0 information is additionally forwarded to the L1 trigger, which recomputes similar  $2 \times 2$  channel decisions to produce the single shower trigger, but L1 can perform the calculation also on the borders between trigger units. In addition the L1 trigger can check for energy deposits inside a larger  $16 \times 16$  channel ( $32 \times 32$  towers) window, which is considered to be the jet trigger.

The L1 trigger can compare up to two thresholds for each single shower and jet trigger. There is a dedicated link in between the V0 detector and EMCal Summary Trigger Unit (STU), which can provide centrality information that is used to compute a dynamical threshold as a function of the V0 multiplicity [251].

The trigger subsystem provides both the L0 and L1 decisions to the CTP and DAQ.

## 2.4 TPC upgrade

### 2.4.1 ALICE upgrade during LS2

During LS2 in 2019-2020 ALICE will go through significant modifications. The goal is to be able have continuous readout [252] in heavy-ion collisions at an interaction rate of 50 kHz. ALICE will add a new Fast Interaction trigger (FIT) [253] to provide trigger and timing replacing the V0 and T0 detectors. Also the current

FMD and AD detectors will be dismantled and their roles will be taken over by FIT.

Additionally the current inner tracking system (ITS) will be completely replaced. The current layered structure with three different technologies will be replaced by a detector that uses pixel technology in all layers and with significantly reduced pixel size. Additionally the first layer will be brought closer to the beam pipe. The new ITS will have better tracking efficiency and better impact parameter resolution [230].

The muon detection will be complemented by the Muon Forward Tracker (MFT) [254]. Based on the same technology as the new ITS, MFT will be placed before the hadron absorber that sits in front of the existing muon spectrometer. MFT should significantly increase the signal/background ratio in heavy quark measurements [254].

#### 2.4.2 TPC upgrade

Many subdetectors will make small improvements to enhance the readout rate. The central trigger processor will be replaced and ALICE will introduce a new framework  $O^2$  that combines both online data acquisition and offline analysis.

The detector restricting the readout the most at the moment is the TPC. The current wire chamber based system limits the readout rate to 3.5 kHz. To achieve the 50 kHz readout rate goal the wire chambers will be replaced by a Gas Electron Multiplier (GEM) based system. The GEMs are designed to minimise ion backflow to allow continuous, ungated and untriggered readout. I have made a personal contribution to the quality assurance of the new GEM readout of TPC.

TPC has a total of 36 inner and 36 outer readout chambers. Each of these will consist of 4 layers of GEM foils. The inner chambers will only have one foil for each layer. The outer chambers are separated into three sections, each with its own layer of foils. Each GEM foil is made up of a 50  $\mu\text{m}$  thick resistive kapton layer, coated on both sides by 5 $\mu\text{m}$  thick layers of copper. Each foils is separated into a number (20-24 depending on the size of the foil) of distinct active areas. The active areas are pierced densely with holes. They have 50-100 holes in the area of a single  $\text{mm}^2$ . The density of holes changes from layer to layer. The two middle layers of foils have a larger (double) pitch (smaller hole density) while the top and bottom layers have a smaller (normal) pitch (larger hole density).

The purpose of the multilayered structure is to reduce the ion backflow [255, 256]; not only one layer of GEM foils will be installed, but a 4 layer stack. In the stack there are 2 standard pitch GEM foils, where the pitch size, i.e. the separation of the holes inside a foil is around 140  $\mu\text{m}$ , and 2 large pitch GEM foils, where the hole spacing is two times larger, 280  $\mu\text{m}$ . The two outer layers will have standard pitch and the two middle layers have large pitch. The middle layers with large

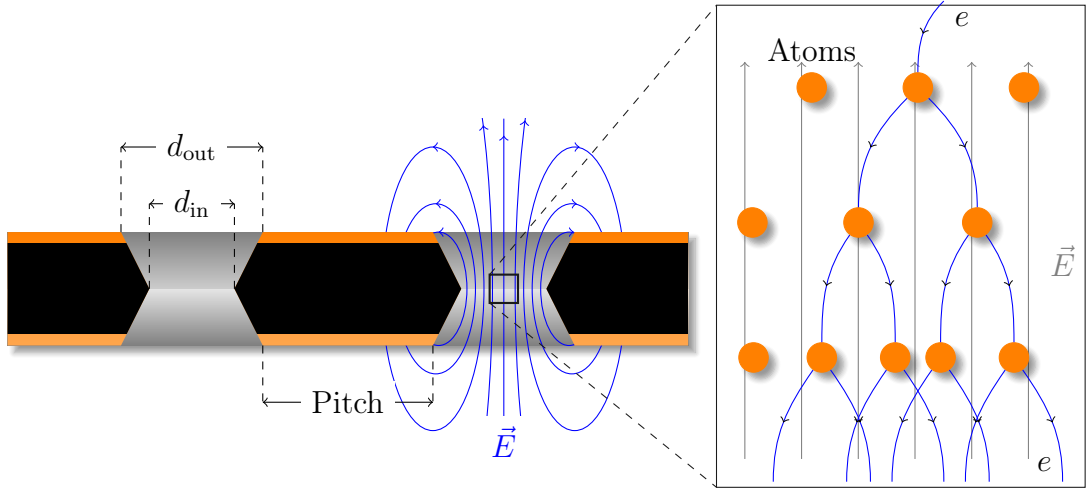


Figure 2.7: *left* Cross-section of a GEM foil. (Not to scale). The hole diameters are  $d_{\text{in}} = 50 \pm 5 \mu\text{m}$  and  $d_{\text{out}} = 70 \pm 5 \mu\text{m}$  and pitch is either 140 or 280  $\mu\text{m}$ . *right* The amplification of a GEM foil is based on the Townsend avalanche phenomenon [258]. Electrons entering the electric field inside the hole are accelerated. If they gain enough energy before colliding with atoms they can liberate additional electrons, which are further accelerated leading to a chain reaction.

pitch serve as extra insulator against the ion backflow. Additionally the setup allows operating individual GEM foils at lower voltages and still have an increase in the gain of a few orders of magnitude [257].

The holes have a conical shape which they acquire during a two step chemical etching process. The designed inner and outer diameters of the holes are  $50 \pm 5 \mu\text{m}$  and  $70 \pm 5 \mu\text{m}$  respectively. Figure 2.7 shows the cross-section of a hole alongside with the operation principle of a GEM foil.

The working principle of these foils is based on the Townsend avalanche phenomenon [258], which is also used in proportional counters such as Geiger counters. There is a large potential difference (140–400 V) applied to the two sides of the foil, which results in large field in each hole. Electrons gain energy in the field and if the electric field is strong enough, the free electron can gain sufficient velocity (energy) to liberate another electron when it next collides with a molecule. The two free electrons then travel along the electric field and can gain sufficient energy from the electric field to cause further impact ionisations, and so on, leading to a chain reaction. Under the right conditions a single electron entering any hole will create an avalanche containing 100–1000 electrons; this is the gain of the GEM foil.

As opposed to wire chambers, which typically have one voltage setting, a GEM-based detector requires several independent voltage settings: there is a drift voltage

which drives the electrons from the ionisation point to the GEM, an amplification voltage, and an extraction voltage that brings electrons from the GEM exit to the readout plane. In a multilayer system this is further complicated. The voltages between layers of foils can be tuned individually optimising amplification and preventing ion backflow.

## Quality Assurance of the GEM foils

The GEM foils are produced at CERN, where they will undergo a basic QA (QA-B) procedure, that includes a coarse optical inspection for any large defects ( $\gtrsim 1$  mm) and a short term high voltage measurement. Afterwards the foils are sent for an advanced quality assurance (QA-A) procedure which is performed in one of the two QA-A centres, one in the Helsinki Institute of Physics (HIP) and one in the Wigner Research Centre in Budapest. Details of the QA-A procedure can be found in the thesis of Márton Vargyas [259] and in [260]. In the QA-A centres all foils are put through a detailed optical scanning process and a long term high voltage measurement. I was personally performing the QA production in Helsinki for the final 6 months of the project.

The optical scan is performed with the help of a scanning robot. The setup along with most of the software was developed at the Detector Laboratory of the Helsinki Institute of Physics [261]. The optical scan is able to distinguish every single hole on the GEM foil and measure their properties. The purpose of the scan is two-fold; to catch defects that could affect the performance and classify the foils based on their hole parameters. It is expected that these are connected with the foil's electric properties [261]. For example, smaller holes create more intense and focused fields, which would result in larger amplification of their avalanche electrons, i.e. the local gain is expected to be larger.

After the optical scanning, the foils are subjected to a long term (5-12 hours) high voltage leakage current measurement. Each segment of the GEM foil is connected to a high voltage of 500 V and the leakage current is measured separately for each segment. The accepted leakage current in each segment is 0.16 nA. Foils that fail the criteria are sent to CERN for recleaning or repairing, after which they will go through the QA pipeline again.

Additionally some foils will be put through a gain mapping procedure. This process is time consuming and can only be performed in the QA-A centre in Budapest. Thus it was done for only a small subset of foils. However, by measuring the gain in some foils the gain can be correlated with foil properties. Thus the single foil gain can be predicted based on the results of the optical scan. Details can be found in [259].

# Chapter 3

## Event and track selection

The  $\sqrt{s_{\text{NN}}} = 5.02$  TeV p–Pb ( $1.3 \cdot 10^8$  events,  $\mathcal{L}_{\text{int}} = 62 \text{ nb}^{-1}$ ) collisions were recorded in 2013 by the ALICE detector [216]. The details of the performance of the ALICE detector during LHC Run 1 (2009–2013) are presented in [262].

### 3.1 Event selection

This analysis uses both a minimum bias trigger and an EMCal based trigger to select the analysed events. For the 2013 p–Pb collisions minimum bias events are required to have signals in both sides of V0, V0A (positive  $\eta$ , lead going side in p–Pb collisions) and V0C (negative  $\eta$ ). The timing difference between the two stations is also used to reduce the contamination of the data sample from beam-gas events [262].

EMCal is used to provide the jet trigger used in triggered datasets. EMCal can be used to trigger on single shower deposits or energy deposits integrated over a larger area. Latter case is used for jet triggers. The EMCal trigger definition in the 2013 p–Pb collisions requires an energy deposit of either 10 GeV for the low threshold trigger or 20 GeV for the high threshold trigger in a  $32 \times 32$  patch size. Triggers, V0 and EMCal are discussed in more detail in sections 2.3.5, 2.3.7 and 2.3.4.

### 3.2 Track reconstruction

The analysis uses charged tracks that are reconstructed with the Time Projection Chamber (TPC) [231] and the Inner Tracking System (ITS) [263]. These are discussed in sections 2.3.1 and 2.3.2. A detailed overview of track reconstruction in ALICE can be found from [262].

The track reconstruction procedure is shown in Figure 3.1. The figure shows only one track, but in reality the reconstruction has to deal with many tracks. The ALICE track reconstruction procedure starts in TPC. The TPC readout chambers include 159 tangential pad rows. The procedure starts from the outermost layer and based on proximity the hits in this layer are paired with hits in the next layer inwards. When this procedure reaches the innermost pad row in TPC, the algorithm proceeds to ITS using the information obtained from TPC as an initial seed. Similar procedure of pairing adjacent layers with a proximity cut is repeated in ITS.

When the reconstruction of tracks in ITS is completed, all reconstructed tracks are extrapolated to their point of closest approach to the interaction vertex obtained from SPD information. Then the track fitting is repeated but starting from the innermost layer and proceeding outwards. A Kalman filter [264] technique is used to perform the new fits using the hits found in the previous stage. In this iteration the reconstructed tracks are matched also to other detectors in the central barrel beyond TPC. When this step is complete, a third and final refit step is performed, again proceeding from the outermost TPC pad rows inwards to the interaction point. This final refit provides the final track parameters.

Using the reconstructed tracks the estimation of the primary vertex can be improved from the original SPD information. The reconstructed tracks are extrapolated to the beam line and the primary vertex position is determined by a weighted average of the points of closest approach.

The remaining step of the track reconstruction is the determination of secondary vertices. In this step the procedure selects all reconstructed tracks with distances of closest approach (DCA) to the primary vertex larger than a defined minimum value. The algorithm determines points of closest approach for pairs of these tracks. If the tracks are close enough to each other and show properties of short lived particle decays, these points are identified as secondary vertices.

Combining the information from the ITS and the TPC provides a resolution ranging from 1 to 10 % for charged particles with momenta from 0.15 to 100 GeV/c. For tracks without the ITS information, the momentum resolution is comparable to that of ITS+TPC tracks below transverse momentum  $p_T = 10$  GeV/c, but for higher momenta the resolution reaches 20 % at  $p_T = 50$  GeV/c [262, 266].

## Track selection

In p–Pb collisions the tracks are selected following the hybrid approach [267] which ensures a uniform distribution of tracks as a function of azimuthal angle ( $\varphi$ ). The parameters in the approach are summarised in Table 3.1.

The first requirements are on the quality of the track fit in ITS and TPC. The ITS requirement only removes tracks that are clear outliers. For TPC the

Table 3.1: Parameters in the hybrid track cut

Track Cut	Step 1	Step 2
$\chi^2 / \text{ITS cluster}$	< 36	< 36
$\chi^2 / \text{ITS cluster}$	< 4	< 4
Hits in ITS	3	0
ITS hit requirements	1 in SPD	No requirement
Vertex constraint	No	Yes
Number of crossed rows in TPC	70	70
TPC crossed rows over findable clusters	> 0.8	> 0.8
Fraction of shared TPC clusters	< 0.4	< 0.4
Kink daughters	Rejected	Rejected
$\text{DCA}_{xy}$	< 3.2 cm	< 3.2 cm
$\text{DCA}_z$	< 2.4 cm	< 2.4 cm
Other		Rejected by step 1

requirement is much more strict. For step 1 it is required that a track has 3 out of the 6 possible hits in ITS, one of which must be in the SPD. In step 2 this is replaced by a vertex constraint, which includes the primary vertex itself as a point to the track to improve the momentum resolution.

The approach requires that 70 out of the 159 possible pad rows in the TPC are crossed. This is a measure of the effective track length inside the TPC. This takes into account the possibility that a track can have missing pad rows if the charge in these clusters is below the detection threshold. Additionally the track selection criteria require that the ratio between crossed rows and geometrically possible clusters clusters is at least 0.8. This takes into account dead zones due to chamber boundaries and limited  $\eta$ -acceptance. For both steps the hybrid requires that the fraction of clusters shared with several tracks is less than 40%.

Additional cuts are meant to ensure that the reconstructed tracks are actually produced in the primary collision. A particle might scatter in the detector altering its track. The particle after such a scatter is rejected in the cuts, as it no longer carries information about the primary collisions. The remaining cuts are on the DCA to primary vertex. To have confidence that the track comes from the primary collision, the track must be close enough to the primary vertex. The cuts are different for the distance along the beam axis ( $\text{DCA}_z$ ) and perpendicular to ( $\text{DCA}_{xy}$ ) the beam axis.

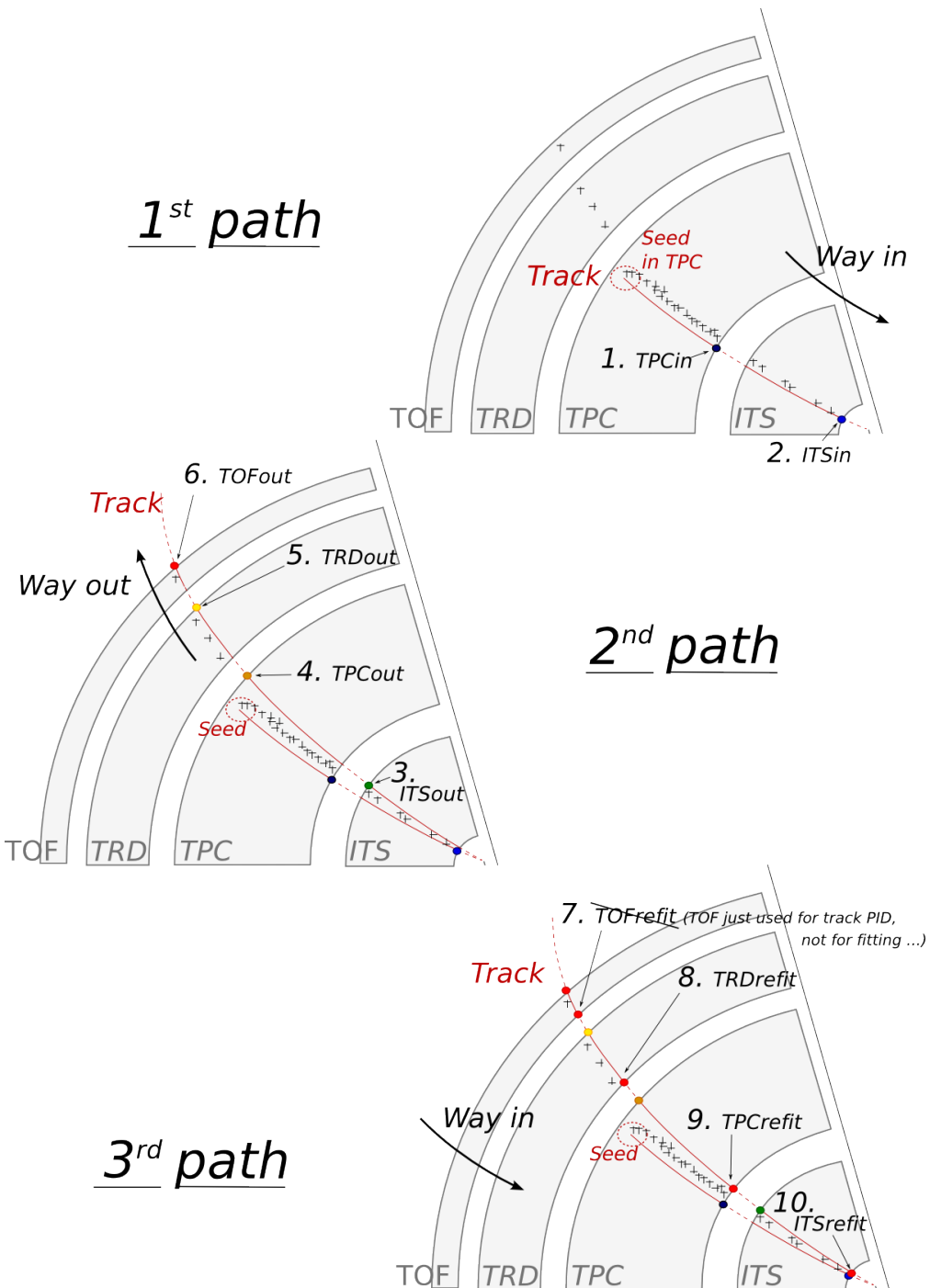


Figure 3.1: Principles of tracking in the ALICE experiment, showing the three successive paths allowing to build a track and refine its parameters. Numbers ranging from 1 to 10 mention the bits that are activated in case of success during the propagation of the Kalman filter at the considered stage. Figure from [265].

### 3.3 Cluster selection

Neutral particles used in jet reconstruction are reconstructed by the Electromagnetic Calorimeter (EMCal) [240]. The EMCal covers an area with a range of  $|\eta| < 0.7$  in pseudorapidity and 100 deg in azimuth. EMCal is complemented by the Dijet Calorimeter (DCal) [241] and Photon Spectrometer (PHOS) [239] that are situated opposite of the EMCal in azimuth. PHOS covers 70 degrees in azimuth and  $|\eta| < 0.12$ . The DCal is technologically identical to EMCal, but is located opposite to the EMCal. The DCal coverage spans 67 degrees in azimuth, but in pseudorapidity the mid region is occupied by the PHOS. Between the active volumes of PHOS and DCal, there is a gap of 10 cm.

The clusters used in the analysis were obtained from the EMCal clusteriser. The parameters used in the clusteriser are summarised in Table 3.2. The clusteriser searches for a tower with energy deposit greater than a defined seed energy and merges all towers that share a side if their energy deposit is higher than a defined threshold. In the next step all towers sharing a side with already included towers are added, again requiring that the energy deposits exceeds the threshold. The algorithm can identify local minima and halts the clustering in case that the neighbouring tower energy is higher. Already clustered towers are removed from the pool, so any individual tower can be clustered only once.

Highly energetic calorimeter hits should spread into several towers as the electromagnetic shower evolves. However, some clusters with high energy have their energy located in a single tower. These are believed to come from a slow neutron hitting the APD readout of the towers. They are referred to as exotic clusters. The measure of exoticity is denoted as

$$1 - \frac{E_{\text{cross}}}{E_{\text{max}}}, \quad (3.1)$$

where  $E_{\text{max}}$  is the energy in the most energetic tower and  $E_{\text{cross}}$  is the sum of the four towers neighbouring the most energetic one. The closer this is to 1, the more

Table 3.2: Parameters used in the EMCal clusteriser

Setting	Value
Clusteriser seed	0.2 MeV
Clusteriser cutoff	0.05 MeV
Cells in cluster	> 1
Track matching radius	0.025
Fiducial cut	1 tower
Exotic cut	0.97
Minimal cluster Energy	0.3 GeV

exotic the cluster is and the larger the probability that it is fake. Cut of 0.97 has been adopted as default for analyses using EMCal, including the one presented in this thesis. Any clusters above this cut are removed.

To suppress charged hadron contributions in EMCal, tracks identified by tracking detectors are extrapolated to the EMCal surface. The clusteriser looks for the closest cluster in EMCal and the track is further extrapolated until it reaches the same depth as the cluster. The remaining distance from the extrapolated track to the cluster is then checked to reject hadronic hits. Clusters matched to charged tracks are removed from the analysis as well as clusters being identified as fake.

# Chapter 4

## Analysis method

### 4.1 Jet Finding

The analysis uses reconstructed jets as estimates of the original parton. Jet reconstruction essentially combines nearby tracks into jets.

Collisions between hadrons are never as clean as electron-positron collisions. Even for a proton-proton collision there are participant partons, that will produce a soft background in addition to the hard scattering products. Jet reconstruction must deal with this soft background. The reconstruction is never perfect, one can have uncorrelated tracks that get included in the jet and some tracks originating from the parton are missed by the reconstruction. There are several methods to perform the reconstruction, all of which require some kind of size parameter, which cuts out jet participants too far from the jet axis. The tracks that are grouped into a jet are referred to as jet constituents.

In each collision event, the jets are reconstructed using FastJet [268] with the anti- $k_T$  algorithm [269]. Jets for  $R=0.4$  are selected in  $|\eta| < 0.25$  to satisfy the fiducial acceptance of the EMCAL. In jet reconstruction both charged tracks with  $p_T > 0.15 \text{ GeV}/c$  and neutral clusters with  $p_T > 0.30 \text{ GeV}/c$  are considered. Clusters that match charged tracks are removed before jet reconstruction. The analysis is then performed by analysing the charged jet constituents and results are presented in terms of the jet transverse momentum  $p_{T,\text{jet}}$ .

#### 4.1.1 Anti $k_T$ algorithm

Jets are reconstructed using the anti- $k_T$  algorithm [269]. The algorithm works by trying to undo the splittings through combining protojets. First the algorithm creates a list of protojets. At the beginning the list is populated by converting each track in the event into a protojet. Then the algorithm proceeds by combining

these protojets. A simplified picture of the process for a limited number of tracks is shown in Figure 4.1

The algorithm calculates distance measures,  $k_{T,i}$  and  $k_{T,i,j}$  for each individual protojet and for each possible pair of protojets. For individual protojets this depends on the transverse momentum of the track.

$$k_{T,i}^2 = p_{T,i}^{2p} \quad (4.1)$$

For each pair of protojets the distance measure is calculated as

$$k_{T,i,j}^2 = \min(p_{T,i}^{2p}, p_{T,j}^{2p}) \frac{\Delta R_{i,j}^2}{D^2}, \quad (4.2)$$

where the distance is taken over azimuthal angle,  $\phi$  and rapidity  $y$ ,

$$\Delta R_{i,j} = (\phi_i - \phi_j)^2 + (y_i - y_j)^2. \quad (4.3)$$

If  $k_{T,i}$  is the smallest quantity in the event then the protojet is promoted to a jet and it is removed from further consideration. If  $k_{T,i,j}$  is the smallest quantity the two protojets  $i$  and  $j$  are merged into a new protojet. This is repeated until no protojets are left.

The choice of the power  $p$  in the distance measure depends on the algorithm used

- $p = 1$ :  $k_T$  algorithm
- $p = 0$ : Cambridge Aachen algorithm
- $p = -1$ : anti- $k_T$  algorithm

With the choice  $p = -1$  in anti- $k_T$  algorithm, the softest splittings are undone first. One consequence of the power choice in the anti- $k_T$  algorithm is that reconstructed jets have a shape close to circular.

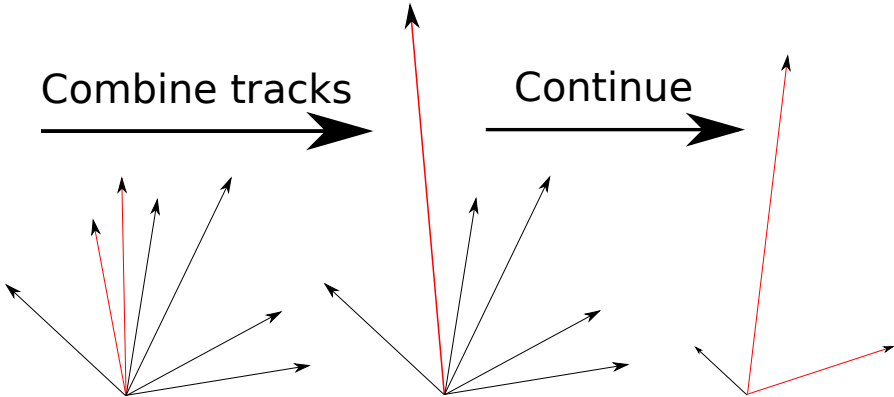


Figure 4.1: A simple example of the anti- $k_T$  algorithm in progress. The red tracks in the leftmost figure are identified to have the smallest  $k_{T,i}$  in the event and are combined into the red track of the middle figure. As this continues the remaining tracks are added to this or other jets. One track was deemed to be isolated enough to be counted as a protojet by itself. Note that the rightmost figure is zoomed out.

## 4.2 Definition of $j_T$

The reconstructed jet axis is used for  $j_T$  reference. Any charged track within a fixed cone with radius  $R$  is taken as a jet constituent, as opposed to using the constituent list provided by the jet algorithm. Anti- $k_T$  produces jets that are very circular in shape. Thus this doesn't change the constituent list considerably. Calorimeter clusters are used only in jet reconstruction.

The jet fragmentation transverse momentum,  $\vec{j}_T$ , is defined as the component of the constituent track momentum,  $\vec{p}_{\text{track}}$ , transverse to the jet momentum,  $\vec{p}_{\text{jet}}$ . It represents the transverse kick with respect to the initial hard parton momentum that a fragmenting particle receives during the fragmentation process, which is a measure of the momentum spread of the jet fragments.

The resulting  $\vec{j}_T$  is illustrated in Fig. 4.2. The length of the  $\vec{j}_T$  vector depends on the jet and track momentum vectors  $\vec{p}_{\text{jet}}$  and  $\vec{p}_{\text{track}}$

$$j_T = \frac{|\vec{p}_{\text{jet}} \times \vec{p}_{\text{track}}|}{|\vec{p}_{\text{jet}}|}. \quad (4.4)$$

Resulting  $j_T$  distributions are shown as

$$\frac{1}{j_T} \frac{dN}{dj_T} \quad (4.5)$$

distributions. The logic behind this is that  $j_T$  is inherently a two-dimensional

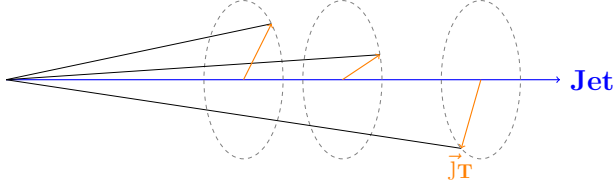


Figure 4.2: Illustration of  $\vec{j}_T$ . The jet fragmentation transverse momentum,  $\vec{j}_T$ , is defined as the momentum component of the track momentum,  $\vec{p}_{\text{track}}$ , that is transverse to the jet momentum,  $\vec{p}_{\text{jet}}$ .

observable, comprised of  $j_{Tx}$  and  $j_{Ty}$  components. So the actual physical observable would be

$$\frac{d^2N}{dj_{Tx} dj_{Ty}} \quad (4.6)$$

Changing into polar coordinates with  $j_{Tr} = j_T$  and  $\theta$  gives

$$\frac{d^2N}{j_T dj_T d\theta}, \quad (4.7)$$

where  $j_T$  over the azimuth  $\theta$  should stay constant and it can be integrated over, which gives

$$\frac{1}{2\pi} \frac{dN}{j_T dj_T}. \quad (4.8)$$

Results of the raw inclusive  $j_T$  distribution in four  $p_{T,\text{jet}}$  bins with background are shown in Figure 4.3. Background, i.e. the contribution from the underlying event, is further discussed in Section 4.4

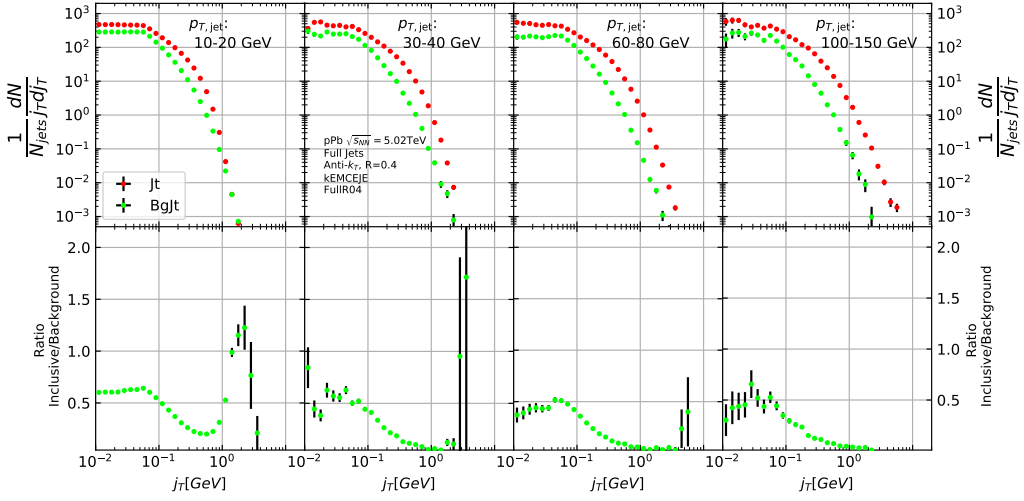


Figure 4.3: Inclusive  $j_T$  with background

### 4.3 Unfolding detector effects

The raw inclusive  $j_T$  distributions are corrected for the detector inefficiency with an unfolding procedure. The procedure uses response matrices obtained from a PYTHIA [270] simulation.

Measured distributions are affected by two main factors; Limited acceptance - The probability to observe a given event is less than one and limited resolution - Quantity  $x$  cannot be determined exactly, but there is a measurement error. True  $f(x)$  and measured  $g(y)$  distributions are connected by a convolution integral. Including statistical fluctuations this becomes

$$\hat{g}(y) = \int_a^b A(y, x) f(x) dx + \epsilon(y), \quad (4.9)$$

where  $A$  is the detector response obtained by (for example) Monte Carlo simulations and  $\epsilon(y)$  is the term coming from statistical fluctuations. If  $x$  and  $y$  are discrete variables we have

$$\hat{g}_i = \sum_{j=1}^m A_{ij} f_j + \epsilon_i, \quad (4.10)$$

where  $i$  and  $j$  give the  $j_T$  bins in the true and measured distributions.  $f_j$  and  $g_i$  give the counts in these bins. Or in matrix form

$$\hat{g} = Af + \epsilon, \quad (4.11)$$

where  $\hat{g}$  and  $f$  are vectors corresponding to the measured and true histograms. If the only detector effect is limited acceptance,  $A$  is a diagonal matrix, i.e.  $A_{ij} =$

0 for  $i \neq j$ . We want to deduce the true distribution  $f$ , when the measured distribution  $g$  is known. In a general discrete case the (naive) solution is obtained by the inverse matrix

$$\hat{f} = A^{-1}\hat{g} \quad (4.12)$$

However this usually leads to oscillating solutions and determining the inverse matrix can be difficult.

Two common methods to perform this inversion are Bayesian and SVD unfolding methods. Often the solution requires some additional *a priori* information. For example the solution should be smooth in most cases.

### 4.3.1 Bayesian unfolding

The bayesian (iterative) method is based on the Bayes formula [271].

$$P(C_i|E_j) = \frac{P(E_j|C_i) P_0(C_i)}{\sum_{l=1}^{n_C} P(E_j|C_l) P_0(C_l)}, \quad (4.13)$$

i.e. the probability of Cause  $C_i$  ("truth") given Effect  $E_j$  ("observed"),  $P(C_i|E_j)$ , is proportional to the probability of observing  $E_j$  given  $C_i$ ,  $P(E_j|C_i)$  (response matrix) and the true distribution  $P_0(C_i)$ . In the equation  $l$  is a summation variable over the number of causes  $n_C$ .

In the unfolding procedure  $P_0$  is given some starting distribution, either a uniform distribution or some guess of the final distribution. Taking into account the inefficiency this gives

$$\hat{n}(C_i) = \frac{1}{\epsilon_i} \sum_{j=1}^{n_E} n(E_j) P(C_i|E_j), \quad (4.14)$$

where  $\epsilon_i$  is the efficiency (between 0 and 1) of getting any signal from Cause  $C_i$ ,  $P(C_i|E_j)$  is the conditional probability from Equation 4.14 and  $n(E_j)$  are the observed frequencies. First  $P(C_i|E_j)$  is calculated with the uniform distribution or best guess of the shape of the distribution. This is then used to calculate the new distribution  $\hat{P}(C_i)$

$$\hat{N}_{true} = \sum_{i=1}^{n_C} \hat{n}(C_i), \quad \hat{P}(C_i) = P(C_i|n(E)) = \frac{\hat{n}(C_i)}{\hat{N}_{true}} \quad (4.15)$$

$P_0$  is then replaced with  $\hat{P}$  and the procedure is repeated until an acceptable solution is found. One way to gauge the acceptability is measuring the change between iterations. Initially there is a large change between iterations, but it should get small when close to the final distribution. The number of iterations

should be as low as possible, as the errors increase when going further in the iterations, but the number of iterations must be high enough so that the correct distribution is extracted.

The bayesian procedure alongside with the SVD unfolding method are implemented in the RooUnfold package [272], which is used to perform the unfolding in practice. SVD unfolding is another procedure that utilises the Singular Value Decomposition (SVD) of the response matrix to find the inverse of the response matrix [273].

## Error propagation in the Bayesian procedure

The measured distribution has some statistical uncertainty, this should be reflected in the unfolded distribution. Additionally the response matrix may have some uncertainty if the statistics used in the Monte Carlo simulation were limited.

For errors originating from the measured distribution RooUnfold uses the error propagation matrix

$$\frac{\partial \hat{n}(C_i)}{\partial n(E_j)} = M_{ij} + \frac{\hat{n}(C_i)}{n_0(C_i)} \frac{\partial n_0(C_i)}{\partial n(E_j)} - \sum_{k=1}^{n_E} \sum_{l=1}^{n_C} \frac{n(E_k) \epsilon_l}{n_0(C_l)} M_{ik} M_{lk} \frac{\partial n_0(C_l)}{\partial n(E_j)}, \quad (4.16)$$

where  $\hat{n}(C_i)$  is the unfolded result from Eq. 4.15. This depends upon the matrix  $\frac{\partial n_0(C_i)}{\partial n(E_j)}$ , which is  $\frac{\partial \hat{n}(C_i)}{\partial n(E_j)}$  from the previous iteration. In the first iteration,  $\frac{\partial n_0(C_i)}{\partial n(E_j)} = 0$  and  $\frac{\partial \hat{n}(C_i)}{\partial n(E_j)} = M_{ij}$ .

The error propagation matrix  $V$  is used to obtain the covariance matrix on the unfolded distribution

$$V(\hat{n}(C_k), \hat{n}(C_l)) = \sum_{i,j=1}^{n_E} \frac{\partial \hat{n}(C_k)}{\partial n(E_i)} V(\hat{n}(E_i), \hat{n}(E_j)) \frac{\partial \hat{n}(C_l)}{\partial n(E_j)}, \quad (4.17)$$

where  $V(\hat{n}(E_i), \hat{n}(E_j))$  is the covariance matrix of the measurements. In counting experiments common in particle physics, each bin is independently Poisson distributed, with

$$V(\hat{n}(E_i), \hat{n}(E_j)) = n(E_i) \delta_{ij} \quad (4.18)$$

The error propagation matrix for the response matrix is

$$\begin{aligned} \frac{\partial \hat{n}(C_i)}{\partial P(E_j|C_k)} &= \frac{1}{\epsilon_i} \left( \frac{n_0(C_i) n(E_j)}{f_j} - \hat{n}(C_i) \right) \delta_{ik} - \frac{n_0(C_k) n(E_j)}{f_j} M_{ij} + \\ &\quad \frac{\hat{n}(C_i)}{n_0(C_i)} \frac{\partial n_0(C_i)}{\partial P(E_j|C_k)} - \frac{\epsilon_i}{n_0(C_i)} \sum_{l=1}^{n_E} \sum_{r=1}^{n_C} n(E_l) M_{il} M_{rl} \frac{\partial n_0(C_r)}{\partial P(E_j|C_k)}, \end{aligned} \quad (4.19)$$

where  $\frac{\partial n_0(C_i)}{\partial P(E_j|C_k)}$  is the error propagation matrix from the previous iteration,  $\frac{\hat{n}(C_i)}{\partial P(E_j|C_k)}$ . For the first iteration, this is zero and the final two terms in Eq. 4.19 disappear.

The covariance matrix due to these errors is given by

$$V(\hat{n}(C_k), \hat{n}(C_l)) = \sum_{j,s=1}^{n_E} \sum_{i,r=1}^{n_C} \frac{\partial \hat{n}(C_k)}{\partial P(E_j|C_i)} V(P(E_j|C_i), P(E_s|C_r)) \frac{\partial \hat{n}(C_l)}{\partial P(E_s|C_r)}, \quad (4.20)$$

where  $V(P(E_j|C_i), P(E_s|C_r))$  can be taken as multinomial, Poisson or other distribution.

### 4.3.2 Pseudo-experiment Monte Carlo

A Monte Carlo pseudo-experiment simulation was performed to see the performance of unfolding in an ideal case. The simulation samples jet  $p_T$  values from the observed  $p_T$  distribution. Starting from this  $p_T$  the simulation starts creating tracks with

$$p_{\text{track}} = z_{\text{track}} p_{T,\text{jet}} \quad (4.21)$$

where  $z_{\text{track}}$  is sampled from the observed  $z$  distribution. Tracks are given random  $\eta$  and  $\phi$  values from uniform distributions centred at 0. All tracks below 0.15 GeV/c are discarded. Sampling is continued until the sum of the track transverse momenta exceeds the jet transverse momentum. The sum of all the track momenta is calculated. This sum is then defined to be the jet.

Simultaneously a  $p_T$  dependant observation efficiency is applied to the tracks and a separate observed jet is calculated using only the observed tracks. Additionally a set of fake tracks is added to the observed jet. Fake tracks are generated identically to normal tracks, except for  $p_{T,\text{track}}$ , which is taken from a uniform distribution between 0.15 GeV/c and 1 GeV/c. Tracks are always either observed or not at the true momentum. No smearing is added to the observed momentum.

Afterwards the tracks are looped over for  $j_T$  calculation. For observed tracks we calculate  $j_T$  with respect to both the true jet axis and the observed jet. The

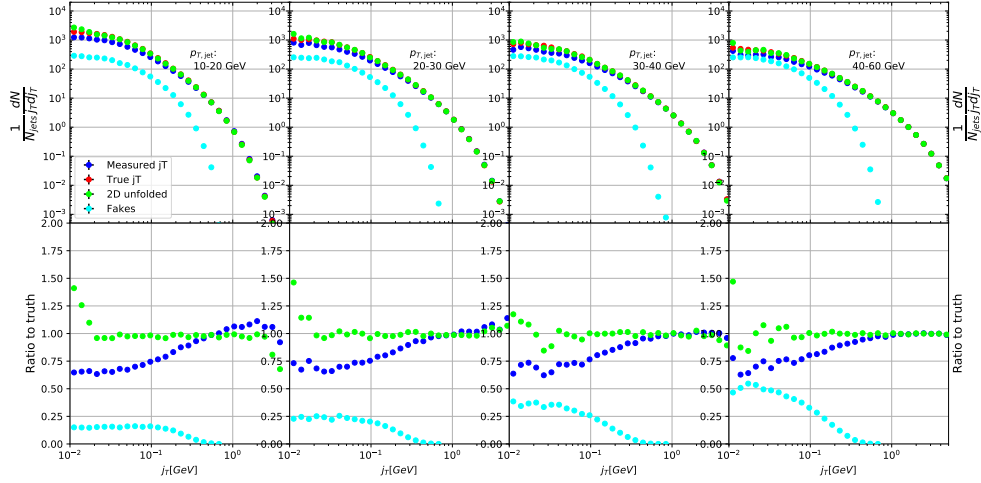


Figure 4.4: Results from unfolding in the pseudo-experiment Monte Carlo simulation

two dimensional (2D) Response matrix is filled with

$$(j_T^{\text{obs}}, p_{T,\text{jet}}^{\text{obs}}, j_T^{\text{true}}, p_{T,\text{jet}}^{\text{true}}), \quad (4.22)$$

where  $j_T^{\text{obs}}$  and  $p_{T,\text{jet}}^{\text{obs}}$  are the observed values and  $j_T^{\text{true}}$  and  $p_{T,\text{jet}}^{\text{true}}$  are the true values. In practice this is done with a set of three dimensional (3D) histograms, where  $p_{T,\text{jet},\text{true}}$  determines the histogram index and the remaining three values the bin in the 3D histogram.

After creating the response matrices, an identical procedure is carried out to the create testing data. Now instead of filling response matrices, 2D histograms are filled with  $(j_T^{\text{obs}}, p_{T,\text{jet}}^{\text{obs}})$  and  $(j_T^{\text{true}}, p_{T,\text{jet}}^{\text{true}})$

The observed distributions are unfolded using the 2D Bayesian (iterative) algorithm of RooUnfold. Results are shown in Figure 4.4. Aside from some discrepancy at very low  $j_T$  the true distribution is retrieved well.

### 4.3.3 Pythia Response matrices

A PYTHIA 6 simulation was carried out to determine the response matrices. The simulation used the Perugia 2011 [274] tune with  $\sqrt{s_{NN}}=5.02$  TeV. The detector response of the particle level tracks was simulated using GEANT3 [275, 276].

Response matrices are filled through correlation between MC detector and particle level jets and tracks. When creating the response matrices detector level tracks in each event are first analysed using the same procedure as for data, but their  $j_T$  values are stored in an array. This is only done for tracks that are closer

than the cone size,  $R$ , to a jet. Thus most tracks in the event will not have their  $j_T$  values calculated. The analysis then moves to particle level (MC) tracks. There are analysed similarly, but for each track the code checks whether a corresponding detector level track existed and if that track had a  $j_T$  value. Finally the code checks for detector level tracks that don't have corresponding particle level track with a  $j_T$  value.

There are several possibilities that have to be taken into account:

- We find a corresponding track with a  $j_T$  value. Response matrix is filled normally with  $(j_T^{\text{obs}}, p_{T,\text{jet}}^{\text{obs}}, j_T^{\text{true}}, p_{T,\text{jet}}^{\text{true}})$
- We don't find a corresponding track. Record  $(j_T^{\text{true}}, p_{T,\text{jet}}^{\text{true}})$  as a miss
- We find a corresponding track, but it didn't have  $j_T$  value. Most likely because it was not part of a jet in the detector level set. Similary record  $(j_T^{\text{true}}, p_{T,\text{jet}}^{\text{true}})$  as a miss
- For detector level tracks that have no correspondence in particle level set the code records  $(j_T^{\text{obs}}, p_{T,\text{jet}}^{\text{obs}})$  as a fake

In the analysis code the response matrix is made of an array of 3 dimensional histograms, with  $(j_T^{\text{obs}}, p_{T,\text{jet}}^{\text{obs}}, j_T^{\text{true}})$  as axes. The histogram index gives the  $p_{T,\text{jet}}^{\text{true}}$  value. The ranges in the response matrices of both  $j_T$  and  $p_{T,\text{jet}}$  match the ranges used for the end results. For  $j_T$  the range is between  $0.01 \text{ GeV}/c$  and  $20 \text{ GeV}/c$  and  $p_{T,\text{jet}}$  between  $5 \text{ GeV}/c$  and  $500 \text{ GeV}/c$ . The ranges are the same in detector and particle level.

As a primary method unfolding is performed with an iterative (bayesian) algorithm using the RooUnfold [272] package. The number of iterations used is 4. As a default the true  $j_T$  distribution from the PYTHIA simulation is used as the prior.

#### 4.3.4 Unfolding closure test

The PYTHIA set is divided into 2 halves. First is used to fill the response matrices, as well as record missed and fake tracks. Second half is used to test the effectiveness of the unfolding method. Jet  $p_T$  distributions and response matrix are shown in Figure 4.5. For the range where this analysis is performed,  $40 \text{ GeV}/c < p_{T,\text{jet}} < 150 \text{ GeV}/c$ , the  $p_{T,\text{jet}}$  distribution is recovered well. At low  $p_{T,\text{jet}}$  the true distribution can't be recovered. The primary reason is that jet with  $p_{T,\text{obs}} < 5 \text{ GeV}/c$  are not considered, although  $p_{T,\text{true}}$  would have been above  $5 \text{ GeV}/c$ . Thus these are missing from the response matrix and their contribution can't be unfolded. At high  $p_{T,\text{jet}}$  the situation is opposite. Jets with  $p_{T,\text{true}} > 500 \text{ GeV}/c$  are lost due to histogram limits. Thus jets just below this limit are overrepresented in the response matrix for  $p_{T,\text{obs}} \approx 500 \text{ GeV}/c$ .

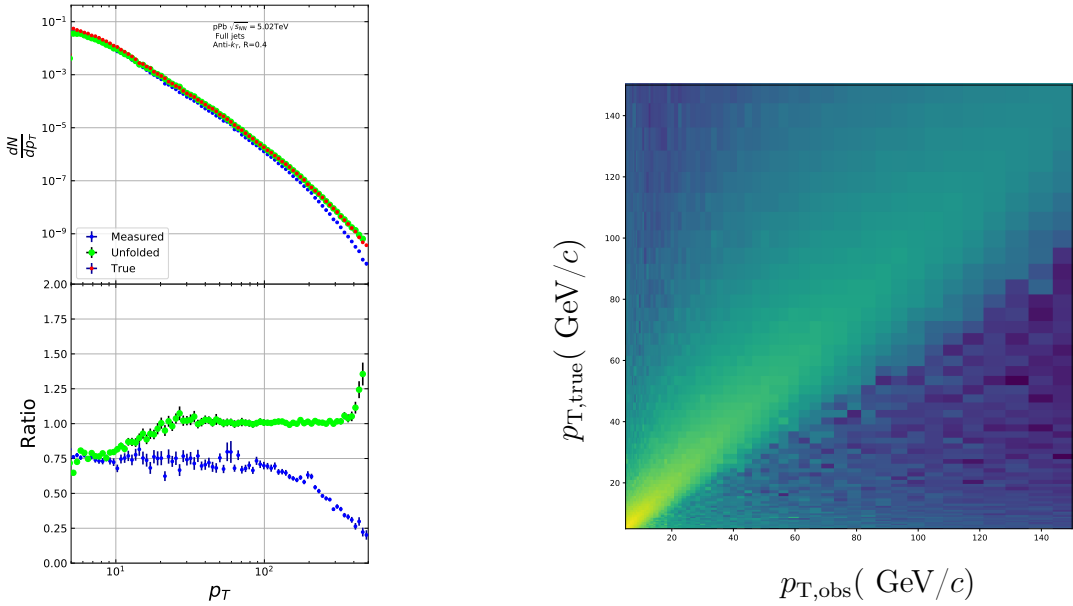


Figure 4.5: *left:* Unfolded jet  $p_T$  distribution in PYTHIA closure test *right:* Jet  $p_T$  response matrix from unfolding closure test

Response matrices within single jet  $p_T$  bins are shown in Figure 4.6. Results from the closure test are shown in Figure 4.7. In the lowest jet  $p_T$  bins unfolding fails to recover the true distribution. The lowest jet  $p_T$  bins are dominated by combinatorial jets and thus the true detector response is likely not retrieved.

Above  $30 \text{ GeV}/c < p_{T,\text{jet}} < 40 \text{ GeV}/c$  the distribution is recovered well in the mid  $j_T$  region. At  $j_T < 0.1 \text{ GeV}/c$  there is clear discrepancy and hence the final results are shown only for  $j_T > 0.1 \text{ GeV}/c$ . Additionally there is some discrepancy at very high  $j_T$ . This is taken into account in the unfolding systematics.

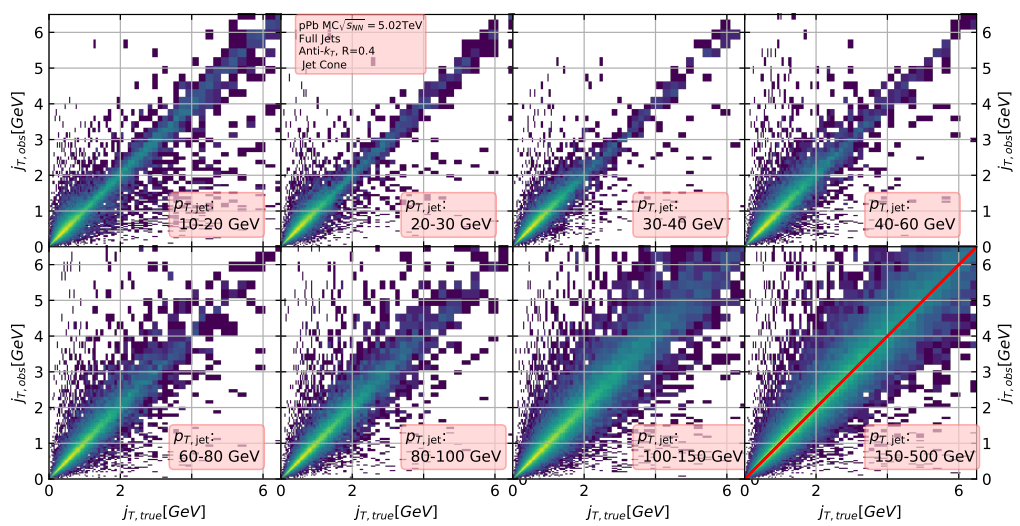


Figure 4.6:  $j_T$  Response matrices in individual  $p_{T,\text{jet}}$  bins

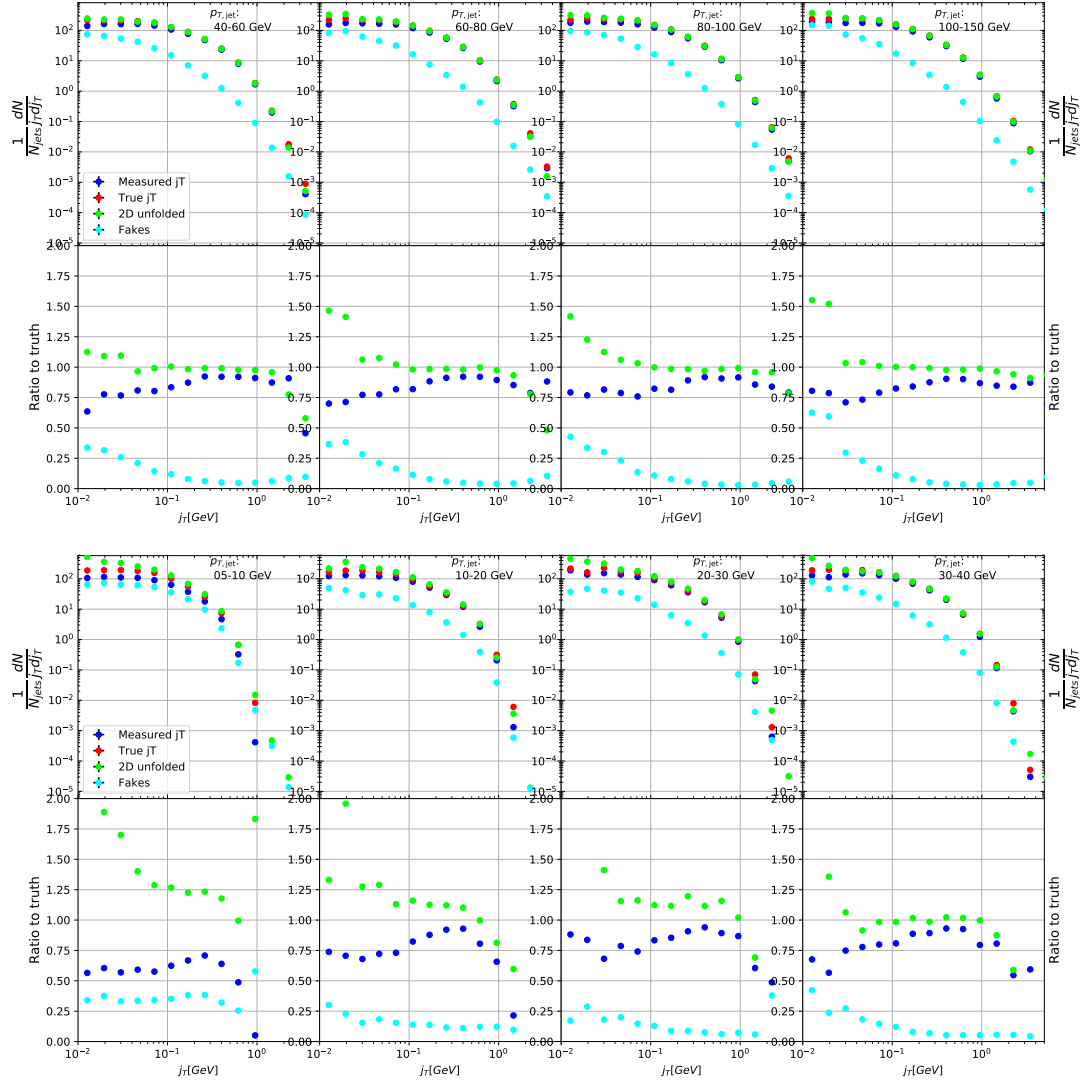


Figure 4.7: Pythia closure test results. Fake tracks include also tracks that do exist in the true dataset, but for one reason or another were not given  $j_T$  values.  $j_T$  is only calculated for tracks that are associated with jets.

## 4.4 Background

When calculating  $j_T$  distributions for jet constituents there is a contribution from the underlying event (UE), i.e. tracks that just happen to be close to the jet axis. To find the signal coming from the actual jet we need to subtract the background (UE) contribution. On a jet-by-jet basis this is difficult to achieve reliably, so one must estimate the background contribution in the inclusive distribution. A schematic view of the background contribution is shown in Figure 4.8.

We have two methods for background estimation. In the first we look at the direction perpendicular to the jet. This is assumed to be the region least likely to contain jet contributions. In the second method we randomly assign the tracks of event new  $\phi$  and  $\eta$  values. The result is thus guaranteed to be uncorrelated.

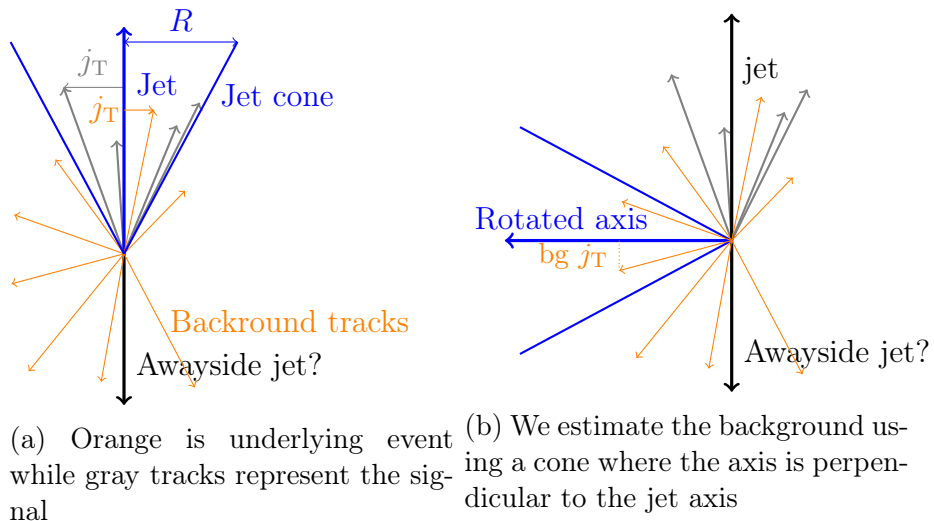


Figure 4.8: Background estimation

### 4.4.1 Perpendicular cone background

As a primary method to estimate the background we look at regions of the detector where there are no tracks from jets, but only uncorrelated tracks from the underlying event. The underlying event is thus estimated by looking at an imaginary jet cone perpendicular to the observed jet axis ( $\frac{\pi}{2}$  Rotation in azimuthal angle,  $\phi$ ).

After calculating the  $j_T$  values for tracks in the jet, we rotate the jet axis by  $\frac{\pi}{2}$  in positive  $\phi$  direction. We check that there are no other jets closer than  $2R$  to the rotated axis. Otherwise background calculation is skipped for this jet. Probability of this happening is 1-2% depending on the jet  $p_T$  bin.

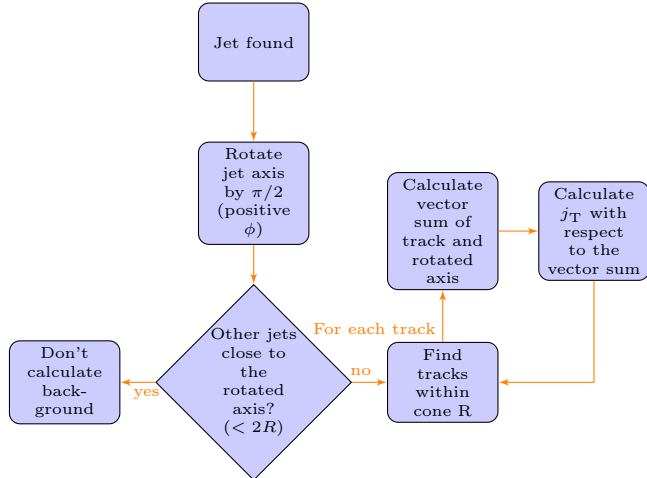


Figure 4.9: Flowchart representation of the perpendicular cone background procedure

If we don't find other jets in the vicinity we move on to estimate the background. We find all tracks within a cone of radius  $R$  around the rotated axis and calculate  $j_T$  of these tracks with respect to the rotated axis.

This background procedure is a part of the reason for using charged tracks inside a fixed size cone, instead of jet constituents. To be representative of the actual underlying event contribution the size and shape of the background estimation region should match the area where  $j_T$  is calculated. The irregular shape of a jet would be hard to take into account when calculating background. Thus the regions are made to match by considering fixed size cones for  $j_T$ .

One additional consideration is the issue of auto-correlations as the jet axis is simply a vector sum of all its constituents. Thus having an additional track in the jet from the underlying event moves the jet axis towards this track. Since the axis is now closer to the track, it has a smaller  $j_T$  value. Assuming a  $1 \text{ GeV}/c$  background track at the edge of a  $R = 0.4$  cone the  $j_T$  value would be  $0.4 \text{ GeV}/c$ . If this is added to a  $5 \text{ GeV}/c$  jet, the  $j_T$  value becomes  $0.33 \text{ GeV}/c$  after the jet axis moves. In a  $50 \text{ GeV}/c$  jet it would be  $0.39 \text{ GeV}/c$ . This is a region where the inclusive  $j_T$  distribution is dominated by background. The distribution is also steeply falling. Overestimating the background can lead to a situation where the background estimation exceeds the inclusive distribution.

To take this effect into account we can't use a fixed axis for background, but it has to behave like a jet would when additional tracks are added. Thus before calculating  $j_T$  values we make a vector sum of the track and the axis used for background, which is either the perpendicular cone axis or the random axis depending on the background method. In each case the momentum of this background axis

is assumed to be the same as the jet which initiated the background estimation.

In p–Pb data there is on average about one underlying event track in a  $R = 0.4$  cone. If there would be more, one should consider taking the vector sum of all tracks inside the cone. As there is usually only one track and if there are more it's unlikely that more than one has high momentum, taking the vector sum track-by-track should be enough.

#### 4.4.2 Random background

In the random background method we look at all tracks in the event, except for tracks close to jets found by the jet algorithm. We randomly assign new  $\eta$  and  $\phi$  values to all tracks using uniform distributions with  $|\eta| < 1.0$ .  $p_T$  values are kept the same. To increase statistics there is a possibility to create a number of random tracks for each actual track. In the analysis we do this 10 times for each track. Again the track  $p_T$  value is kept the same.

We create a random jet cone from uniform  $\eta$  and  $\phi$  distributions. Here  $|\eta| < 0.25$ . Now we calculate  $j_T$  of the random tracks with respect to the random cone axis. As in the perpendicular cone method auto-correlations are added before calculating  $j_T$ .

Comparison between perpendicular cone and random background in Figure 4.10. The advantage of the random background method is that the procedure can be repeated several times for each event, which allows producing additional statistics. However, it seems that, especially in the highest  $p_{T,jet}$  bins there is some jet contribution left at the high end. Naturally there is no correlation between the tracks and the background axis, but if some high momentum tracks originating from jets were not subtracted and happen to hit the edge of the background cone, they can increase the high  $j_T$  yield in the background estimation.

We observe that the results from perpendicular cone background show no observable change between  $p_{T,jet}$  bins. It is a good indication that the background is actually dominated by the underlying event over the entire  $j_T$  region.

Thus as a primary method of background estimation the perpendicular cone method is used. The random background method is used to estimate systematic contributions by comparing the final results obtained with this method to the results obtained from the perpendicular cone method.

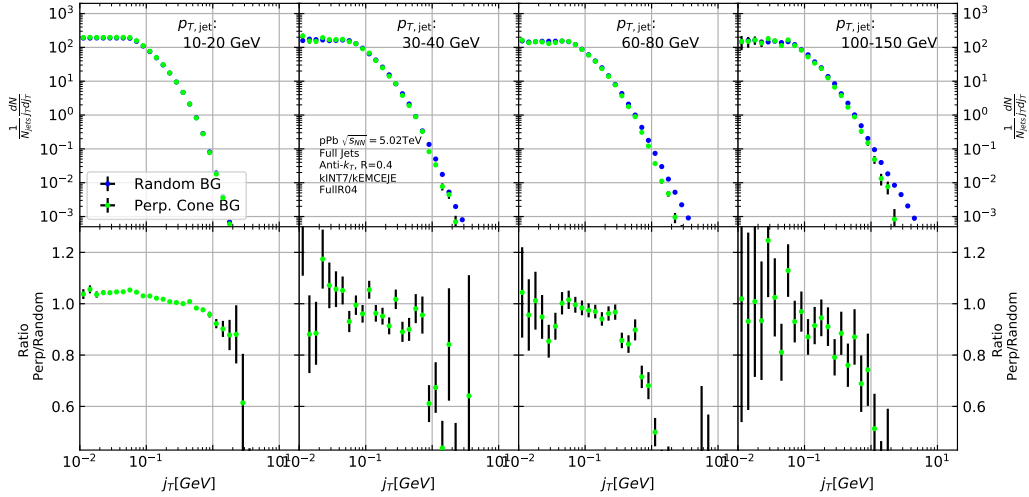


Figure 4.10:  $j_T$  background with two different methods

## 4.5 Fitting

After unfolding and background subtraction the resulting signal distributions are fitted with a 2 component function shown in Eq. 4.23. Gaussian distribution is used for low  $j_T$  and an inverse gamma function is used for high  $j_T$ . The Gaussian is taken to have the centre at  $j_T = 0$ . In total this gives 5 parameters. The fitting procedure was inspired by the dihadron  $j_T$  analysis by ALICE [277]. The complete fitting function is

$$\frac{1}{N_{\text{jets}}} \frac{dN}{j_T dj_T} = \frac{B_2}{B_1 \sqrt{2\pi}} e^{-\frac{j_T^2}{2B_1^2}} + \frac{B_3 B_5^{B_4}}{\Gamma(B_4)} \frac{e^{-\frac{B_5}{j_T}}}{j_T^{B_4+1}}, \quad (4.23)$$

where  $\Gamma(x)$  is the gamma function and  $B_n$  are parameters of the fit.

To achieve stable results the fitting is performed in two steps. First both components are fitted separately. Gaussian component is fitted to the low end of  $j_T$ . Inverse gamma component is fitted to  $j_T$  above 1 GeV/c. After getting the results from the individual fits they are combined into a single function with initial values from the individual results and an additional fit is performed.

After getting the fit function  $\sqrt{\langle j_T^2 \rangle}$  (RMS) and yield values are extracted separately from each component. The narrow component RMS is

$$\sqrt{\langle j_T^2 \rangle} = \sqrt{2} B_1, \quad (4.24)$$

and the wide component RMS value is calculated as

$$\sqrt{\langle j_T^2 \rangle} = \frac{B_5}{\sqrt{(B_4 - 2)(B_4 - 3)}}, \quad (4.25)$$

where it is required that  $B_4 > 3$ .

The statistical errors can be calculated with the general error propagation formulas. As a result one gets errors for the narrow component RMS

$$\delta \sqrt{\langle j_T^2 \rangle} = \sqrt{2} \delta B_1 \quad (4.26)$$

and for the wide component RMS

$$\delta \sqrt{\langle j_T^2 \rangle} = \sqrt{\left( \frac{(5 - 2B_4) B_5 \delta B_4}{(2(B_4 - 2)(B_4 - 3))^{\frac{3}{2}}} \right)^2 + \left( \frac{\delta B_5}{\sqrt{(B_4 - 2)(B_4 - 3)}} \right)^2}. \quad (4.27)$$

# Chapter 5

## Systematic uncertainties

The main systematic uncertainties in this analysis come from the background estimation, the unfolding procedure and uncertainty in the tracking efficiency. The systematics in background estimation were studied using an alternative method to extract the background, the random background method and the uncertainty in tracking was studied by varying tracking efficiencies in a PYTHIA simulation.

The systematic uncertainty that arises from the unfolding procedure is estimated by performing the unfolding with two separate methods. Data corrected by the iterative unfolding method are used as the results and the SVD unfolding method is employed to estimate the uncertainty. In a PYTHIA closure test the true distribution was in general found to be between the unfolded distributions from the iterative and SVD method. The difference between the methods when unfolding data should give a reasonable estimate of the unfolding uncertainty. The resulting uncertainty is below 8% for both wide and narrow component RMS.

### 5.1 Background

The uncertainty coming from background calculation is estimated by subtracting the background separately for the perpendicular cone and random background methods. Comparisons of the resulting signal distributions are shown in Figure 5.1.

Fits are then performed on both perpendicular cone and random background signals. Difference between them is taken as the systematic uncertainty. The fits for individual bins from the random background method are shown in Figure 5.2. Resulting differences between the methods for different components are shown in Figure 5.3. The dotted lines are put at  $\pm 5\%$  for the narrow component and at  $\pm 8\%$  for the wide component. These are taken as systematic estimates for the entire  $p_{T,\text{jet}}$  range.

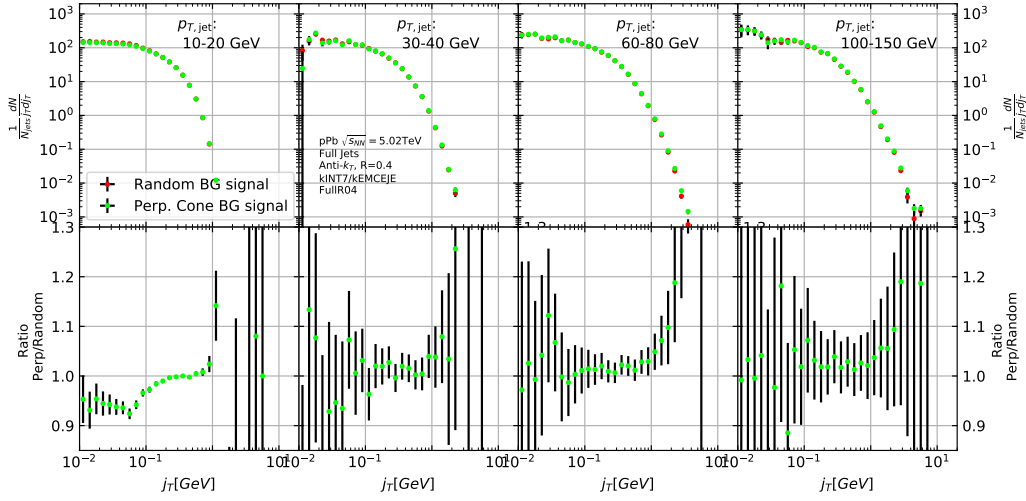


Figure 5.1: Comparison of the effect of background method on  $j_T$  signal

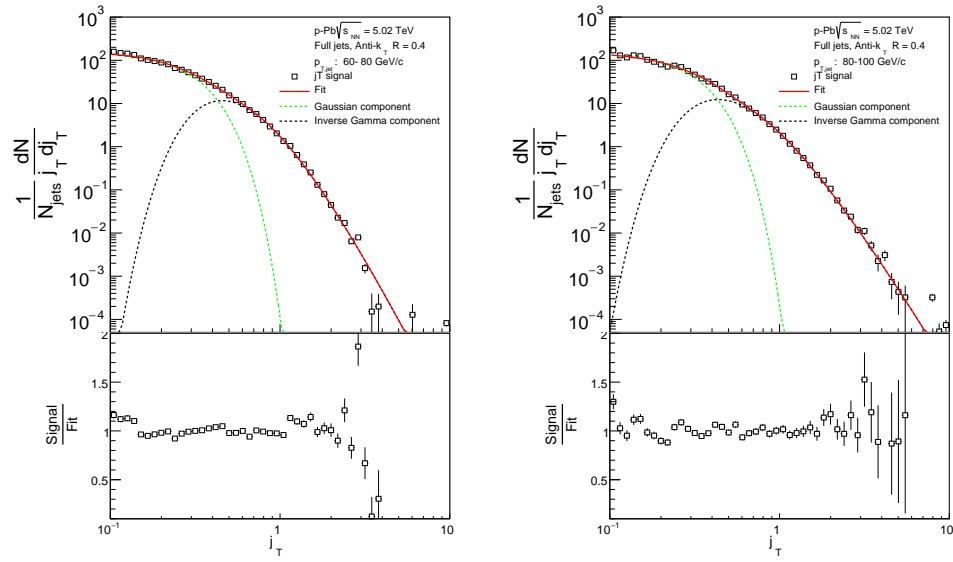


Figure 5.2:  $j_T$  signal with random background subtraction fits in different jet  $p_T$  bins

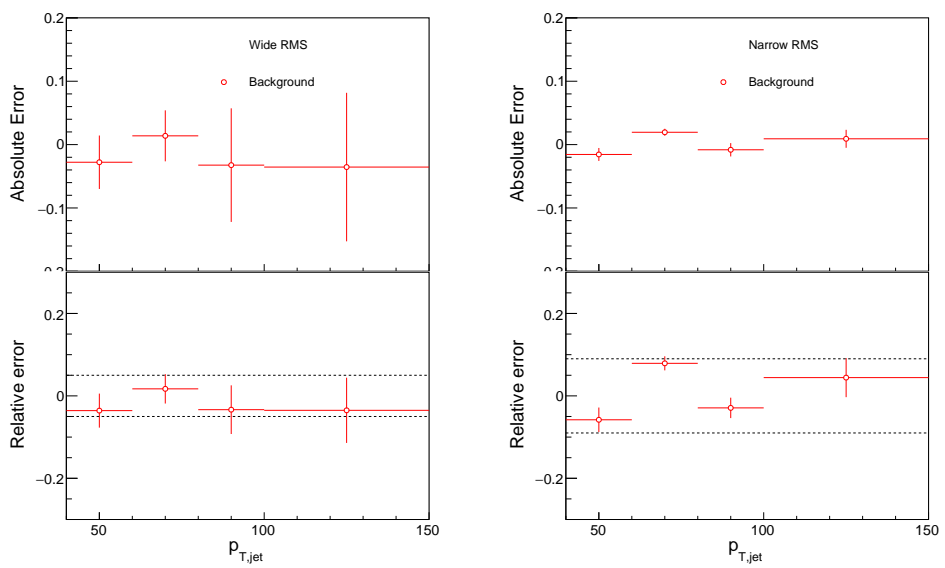


Figure 5.3: Differences between perpendicular cone and random background subtraction in the resulting RMS values

## 5.2 Unfolding

Unfolding is the second major source of systematic uncertainty. To estimate the uncertainty related to the unfolding procedure several checks are performed. The main systematic uncertainty estimation comes from comparing results performed using both SVD and Bayesian unfolding. Difference between the methods is taken as the systematic uncertainty. Since SVD unfolding does not have a two dimensional option, the unfolding is done bin by bin.

As in the background systematic estimation, fits are performed for both cases separately. Resulting differences between the methods for different components are shown in Figure 5.4. The dotted lines are at  $\pm 8\%$  for both components. These are taken to be the systematic uncertainty related to unfolding.

Several other systematic checks were performed with the Bayesian unfolding procedure. They are described in the following sections. As these are small compared to the main uncertainty they are not included separately.

### 5.2.1 Effect of number of iterations

The iterative unfolding algorithm permits the change of number of iterations. The unfolding procedure was carried out using different numbers of iterations. The results from these different cases are shown in Figure 5.5. The results are compared to the default unfolding algorithm with 4 iterations. The difference in results between the different cases is mostly less than 2.5%.

### 5.2.2 Effect of different prior

The iterative algorithm requires a prior estimate of the shape of the distribution. As a default prior the truth (particle level) distribution is used. To test the effect of changing the prior we instead use the unfolded  $j_T$  distribution as prior. The results are compared to the unfolding algorithm with the default prior. This is shown in Figure 5.6. The difference in results between the different cases is mostly less than 2.5%.

### 5.2.3 Effect of $p_T$ truncation

As an additional check the unfolding is carried out with different  $p_{T,jet}$  truncation values. By default the full range of  $p_{T,jet} > 5 \text{ GeV}/c$  is used. We test the unfolding by only using the response matrix for  $p_{T,jet} > 10 \text{ GeV}/c$ . The results of this test are shown in Figure 5.7. The effects are strongest in the lower  $p_{T,jet}$  bins. Also in this case the difference is less than 2.5 % in all  $p_{T,jet}$  bins.

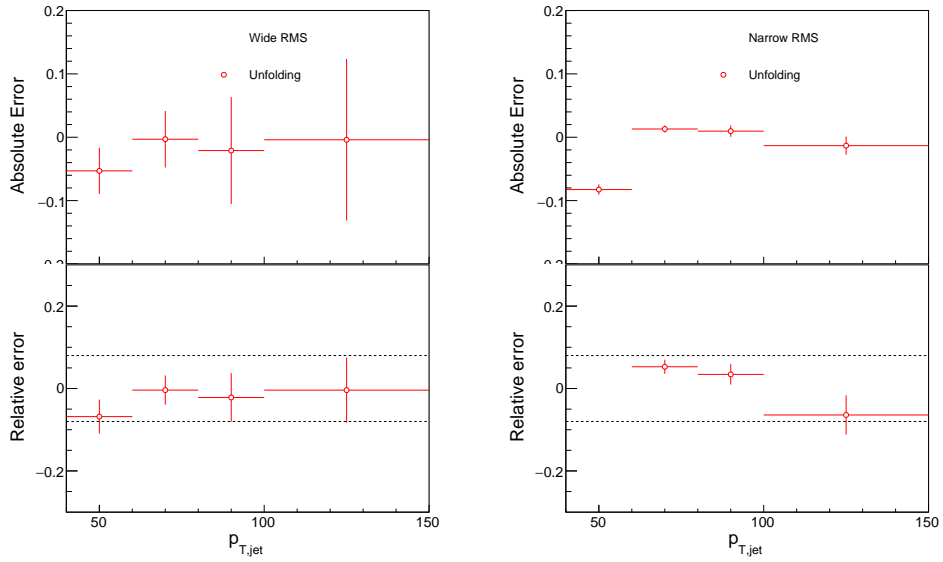


Figure 5.4: Differences between Bayesian and SVD unfolding in the resulting RMS values

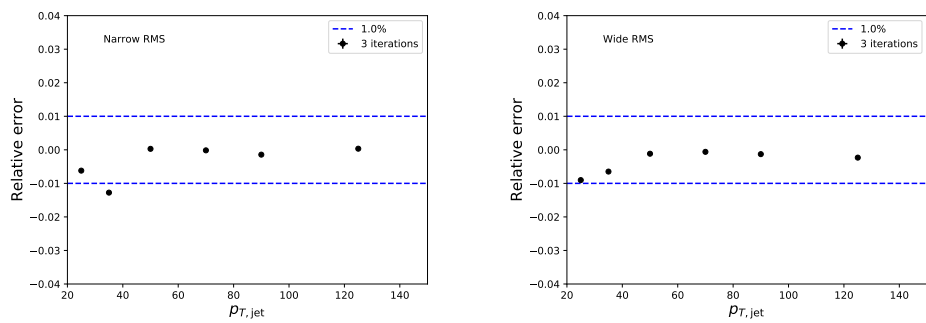


Figure 5.5: Unfolding with different number of iterations

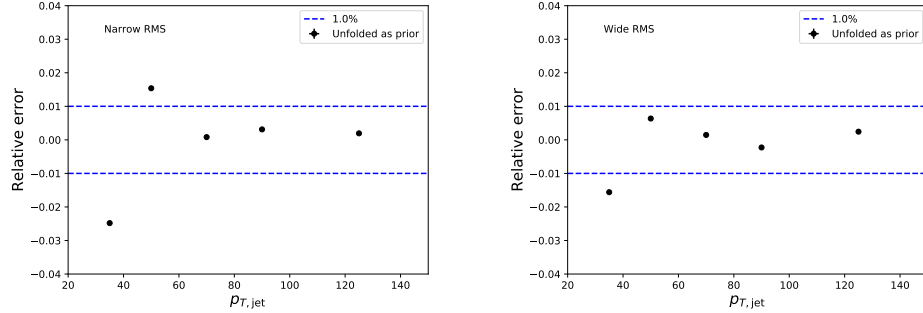


Figure 5.6: Effect of changing prior from true distribution in PYTHIA to the unfolded distribution

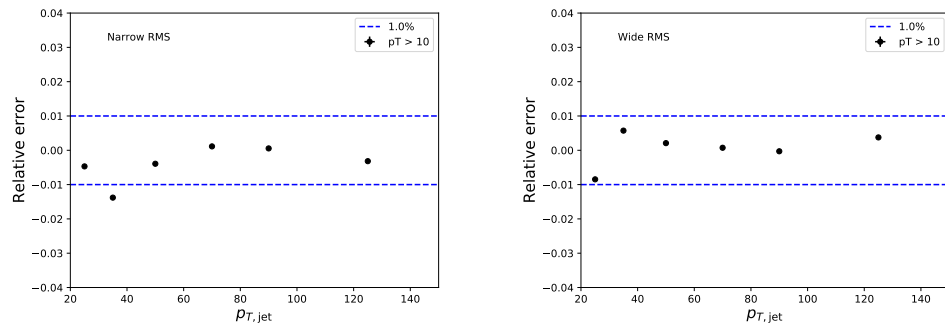


Figure 5.7: Effect of changing minimum jet  $p_T$  used in unfolding from 5  $\text{GeV}/c$  to 10  $\text{GeV}/c$

### 5.3 Tracking

Systematic effects originating from uncertainty in the tracking efficiency are estimated through a PYTHIA simulation, where an artificial inefficiency of 3% is introduced i.e. 3 % of tracks are randomly removed from each event. The effect of this artificial inefficiency is shown in Figure 5.8. The systematic uncertainties assigned to tracking efficiency are 4 % for the narrow component and 5 % for the wide component.

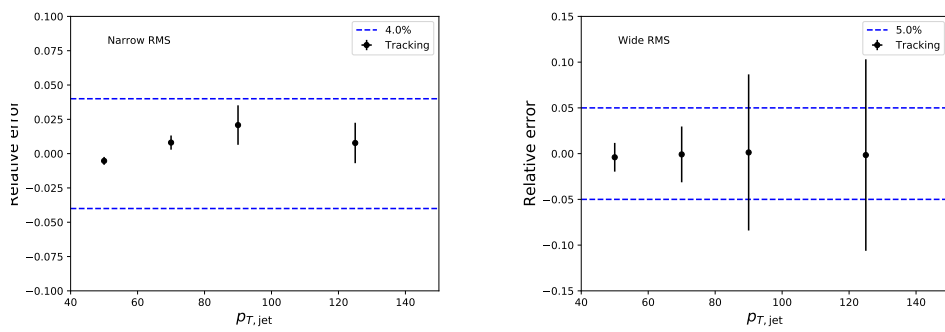


Figure 5.8: Relative systematic uncertainties resulting from uncertainty in tracking efficiency

## 5.4 EMCAL clusters

The analysis uses EMCAL clusters only in the reconstruction of jets. Thus the only way uncertainty in EMCAL performance can affect the results is through modification of jet momentum or axis.

Uncertainty related to the EMCAL energy scale was estimated by scaling cluster energies up and down by 2 % in a PYTHIA particle level simulation. Similarly the jet momentum was scaled by  $\pm 2\%$  when determining the jet  $p_T$  bin. In this analysis EMCAL is used only in jet reconstruction, not for calculating  $j_T$ . The only ways EMCAL uncertainty can affect the analysis are changes in jet energy and jet axis. Jet axis shouldn't significantly change, so the main contribution should be changes in jet  $p_T$  bin.

The resulting differences in the inclusive  $j_T$  distributions are shown in Figure 5.9. Qualitatively the effect of scaling cluster energies is the same as scaling the jet energies.

Like in the previous cases fits are performed for the unscaled case and for cases with  $\pm 2\%$  scaling. The resulting systematic uncertainties are shown in Figure 5.10. The uncertainty is taken to be 1% for both components.

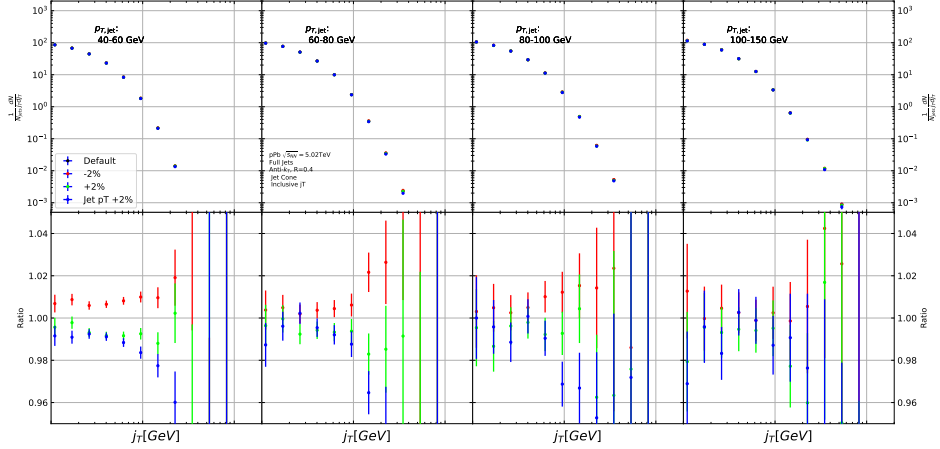


Figure 5.9: Results from PYTHIA simulations with Cluster energies scaled up and down by 2 %. Additionally jet momenta were scaled by 2 % when determining the jet  $p_T$  bin.

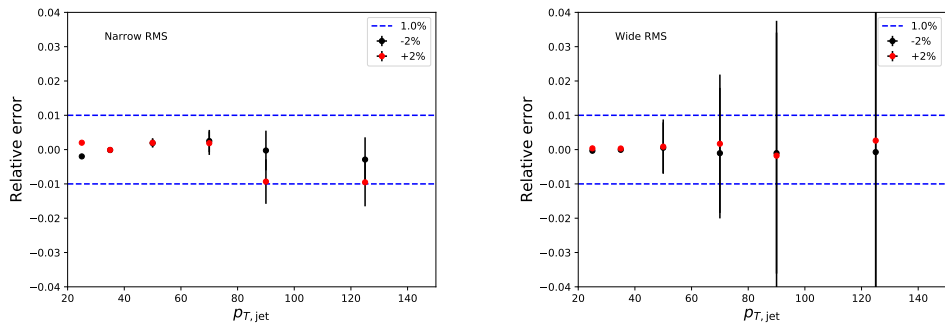


Figure 5.10: Relative systematic uncertainties resulting from cluster energy uncertainty.

## 5.5 Summary of systematic uncertainties

The different source of the systematic uncertainty are considered as uncorrelated and the values of each source are summed in quadrature. Resulting systematic uncertainties are shown in Table 5.1. The different source of the systematic uncertainty are considered to be uncorrelated and are thus combined bin-by-bin in quadrature to get the total systematic uncertainties. The resulting uncertainty is approximately 10 % for the wide component RMS and 13 % for the narrow component RMS.

Table 5.1: Summary of systematic uncertainties

Systematic	Wide RMS	Narrow RMS
Background	5 %	9 %
Unfolding	8 %	8 %
Tracking	4 %	5 %
EMCal	1 %	1 %
Total	10 %	13%

# Chapter 6

## Results

In this section I present the final results for  $j_T$  signals. After unfolding and subtracting the background contribution we get the final  $j_T$  distributions. Figure 6.1 shows  $j_T$  distributions for two different  $p_{T,jet}$  bins with  $60 \text{ GeV}/c < p_{T,jet} < 80 \text{ GeV}/c$  and  $100 \text{ GeV}/c < p_{T,jet} < 150 \text{ GeV}/c$ . Additional  $p_{T,jet}$  bins are shown in appendix B. The distributions get wider with increasing  $p_{T,jet}$ . In part this is explained by kinematics; In a jet cone the cone size,  $R$ , sets limits on the possible  $j_T$  values. For a given  $p_{T,track}$  the maximum  $j_T$  value is approximately

$$j_{T\max} \approx R \cdot p_{T,track}, \quad (6.1)$$

using the small angle approximation.

We fit the distribution using the two component fit function presented in Section 4.5. These are also shown in Figure 6.1. Fitting a Gaussian alone to the entire  $j_T$  distribution will produce a similar result as the Gaussian component in the two component fit. Thus the gaussian fit alone can't describe the full jet  $j_T$  distribution.

To characterise the widening of the  $j_T$  distribution we can then extract the RMS, i.e.  $\sqrt{\langle j_T^2 \rangle}$ , values of the fits. Resulting RMS values with systematic errors are shown separately for the two components in Figure 6.2. Here it is seen that the width of the narrow component shows only a weak dependence on the transverse momentum of the jet,  $p_{T,jet}$ . The RMS value of the wide component on the other hand increases with increasing  $p_{T,jet}$ .

The RMS values for both components are compared to PYTHIA and Herwig simulations as shown in Figure 6.3. All the PYTHIA models reproduce the data well, both the wide and narrow component. For the narrow component Herwig gives RMS values comparable to the data. On the other hand, Herwig produces larger wide component  $\sqrt{\langle j_T^2 \rangle}$  values than data and PYTHIA, and this difference seems to get larger with increasing  $p_{T,jet}$ .

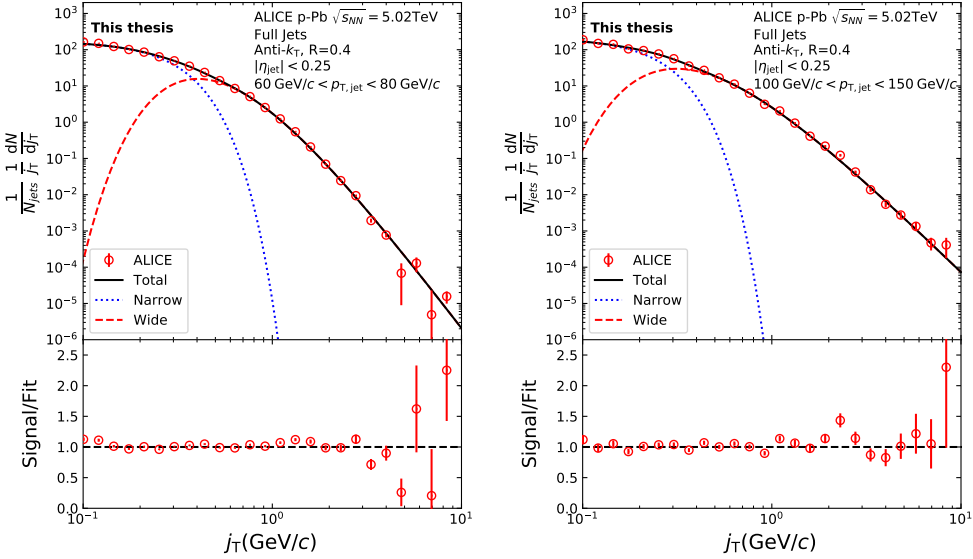


Figure 6.1:  $j_T$  signal distributions fitted with the two component model are shown in different jet  $p_T$  bins.

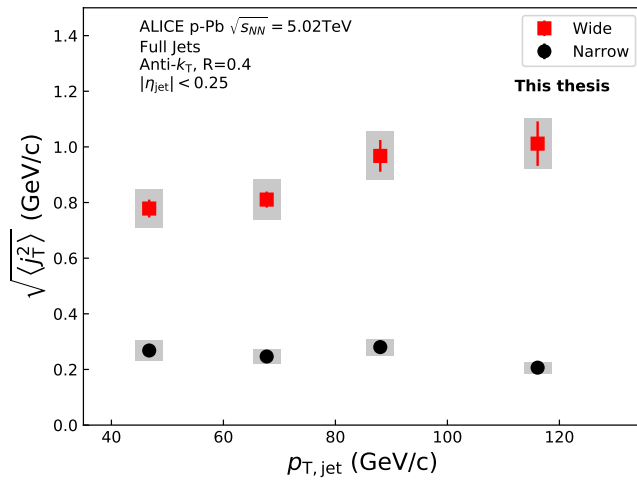


Figure 6.2: RMS values extracted from the fits are shown for the Gaussian (narrow) and inverse gamma (wide) components.

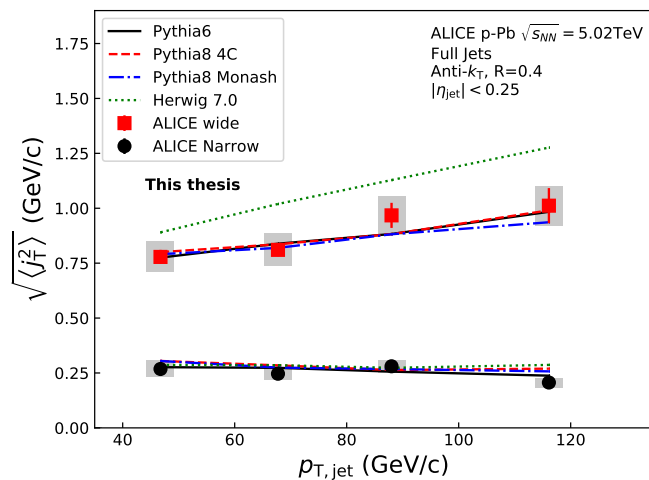


Figure 6.3: RMS values extracted from the fits are compared to Monte Carlo models. PYTHIA reproduces the data well for both the narrow and wide components. Herwig produces wider distributions.

## 6.1 High multiplicity events

The analysis was repeated taking only events with high multiplicity. Three different multiplicity percentile cuts were used; 10%, 1% and 0.1%. The centrality estimations were given by the V0A estimator. Resulting  $j_T$  signal distributions are shown in Figure 6.4. From the figure one can observe no modification within the errors when tighter multiplicity cuts are introduced.

As described in Section 1.5 no conclusive evidence of jet modification in p–Pb collisions has been observed. However, all previous observations have been done for minimum bias events. Most observables are based on measuring yield instead of jet shape and are thus sensitive to biases in the centrality selection. No previous jet shape measurements have been performed in high multiplicity p–Pb events, where collective motion was observed.

As the statistics are limited in the high multiplicity runs, it was hard to achieve stable fits to the distributions. Thus the RMS values are not shown.

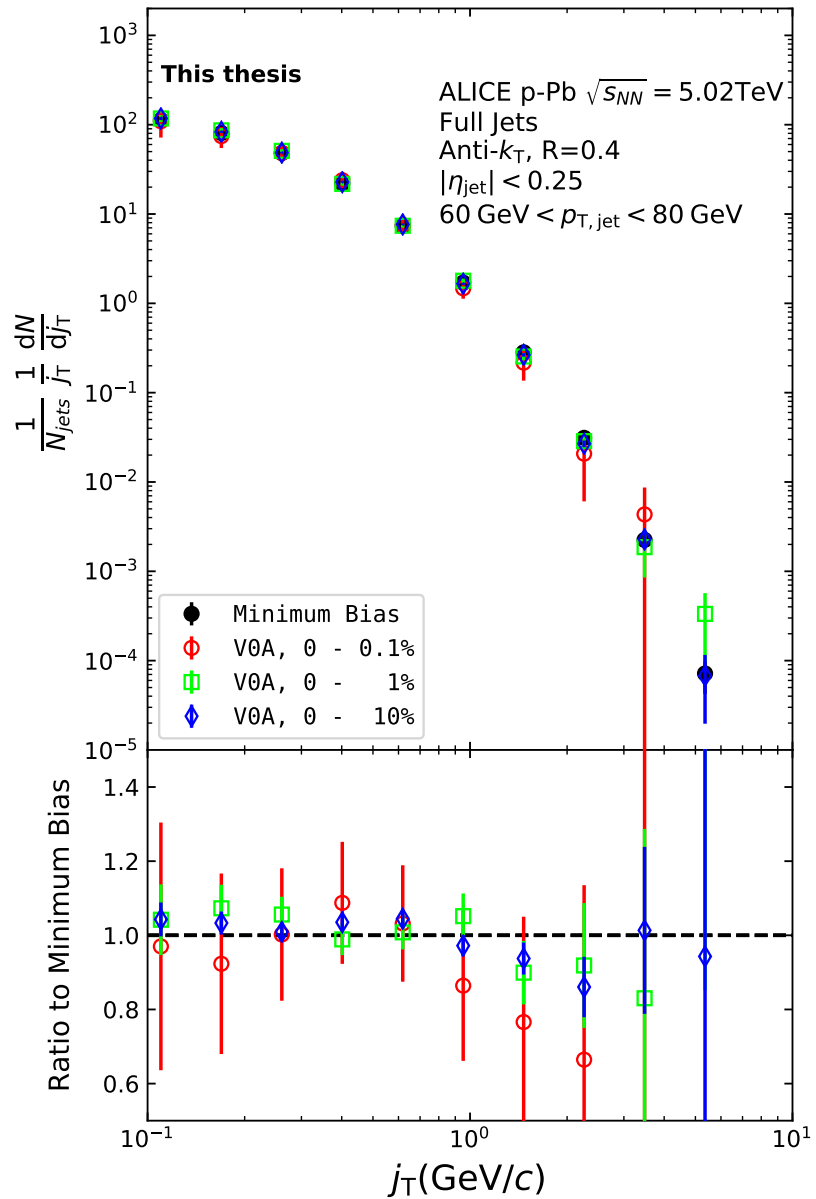


Figure 6.4:  $j_T$  distributions are shown for various multiplicity bins in p-Pb collisions.

# Chapter 7

## Discussions

### 7.1 Comparing dihadron and jet $j_T$ results

The jet fragmentation transverse momentum  $j_T$  has been studied previously at ALICE using dihadron correlations [277]. The study took the leading hadron in each event and calculated  $j_T$  for any near-side tracks with respect to the leading hadron. Thus there is no kinematical limit to  $j_T$  from the jet cone. In the analysis the background shape is estimated using pairs with large  $\Delta\eta$ . The normalisation of the background is done when fitting the  $j_T$  distribution. The inclusive distribution is fitted with a three component function, where one of the components is the background contribution. After subtracting the background, what remains is the signal distribution characterised by the two components. The resulting signal distribution from the analysis is shown in Figure 7.1. The analysis was the first to introduce this factorisation of  $j_T$  into components.

To constrain the effects from kinematical differences between  $p_{T,\text{trigger}}$  bins the analysis used bins of the fragmentation variable  $x_{\parallel}$ , which is the projection of the associated particle momentum  $\vec{p}_a$  to the trigger particle momentum  $\vec{p}_t$ , normalised by the trigger particle momentum

$$x_{\parallel} = \frac{\vec{p}_t \cdot \vec{p}_a}{\vec{p}_t^2}. \quad (7.1)$$

The RMS results from the fitting in both pp and p–Pb collisions are shown in Figure 7.2. Qualitatively the results are similar to jet  $j_T$  results. The RMS value of the wide component has an increasing trend with respect to  $p_{T,t}/p_{T,jet}$ , while the RMS value of the narrow component stays constant. Both components are well described by PYTHIA simulations. As seen in the figures there is no difference between minimum bias pp and p–Pb results in the dihadron analysis.

Comparison between RMS values in dihadron  $j_T$  [277] and jet  $j_T$  is shown in Figure 7.3. The dihadron trigger  $p_T$  bins are converted to jet  $p_T$  bins and vice

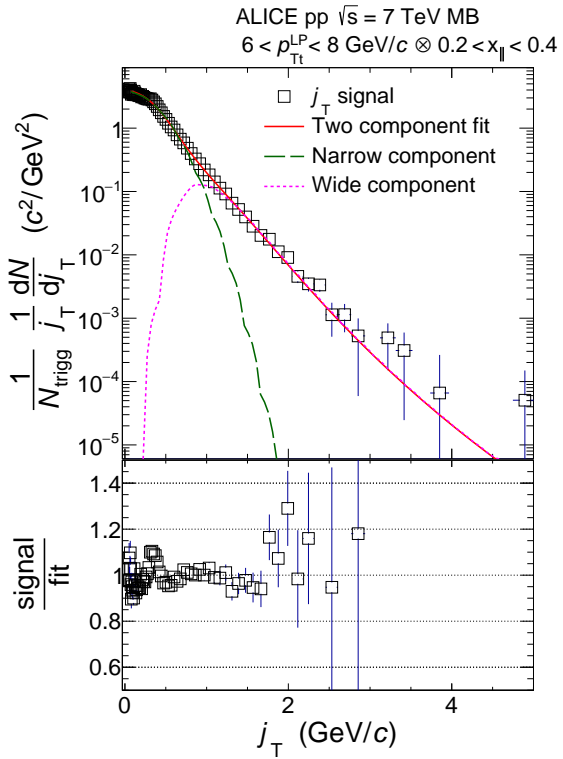


Figure 7.1: Measured  $j_T$  signal distribution using dihadron correlations is shown for  $6 < p_{Tt} < 8$  and  $0.2 < x_{||} < 0.4$ . The distribution is fitted with the same two component model used in this thesis. Figure from [277].

versa. Bin-by-bin comparison is still not possible, but general features can be identified.

The trends are similar in dihadron and jet  $j_T$  results. Wide component RMS values tend to increase with increasing  $p_{T,\text{trigger}}/p_{T,\text{jet}}$ . For  $x_{||} < 0.4$  Narrow component RMS increases slightly at low  $p_{T,\text{trigger}}$  in dihadron analysis. This trend changes between  $x_{||}$  bins; In larger  $x_{||}$  bins the narrow component RMS is closer to constant as is the case for jet  $j_T$ .

The most striking difference is that dihadron  $j_T$  gives wider distributions with larger RMS values. There are several possible causes for this difference. First, in jet analysis the cone size limits width and thus the RMS values. The effect of this limitation can be studied by changing the cone size as is described in Section 7.1.1.

Second, the leading track is an imperfect estimate of the jet/original parton. Because the leading track in general is at an angle compared to the jet axis, the resulting  $j_T$  values are different. In practice the jet axis found by the jet finding algorithm tends to minimize the average  $j_T$  of jet constituents. Thus the yield

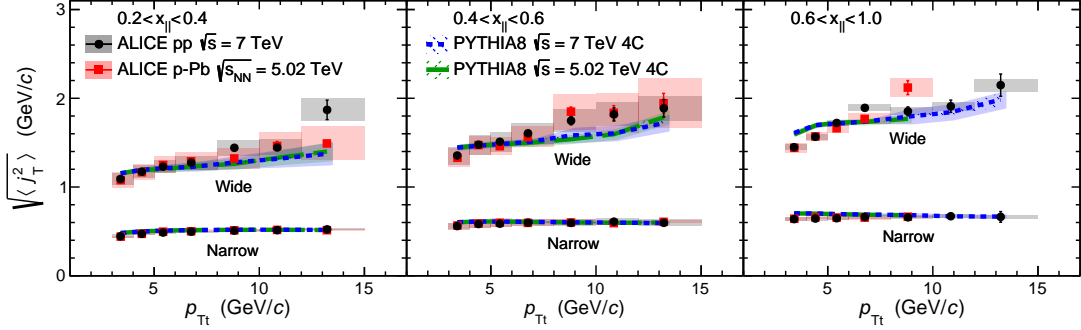


Figure 7.2: RMS values of the narrow and wide  $j_T$  components in the dihadron correlation analysis. Results from pp collisions at  $\sqrt{s} = 7$  TeV (circular symbols) and from p–Pb collisions at  $\sqrt{s_{NN}} = 5.02$  TeV (square symbols) are compared to PYTHIA 8 tune 4C simulations at  $\sqrt{s} = 7$  TeV (short dashed line) and at  $\sqrt{s} = 5.02$  TeV (long dashed line). Different panels correspond to different  $x_{\parallel}$  bins with  $0.2 < x_{\parallel} < 0.4$  on the left,  $0.4 < x_{\parallel} < 0.6$  in the middle, and  $0.6 < x_{\parallel} < 1.0$  on the right. The statistical errors are represented by bars and the systematic errors by boxes. Figure from [277].

at high  $j_T$  is limited and the RMS values are smaller. The effect of having the leading hadron as reference instead of the jet axis is discussed in Section 7.1.2

Third, the results from the dihadron analysis are done in  $p_{T,\text{trigger}}$  bins. This favours hard jets, i.e. jets where the leading hadron carries a large momentum fraction and the jet multiplicity is small. In  $p_{T,\text{jet}}$  bins jets are more likely to be soft, i.e. they have a small leading momentum fraction and high multiplicity jets.

### 7.1.1 Different $R$ parameters

The size of the jet cone gives a limit for  $j_T$ . For a track with a fixed momentum  $p$  this is a hard limit. This is conveniently seen as  $j_{T,\text{max}}$  can be given in terms of cone size  $R$  and momentum  $p$ . In the small angle approximation limit

$$j_{T,\text{max}} \approx p \cdot R. \quad (7.2)$$

Thus for tracks with  $p_{T,\text{track}} < p_{T0}$ , must be  $j_T < p_{T0} \cdot R$ . This is illustrated in Figure 7.4.

We studied the effect of cone sizes on  $j_T$  distribution with a PYTHIA simulation. Distributions with different cone sizes in different  $p_{T,\text{jet}}$  bins are shown in Figure 7.5. The increase of high  $j_T$  with increasing cone size,  $R$ , is clearly seen in the individual  $j_T$  distributions. At low  $j_T$  there is no change within the errors.

When looking at the RMS values from wide component we see an increase

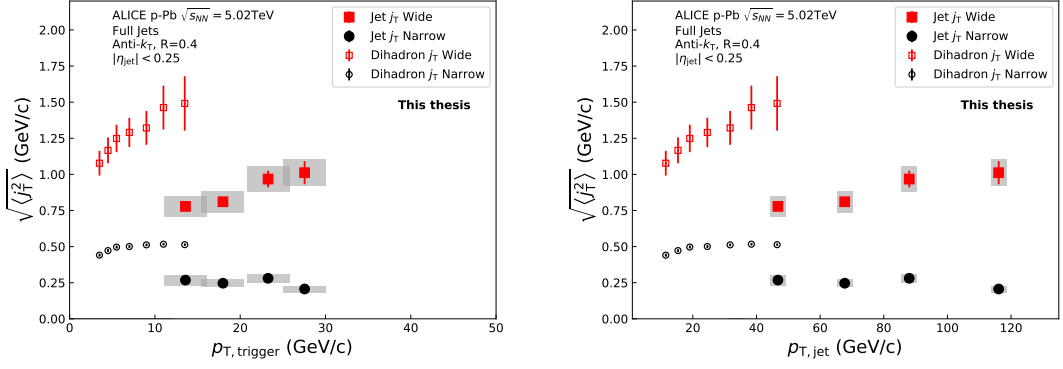


Figure 7.3: Jet  $j_T$  results are compared to results obtained in the dihadron analysis [277]. Dihadron trigger  $p_T$  bins are converted to jet  $p_T$  bins using observed mean  $p_{T,\text{jet}}$  values in  $p_{T,\text{trigger}}$  bins. Dihadron results are for  $0.2 < x_{||} < 0.4$ .

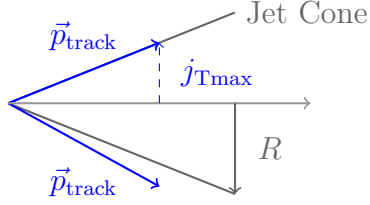


Figure 7.4:  $j_T$  has maximum value defined by the cone size and track momentum  $\vec{p}_{\text{track}}$

or decrease of about 10% when going from  $R = 0.4$  to  $R = 0.5$  or  $R = 0.3$ , respectively. This is seen in Figure 7.6. The message from narrow component RMS values is less clear. At low jet  $p_T$  the behaviour is similar, but at high  $p_T$  the order is reversed.

### 7.1.2 Leading tracks versus jet as reference

In comparison to the leading hadron the jet axis from jet reconstruction should provide a better estimate of the original parton. The assumption is that because the leading hadron is an imperfect estimate of the jet axis, low  $j_T$  tracks should on average be shifted to higher  $j_T$ .

Because the leading track is at an angle compared to the jet axis, the resulting  $j_T$  values are different. In practice the jet axis found by the jet finding algorithm tends to minimise the average  $j_T$  of jet constituents, as at least the hardest constituents should be close to the jet axis. Thus the yield at high  $j_T$  is reduced and the RMS values get smaller. On the other hand, when using the leading hadron as

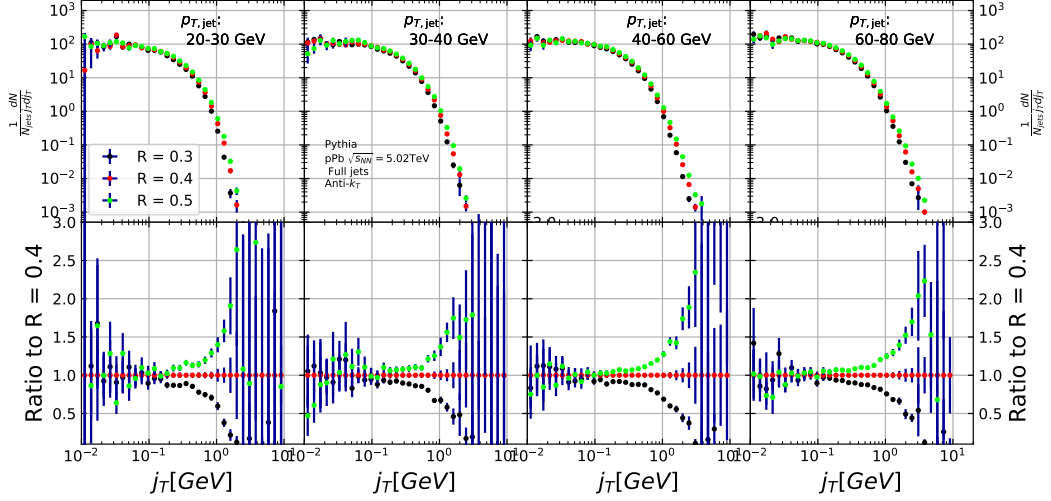


Figure 7.5: Effect of changing cone size on  $j_T$  distributions. The change is done both for the  $R$  parameter in the anti- $k_T$  algorithm, and for the size of the cone where  $j_T$  is calculated.

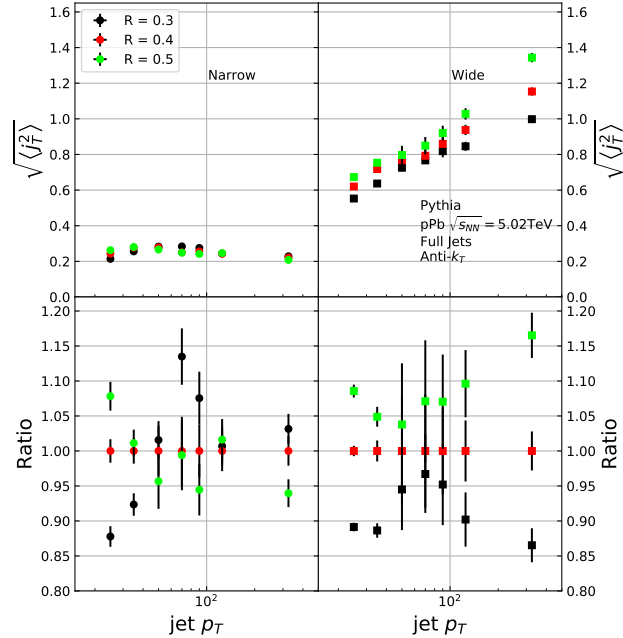


Figure 7.6: Effect of changing  $R$  parameter in jet finding on narrow and wide component RMS values. Wide component RMS values increase with increasing cone size.

a reference, it is naturally missing from the set of tracks for which  $j_T$  is calculated. This causes a decrease in the yield at low  $j_T$ .

We performed a PYTHIA study where  $j_T$  was calculated with respect to the leading track momentum, instead of the jet axis. The results are shown in Figure 7.7. The resulting  $j_T$  distributions are significantly wider than  $j_T$  distributions from using the jet axis as reference. The effect seems to be larger than that seen in comparing different  $R$  values.

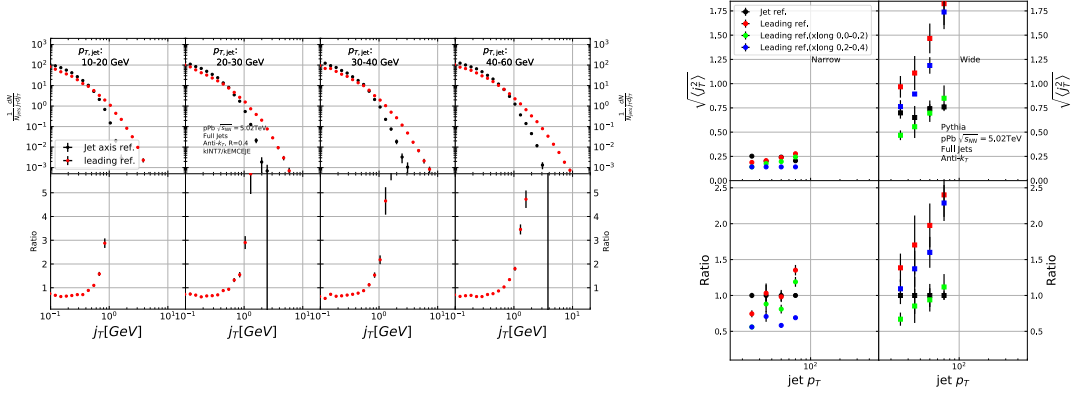


Figure 7.7: Results of calculating  $j_T$  with respect to the leading hadron, instead of the jet axis in a PYTHIA simulation are shown.

A direct comparison between jet and dihadron  $j_T$  measurements is not possible. But combined with the  $R$  dependence of  $\sqrt{\langle j_T^2 \rangle}$  the difference between  $\sqrt{\langle j_T^2 \rangle}$  values in jet and dihadron analyses can be quantitatively understood.

# Chapter 8

## Summary

In this thesis I have studied the jet fragmentation transverse momentum at  $\sqrt{s_{NN}} = 5.02$  TeV in p–Pb collisions. The analysis was performed using jets reconstructed with the anti- $k_T$  algorithm. The resulting  $j_T$  distributions were fitted with a two component model, which allows us to separate two distinct components. The width of the narrow component was found to depend weakly on jet  $p_T$ . The narrow component has been associated with the non-perturbative hadronisation process. This is consistent with the assumption that hadronisation is universal, i.e. it doesn't depend on the hard scattering.

The width of the wide component was found to get larger with increasing  $p_{T,jet}$ . This is in part explained by the changing kinematical limits when going to higher  $p_{T,jet}$  which allows higher  $p_{T,track}$ . Additionally the larger phase space allows stronger parton splitting.

Both the narrow and wide component RMS values were well described by PYTHIA , but Herwig gave larger RMS values for the wide component than data. In the narrow component there was no difference between the models. Both describe the data well. This component was associated with hadronisation. At least in this context the different hadronisation algorithms of PYTHIA (string model) and Herwig (cluster model) give similar results.

Similar analysis has been performed with dihadron correlations [277]. Although a direct comparison between the results is not possible, they are qualitatively compatible with each other. The difference is understood to come from the different  $j_T$  reference, the cone size limitation in jet  $j_T$  analysis and the kinematical bias that arises from using  $p_{T,trigger}$  bins which favours harder jets than using  $p_{T,jet}$  bins. The dihadron analysis saw no difference between results in pp and p–Pb datasets and concluded that there were no cold nuclear matter effects. The same is expected to be true for the jet  $j_T$ . This is further supported by the agreement between PYTHIA and data as PYTHIA results are for pp collisions.

To study possible QGP effects in high multiplicity p–Pb collisions the analysis

was repeated using different multiplicity selections. So far no jet observables have shown conclusive evidence of modification in  $p$ -Pb events. However these are primarily based on measuring yield, which makes them vulnerable to biases when selecting for multiplicity. Thus these measurements have been only performed in minimum bias events. As  $j_T$  is based on shape on a per-jet basis, it should not be sensitive to these selection biases. No effect was seen in any of the multiplicity selections. However, with the statistics available, the effect should be quite large ( $\gtrapprox 20\%$ ) to be visible.

Naturally the next step would be extending the analysis to Pb-Pb data to gain better understanding of jet modification. Jet analysis in a heavy-ion collision with significant contributions from the underlying event has proved challenging [6]. However, experimental methods have improved in recent years. For the  $j_T$  analysis presented in this thesis the main challenge would be the background subtraction method. Because of anisotropic flow in heavy-ion collisions the background inside the jet cone and a cone perpendicular to it would be different. It's unclear if the perpendicular cone method can be modified or if a completely new approach is required.

It has been shown that in Pb-Pb collisions jets become softer and wider because of medium-induced radiation [6]. On the other hand, the hot medium suppresses gluon jets more than quark jets. This has the opposite effect, narrowing jets, as gluon jets are naturally wider than quark jets [278]. How these different effects combine in  $j_T$  needs to be studied.

# Appendices

# Appendix A

## Commonly Used Abbreviations

AD	ALICE Diffractive detector
AGS	Alternating Gradient Synchrotron
ALICE	A Large Ion Collider Experiment
APD	Avalanche Photo Diodes
ATLAS	A Toroidal LHC Apparatus
BNL	Brookhaven National Laboratory
CERN	European Organisation for Nuclear Research
CMS	Compact Muon Solenoid
CTP	Central Trigger Processor
DAQ	Data Acquisition
DCA	Distance of Closest Approach
DCAL	Di-jet calorimeter
DESY	Deutsches Elektronen-Synchrotron (German Electron Synchrotron)
DGLAP	Dokshitzer-Gribov-Lipatov-Altarelli-Parisi
EMCal	Electromagnetic Calorimeter
FIT	Fast Interaction Trigger
FMD	Forward Multiplicity Detector
GEM	Gas Electron Multiplier
GMC	Glauber Monte Carlo
HMPID	High Momentum Particle Identification
ITS	Inner Tracking System
L0	Level-0 trigger

L1	Level-1 trigger
LBNL	Lawrence Berkeley National Laboratory
LHC	Large Hadron Collider
LHCb	LHC beauty
LPM	Landau-Pomeranchuk- Migdal
LS2	Long Shutdown 2
MC	Monte Carlo
NBD	Negative Binomial Distribution
PDF	Parton Distribution Function
PHENIX	Pioneering High Energy Nuclear Interaction eXperiment
PID	Particle Identification
pQCD	Perturbative QCD
QA	Quality Assurance
QCD	Quantum ChromoDynamics
QED	Quantum ElectroDynamics
QGP	Quark-Gluon Plasma
RF	Radio Frequency
RHIC	Relativistic Heavy Ion Collider
RMS	Root Mean Square
SDD	Silicon Drift Detector
SHINE	SPS Heavy-Ion and Neutrino Experiment
SLAC	Stanford Linear Accelerator Center
SM	Super module
SMOG	System for Measuring Overlap with Gas
SPD	Silicon Pixel Detector
SPS	Super Proton Synchrotron
SSD	Silicon Strip Detector
SVD	Singular Value Decomposition
TOF	Time-of-Flight detector
TOTEM	TOTal Elastic and diffractive cross section Measurement
TPC	Time Projection Chamber
UE	Underlying Event
ZDC	Zero Degree Calorimeter

## Appendix B

### Additional graphs

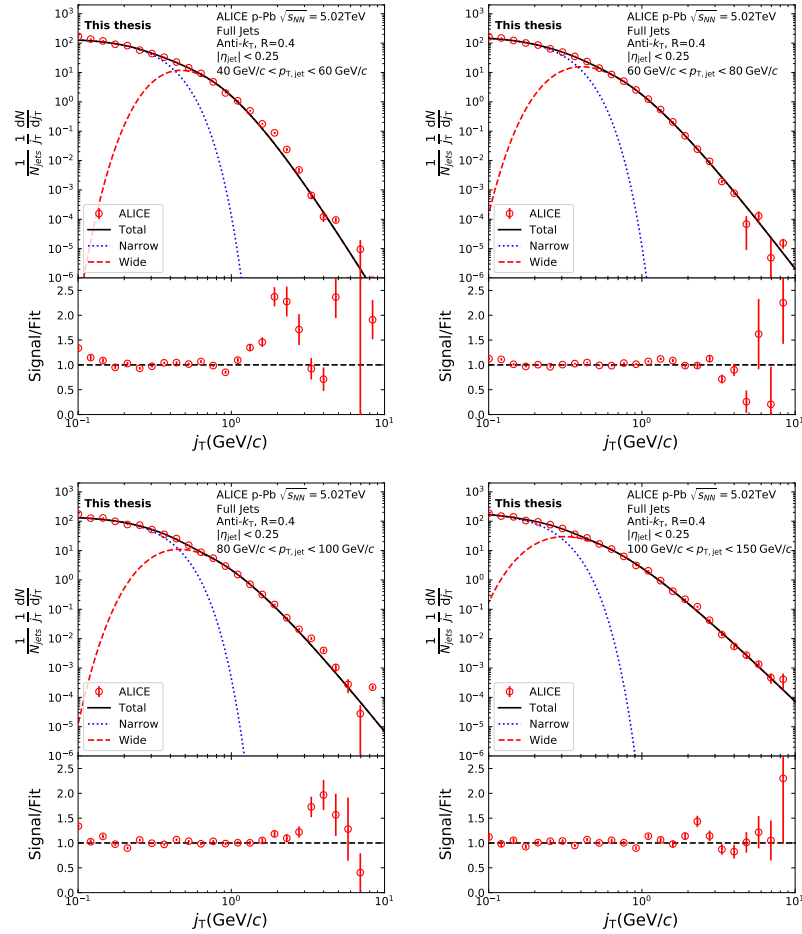


Figure B.1:  $j_T$  signal fits in different jet  $p_T$  bins

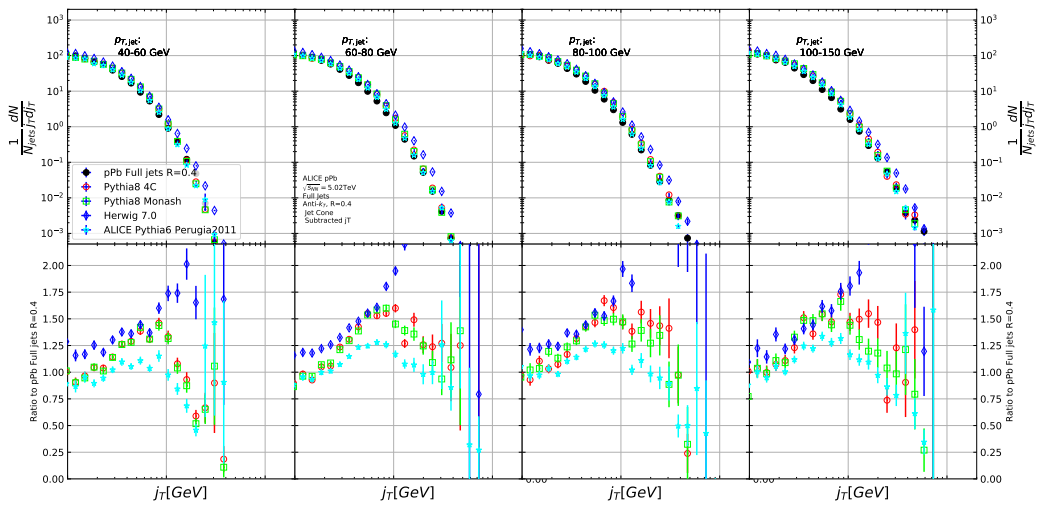


Figure B.2: Figure shows comparisons of  $j_T$  signals between ALICE data and various Monte Carlo simulations.

# Bibliography

- [1] D. J. Gross and F. Wilczek, “Asymptotically free gauge theories. i,” *Physical Review D* **8** no. 10, (1973) 3633.
- [2] **Particle Data Group** Collaboration, M. Tanabashi *et al.*, “Review of Particle Physics,” *Phys. Rev.* **D98** no. 3, (2018) 030001.
- [3] M. L. Perl, E. R. Lee, and D. Loomba, “A Brief review of the search for isolatable fractional charge elementary particles,” *Mod. Phys. Lett.* **A19** (2004) 2595–2610.
- [4] E. Shuryak, “Quantum chromodynamics and the theory of superdense matter,” *Phys. Reps.* **61** (1980) 71.
- [5] D. H. Perkins, *Introduction to high energy physics*. Cambridge University Press, 1982.
- [6] M. Connors, C. Nattrass, R. Reed, and S. Salur, “Jet measurements in heavy ion physics,” *Rev. Mod. Phys.* **90** (2018) 025005, [arXiv:1705.01974 \[nucl-ex\]](https://arxiv.org/abs/1705.01974).
- [7] J. L. Nagle and W. A. Zajc, “Small System Collectivity in Relativistic Hadronic and Nuclear Collisions,” *Ann. Rev. Nucl. Part. Sci.* **68** (2018) 211–235, [arXiv:1801.03477 \[nucl-ex\]](https://arxiv.org/abs/1801.03477).
- [8] E. S., “Entwurf einer verallgemeinerten relativitätstheorie und einer theorie der gravitation,” *Monatshefte für Mathematik und Physik* **26** no. 1, (Dec, 1915) A38–A38. <https://doi.org/10.1007/BF01999515>.
- [9] P. A. M. Dirac and N. H. D. Bohr, “The quantum theory of the emission and absorption of radiation,” *Proceedings of the Royal Society of London. Series A, Containing Papers of a Mathematical and Physical Character* **114** no. 767, (1927) 243–265,  
<https://royalsocietypublishing.org/doi/pdf/10.1098/rspa.1927.0039>.  
<https://royalsocietypublishing.org/doi/abs/10.1098/rspa.1927.0039>.

- [10] S. Tomonaga, “On a relativistically invariant formulation of the quantum theory of wave fields,” *Prog. Theor. Phys.* **1** (1946) 27–42.
- [11] J. S. Schwinger, “Quantum electrodynamics. 2. Vacuum polarization and selfenergy,” *Phys. Rev.* **75** (1948) 651. [,59(1948)].
- [12] J. S. Schwinger, “Quantum electrodynamics. I A covariant formulation,” *Phys. Rev.* **74** (1948) 1439. [,36(1948)].
- [13] R. P. Feynman, “Relativistic cutoff for quantum electrodynamics,” *Phys. Rev.* **74** (1948) 1430–1438.
- [14] M. L. Krauss, *The Greatest Story Ever Told—So Far: Why Are We Here?* Simon & Schuster, 2017.
- [15] S. L. Glashow, J. Iliopoulos, and L. Maiani, “Weak Interactions with Lepton-Hadron Symmetry,” *Phys. Rev.* **D2** (1970) 1285–1292.
- [16] A. Salam and J. C. Ward, “Electromagnetic and weak interactions,” *Phys. Lett.* **13** (1964) 168–171.
- [17] S. Weinberg, “A Model of Leptons,” *Phys. Rev. Lett.* **19** (1967) 1264–1266.
- [18] G. P. S. Occhialini and C. F. Powell, “Nuclear disintegration produced by slow charged particles of small mass,.” [Nature159,186(1947)].
- [19] C. M. G. Lattes, G. P. S. Occhialini, and C. F. Powell, “Observations on the Tracks of Slow Mesons in Photographic Emulsions. 1,” *Nature* **160** (1947) 453–456. [,99(1947)].
- [20] R. Bjorklund, W. Crandall, B. J. Moyer, and H. York, “High energy photons from proton-nucleon collisions,” *Phys. Review* **77** (1950) 213–218.
- [21] O. Chamberlain, E. Segre, C. Wiegand, and T. Ypsilantis, “Observation of Anti-protons,” *Phys. Rev.* **100** (1955) 947–950.
- [22] B. Cork, G. R. Lambertson, O. Piccioni, and W. A. Wenzel, “Anti-neutrons Produced From Anti-protons in Charge Exchange Collisions,” *Phys. Rev.* **104** (1957) 1193–1197.
- [23] L. W. Alvarez, P. Eberhard, M. L. Good, W. Graziano, H. K. Ticho, and S. G. Wojcicki, “Neutral Cascade Hyperon Event,” *Phys. Rev. Lett.* **2** (1959) 215–219.

- [24] R. Armenteros, K. Barker, C. Butler, A. Cachon, and C. York, “Lvi. the properties of charged v-particles,” *The London, Edinburgh, and Dublin Philosophical Magazine and Journal of Science* **43** no. 341, (1952) 597–611, <https://doi.org/10.1080/14786440608520216>.  
<https://doi.org/10.1080/14786440608520216>.
- [25] A. Bonetti, R. L. Setti, M. Panetti, and G. Tomasini, “On the existence of unstable charged particles of hyperprotonic mass,” *Il Nuovo Cimento (1943-1954)* **10** no. 12, (Dec, 1953) 1736–1743.  
<https://doi.org/10.1007/BF02781667>.
- [26] R. Plano, N. Samios, M. Schwartz, and J. Steinberger, “Demostration of the existence of the  $\sigma_0$  hyperon and a measurement of its mass,” *Il Nuovo Cimento (1955-1965)* **5** no. 1, (Jan, 1957) 216–219.  
<https://doi.org/10.1007/BF02812828>.
- [27] W. B. Fowler, R. P. Shutt, A. M. Thorndike, and W. L. Whittemore, “Production of V10 Particles by Negative Pions in Hydrogen,” *Phys. Rev.* **91** no. 5, (1953) 1287.
- [28] W. Heisenberg, “Über den bay der atomkerne,” *Zeitschrift für Physik* **77** (1932) 1–11.
- [29] M. Gell-Mann, “Symmetries of baryons and mesons,” *Phys. Rev.* **125** (1962) 1067.
- [30] V. E. Barnes *et al.*, “Confirmation of the existence of the  $\Omega^-$  hyperon,” *Phys. Lett.* **12** (1964) 134–136.
- [31] M. Gell-Mann, “A schematic model of baryons and mesons,” *Phys. Lett.* **8** (1964) 214.
- [32] G. Zweig, “An SU(3) model for strong interaction symmetry and its breaking. Version 2,” in *DEVELOPMENTS IN THE QUARK THEORY OF HADRONS. VOL. 1. 1964 - 1978*, D. Lichtenberg and S. P. Rosen, eds., pp. 22–101. 1964.
- [33] O. Greenberg, “Spin and unitary spin independence in a paraquark model of baryons and mesons,” *Phys. Rev. Lett.* **13** (1964) 598–602.
- [34] H. Fritzsch and M. Gell-Mann, “Current algebra: Quarks and what else?,” *eConf* **C720906V2** (1972) 135–165, [arXiv:hep-ph/0208010 \[hep-ph\]](https://arxiv.org/abs/hep-ph/0208010).

- [35] **Crystal Ball Collaboration** Collaboration, D. Williams *et al.*, “Formation of the Pseudoscalars  $\pi^0$ ,  $\eta$  and  $\eta'$  in the Reaction  $\gamma\gamma \rightarrow \gamma\gamma$ ,” *Phys. Rev.* **D38** (1988) 1365.
- [36] W. Krolikowski, “Vector Gluon Dominance and Rising Drell Ratio for e- e+ Annihilation,” *Nuovo Cim.* **A27** (1975) 194.
- [37] **LHCb** Collaboration, R. Aaij *et al.*, “Observation of a narrow pentaquark state,  $P_c(4312)^+$ , and of two-peak structure of the  $P_c(4450)^+$ ,” [arXiv:1904.03947 \[hep-ex\]](https://arxiv.org/abs/1904.03947).
- [38] E. D. Bloom *et al.*, “High-Energy Inelastic e p Scattering at 6-Degrees and 10-Degrees,” *Phys. Rev. Lett.* **23** (1969) 930–934.
- [39] M. Breidenbach, J. I. Friedman, H. W. Kendall, E. D. Bloom, D. H. Coward, H. C. DeStaebler, J. Drees, L. W. Mo, and R. E. Taylor, “Observed Behavior of Highly Inelastic electron-Proton Scattering,” *Phys. Rev. Lett.* **23** (1969) 935–939.
- [40] “The nobel prize in physics 1990.” <https://www.nobelprize.org/prizes/physics/1990/summary/>. Accessed: Mon. 8 Apr 2019.
- [41] J. D. Bjorken, “Asymptotic Sum Rules at Infinite Momentum,” *Phys. Rev.* **179** (1969) 1547–1553.
- [42] J. D. Bjorken and E. A. Paschos, “Inelastic Electron Proton and gamma Proton Scattering, and the Structure of the Nucleon,” *Phys. Rev.* **185** (1969) 1975–1982.
- [43] R. P. Feynman, “Very high-energy collisions of hadrons,” *Phys. Rev. Lett.* **23** (1969) 1415–1417. [,494(1969)].
- [44] D. J. Gross and F. Wilczek, “Ultraviolet behavior of non-abelian gauge theories,” *Physical Review Letters* **30** no. 26, (1973) 1343–1346.
- [45] H. D. Politzer, “Reliable perturbative results for strong interactions?,” *Physical Review Letters* **30** no. 26, (1973) 1346–1349.
- [46] D. J. Gross and F. Wilczek, “Asymptotically free gauge theories. ii,” *Physical Review D* **9** no. 4, (1974) 980.
- [47] H. Georgi and H. D. Politzer, “Electroproduction scaling in an asymptotically free theory of strong interactions,” *Physical Review D* **9** no. 2, (1974) 416.

- [48] “The nobel prize in physics 2004.”  
<https://www.nobelprize.org/prizes/physics/2004/summary/>. Accessed: Mon. 8 Apr 2019.
- [49] H. Fritzsch, M. Gell-Mann, and H. Leutwyler, “Advantages of the color octet gluon picture,” *Physics Letters B* **47** no. 4, (1973) 365–368.
- [50] **SLAC-SP-017** Collaboration, J. E. Augustin *et al.*, “Discovery of a Narrow Resonance in  $e^+e^-$  Annihilation,” *Phys. Rev. Lett.* **33** (1974) 1406–1408. [Adv. Exp. Phys.5,141(1976)].
- [51] **E598** Collaboration, J. J. Aubert *et al.*, “Experimental Observation of a Heavy Particle  $J$ ,” *Phys. Rev. Lett.* **33** (1974) 1404–1406.
- [52] C. Bacci *et al.*, “Preliminary Result of Frascati (ADONE) on the Nature of a New 3.1-GeV Particle Produced in e+ e- Annihilation,” *Phys. Rev. Lett.* **33** (1974) 1408. [Erratum: Phys. Rev. Lett.33,1649(1974)].
- [53] “The nobel prize in physics 1976.”  
<https://www.nobelprize.org/prizes/physics/1976/summary/>. Accessed: Mon. 8 Apr 2019.
- [54] J. D. Bjorken and S. L. Glashow, “Elementary Particles and SU(4),” *Phys. Lett.* **11** (1964) 255–257.
- [55] I. Flegel and P. Söding, “Twenty-five years of gluons,” *CERN courier* (2004) . <http://cerncourier.com/cws/article/cern/29201>.
- [56] **TASSO** Collaboration, R. Brandelik *et al.*, “Evidence for Planar Events in e+ e- Annihilation at High-Energies,” *Phys. Lett.* **86B** (1979) 243–249.
- [57] J. K. L. MacDonald, “Successive approximations by the rayleigh-ritz variation method,” *Phys. Rev.* **43** (May, 1933) 830–833.  
<http://link.aps.org/doi/10.1103/PhysRev.43.830>.
- [58] C. Berger *et al.*, “Evidence for gluon bremsstrahlung in e+e annihilations at high energies,” *Physics Letters B* **86** no. 3–4, (1979) 418 – 425. <http://www.sciencedirect.com/science/article/pii/0370269379908694>.
- [59] M. Kobayashi and T. Maskawa, “CP Violation in the Renormalizable Theory of Weak Interaction,” *Prog. Theor. Phys.* **49** (1973) 652–657.
- [60] “The nobel prize in physics 2008.”  
<https://www.nobelprize.org/prizes/physics/2008/summary/>. Accessed: Mon. 8 Apr 2019.

- [61] S. W. Herb *et al.*, “Observation of a Dimuon Resonance at 9.5-GeV in 400-GeV Proton-Nucleus Collisions,” *Phys. Rev. Lett.* **39** (1977) 252–255.
- [62] **CDF** Collaboration, F. Abe *et al.*, “Observation of top quark production in  $\bar{p}p$  collisions,” *Phys. Rev. Lett.* **74** (1995) 2626–2631, [arXiv:hep-ex/9503002 \[hep-ex\]](https://arxiv.org/abs/hep-ex/9503002).
- [63] **D0** Collaboration, S. Abachi *et al.*, “Search for high mass top quark production in  $p\bar{p}$  collisions at  $\sqrt{s} = 1.8$  TeV,” *Phys. Rev. Lett.* **74** (1995) 2422–2426, [arXiv:hep-ex/9411001 \[hep-ex\]](https://arxiv.org/abs/hep-ex/9411001).
- [64] J. Collins and M. Perry, “Superdense matter: Neutrons or asymptotically free quarks?,” *Phys. rev. Lett.* **34** (1975) 1353.
- [65] P. Kovtun, D. Son, and A. Starinets, “Viscosity in strongly interacting quantum field theories from black hole physics,” *Phys. Rev. Lett.* **94** (2005) 111601, [arXiv:hep-th/0405231 \[hep-th\]](https://arxiv.org/abs/hep-th/0405231).
- [66] R. A. Lacey, N. N. Ajitanand, J. M. Alexander, P. Chung, W. G. Holzmann, M. Issah, A. Taranenko, P. Danielewicz, and H. Stöcker, “Has the qcd critical point been signaled by observations at the bnl relativistic heavy ion collider?,” *Phys. Rev. Lett.* **98** (Mar, 2007) 092301. <http://link.aps.org/doi/10.1103/PhysRevLett.98.092301>.
- [67] E. Lofgren, *ACCELERATOR DIVISION ANNUAL REPORTS, 1 JULY 1972 12/31/1974*. Oct, 1975. <http://www.osti.gov/scitech/servlets/purl/937059>.
- [68] A. Kovalenko, A. Baldin, A. Malakhov, *et al.*, “Status of the nuclotron,” in *Proceedings of EPAC*, vol. 94, pp. 161–164. 1994.
- [69] I. Vitev and M. Gyulassy, “High  $p_T$  tomography of  $d + \text{Au}$  and  $\text{Au}+\text{Au}$  at SPS, RHIC, and LHC,” *Phys. Rev. Lett.* **89** (2002) 252301, [arXiv:hep-ph/0209161 \[hep-ph\]](https://arxiv.org/abs/hep-ph/0209161).
- [70] D. S. Barton, “Heavy ion program at bnl: Ags, rhic,” in *Proc. 1987 Particle Accelerator Conference, Washington, D.C., March, 1987*. 1987.
- [71] “New state of matter created at cern.” [Https://home.cern/news/press-release/cern/new-state-matter-created-cern](https://home.cern/news/press-release/cern/new-state-matter-created-cern). Accessed: Sat. 6 Apr 2019.
- [72] **NA61/SHINE** Collaboration, K. Grebieszkow, “Highlights from the NA61/SHINE experiment at the CERN SPS,” *PoS CPOD2013* (2013) 004.

- [73] **PHENIX Collaboration** Collaboration, K. Adcox *et al.*, “Formation of dense partonic matter in relativistic nucleus-nucleus collisions at RHIC: Experimental evaluation by the PHENIX collaboration,” *Nucl.Phys.* **A757** (2005) 184–283, [arXiv:nucl-ex/0410003](https://arxiv.org/abs/nucl-ex/0410003) [nucl-ex].
- [74] **STAR Collaboration** Collaboration, J. Adams *et al.*, “Experimental and theoretical challenges in the search for the quark gluon plasma: The STAR Collaboration’s critical assessment of the evidence from RHIC collisions,” *Nucl.Phys.* **A757** (2005) 102–183, [arXiv:nucl-ex/0501009](https://arxiv.org/abs/nucl-ex/0501009) [nucl-ex].
- [75] **BRAHMS Collaboration** Collaboration, I. Arsene *et al.*, “Quark gluon plasma and color glass condensate at RHIC? The Perspective from the BRAHMS experiment,” *Nucl.Phys.* **A757** (2005) 1–27, [arXiv:nucl-ex/0410020](https://arxiv.org/abs/nucl-ex/0410020) [nucl-ex].
- [76] B. Back, M. Baker, M. Ballintijn, D. Barton, B. Becker, *et al.*, “The PHOBOS perspective on discoveries at RHIC,” *Nucl.Phys.* **A757** (2005) 28–101, [arXiv:nucl-ex/0410022](https://arxiv.org/abs/nucl-ex/0410022) [nucl-ex].
- [77] **LHCb** Collaboration, E. Maurice, “Fixed-target physics at LHCb,” in *5th Large Hadron Collider Physics Conference (LHCP 2017) Shanghai, China, May 15-20, 2017*. 2017. [arXiv:1708.05184](https://arxiv.org/abs/1708.05184) [hep-ex].
- [78] S. A. Voloshin, A. M. Poskanzer, and R. Snellings, “Collective phenomena in non-central nuclear collisions,” [arXiv:0809.2949](https://arxiv.org/abs/0809.2949) [nucl-ex].
- [79] **ALICE Collaboration** Collaboration, “Centrality determination of pb-pb collisions at  $\sqrt{s_{NN}} = 2.76$  tev with alice,” *Phys. Rev. C* **88** (Oct, 2013) 044909. <http://link.aps.org/doi/10.1103/PhysRevC.88.044909>.
- [80] M. L. Miller, K. Reygers, S. J. Sanders, and P. Steinberg, “Glauber modeling in high energy nuclear collisions,” *Ann.Rev.Nucl.Part.Sci.* **57** (2007) 205–243, [arXiv:nucl-ex/0701025](https://arxiv.org/abs/nucl-ex/0701025) [nucl-ex].
- [81] R. Glauber, *Lectures in Theoretical Physics*. Interscience Publishers, Inc., 1959.
- [82] A. Białlas, M. Błeszyński, and W. Czyż, “Multiplicity distributions in nucleus-nucleus collisions at high energies,” *Nuclear Physics B* **111** no. 3, (1976) 461 – 476. <http://www.sciencedirect.com/science/article/pii/0550321376903291>.
- [83] H. De Vries, C. W. De Jager, and C. De Vries, “Nuclear charge and magnetization density distribution parameters from elastic electron scattering,” *Atom. Data Nucl. Data Tabl.* **36** (1987) 495–536.

- [84] **ALICE** Collaboration, B. Abelev *et al.*, “Centrality determination of Pb-Pb collisions at  $\sqrt{s_{NN}} = 2.76$  TeV with ALICE,” *Phys. Rev.* **C88** no. 4, (2013) 044909, [arXiv:1301.4361 \[nucl-ex\]](https://arxiv.org/abs/1301.4361).
- [85] **PHENIX** Collaboration Collaboration, S. Afanasiev *et al.*, “High-pT pi0 Production with Respect to the Reaction Plane in Au + Au Collisions at  $s(NN)^{**}(1/2) = 200$ -GeV,” *Phys. Rev.* **C80** (2009) 054907, [arXiv:0903.4886 \[nucl-ex\]](https://arxiv.org/abs/0903.4886).
- [86] D. Kharzeev, E. Levin, and M. Nardi, “Color glass condensate at the LHC: Hadron multiplicities in pp, pA and AA collisions,” *Nucl. Phys.* **A747** (2005) 609–629, [arXiv:hep-ph/0408050 \[hep-ph\]](https://arxiv.org/abs/hep-ph/0408050).
- [87] W.-T. Deng, X.-N. Wang, and R. Xu, “Hadron production in p+p, p+Pb, and Pb+Pb collisions with the HIJING 2.0 model at energies available at the CERN Large Hadron Collider,” *Phys. Rev.* **C83** (2011) 014915, [arXiv:1008.1841 \[hep-ph\]](https://arxiv.org/abs/1008.1841).
- [88] **TOTEM** Collaboration, G. Antchev *et al.*, “First measurement of elastic, inelastic and total cross-section at  $\sqrt{s} = 13$  TeV by TOTEM and overview of cross-section data at LHC energies,” *Eur. Phys. J.* **C79** no. 2, (2019) 103, [arXiv:1712.06153 \[hep-ex\]](https://arxiv.org/abs/1712.06153).
- [89] B. Alver, M. Baker, C. Loizides, and P. Steinberg, “The PHOBOS Glauber Monte Carlo,” [arXiv:0805.4411 \[nucl-ex\]](https://arxiv.org/abs/0805.4411).
- [90] P. Romatschke, “New Developments in Relativistic Viscous Hydrodynamics,” *Int.J.Mod.Phys.* **E19** (2010) 1–53, [arXiv:0902.3663 \[hep-ph\]](https://arxiv.org/abs/0902.3663).
- [91] **ALICE** Collaboration Collaboration, K. A. *et al.*, “Centrality dependence of the charged-particle multiplicity density at midrapidity in pb-pb collisions at  $\sqrt{s_{NN}} = 2.76$  TeV,” *Phys. Rev. Lett.* **106** (Jan, 2011) 032301. <https://link.aps.org/doi/10.1103/PhysRevLett.106.032301>.
- [92] J.-Y. Ollitrault, “Anisotropy as a signature of transverse collective flow,” *Phys. Rev. D* **46** (Jul, 1992) 229–245.  
[http://link.aps.org/doi/10.1103/PhysRevD.46.229](https://link.aps.org/doi/10.1103/PhysRevD.46.229).
- [93] J.-Y. Ollitrault, “Determination of the reaction plane in ultrarelativistic nuclear collisions,” *Phys. Rev. D* **48** (1993) 1132–1139, [arXiv:hep-ph/9303247 \[hep-ph\]](https://arxiv.org/abs/hep-ph/9303247).

- [94] U. Heinz and P. Kolb, “Early thermalization at rhic,” *Nucl. Phys.* **A702** (2002) 269.
- [95] S. Voloshin and Y. Zhang, “Flow study in relativistic nuclear collisions by Fourier expansion of Azimuthal particle distributions,” *Z.Phys.* **C70** (1996) 665–672, [arXiv:hep-ph/9407282 \[hep-ph\]](https://arxiv.org/abs/hep-ph/9407282).
- [96] A. P. Mishra, R. K. Mohapatra, P. Saumia, and A. M. Srivastava, “Super-horizon fluctuations and acoustic oscillations in relativistic heavy-ion collisions,” *Phys.Rev.* **C77** (2008) 064902, [arXiv:0711.1323 \[hep-ph\]](https://arxiv.org/abs/0711.1323).
- [97] B. Alver and G. Roland, “Collision geometry fluctuations and triangular flow in heavy-ion collisions,” *Phys.Rev.* **C81** (2010) 054905, [arXiv:1003.0194 \[nucl-th\]](https://arxiv.org/abs/1003.0194).
- [98] A. Mocsy and P. Sorensen, “The Sound of the Little Bangs,” [arXiv:1008.3381 \[hep-ph\]](https://arxiv.org/abs/1008.3381).
- [99] T. Abbott *et al.*, “Azimuthal asymmetries of particles emitted in relativistic heavy-ion collisions,” *Phys. Rev. Lett.* **70** (Mar, 1993) 1393–1396. <http://link.aps.org/doi/10.1103/PhysRevLett.70.1393>.
- [100] B. Schenke, S. Jeon, and C. Gale, “Anisotropic flow in  $\sqrt{s} = 2.76$  TeV Pb+Pb collisions at the LHC,” *Phys.Lett.* **B702** (2011) 59–63, [arXiv:1102.0575 \[hep-ph\]](https://arxiv.org/abs/1102.0575).
- [101] K. A. *et al.* [ALICE Collaboration], “Higher harmonic anisotropic flow measurements of charged particles in pb-pb collisions at  $\sqrt{s_{NN}} = 2.76$  TeV,” *Phys. Rev. Lett.* **107** (2011) . 032301.
- [102] K. Aamodt *et al.*, “Harmonic decomposition of two particle angular correlations in pb–pb collisions at,” *Physics Letters B* **708** no. 3–5, (2012) 249 – 264. <http://www.sciencedirect.com/science/article/pii/S0370269312001013>.
- [103] L. LD, “On the multiparticle production in high-energy collisions,” *Izv. Akad. Nauk Ser. Fiz.* **17** (1953) 51.
- [104] J. D. Bjorken, “Highly relativistic nucleus-nucleus collisions: The central rapidity region,” *Phys. Rev. D* **27** (Jan, 1983) 140–151. [https://link.aps.org/doi/10.1103/PhysRevD.27.140](http://link.aps.org/doi/10.1103/PhysRevD.27.140).

- [105] G. Baym, B. L. Friman, J. P. Blaizot, M. Soyeur, and W. Czyz, “Hydrodynamics of Ultrarelativistic Heavy Ion Collisions,” *Nucl. Phys.* **A407** (1983) 541–570.
- [106] H. von Gersdorff, L. McLerran, M. Kataja, and P. V. Ruuskanen, “Studies of the hydrodynamic evolution of matter produced in fluctuations in  $p^-p$  collisions and in ultrarelativistic nuclear collisions,” *Phys. Rev. D* **34** (Aug, 1986) 794–810.  
<https://link.aps.org/doi/10.1103/PhysRevD.34.794>.
- [107] H. Niemi, K. J. Eskola, and R. Paatelainen, “Event-by-event fluctuations in a perturbative QCD + saturation + hydrodynamics model: Determining QCD matter shear viscosity in ultrarelativistic heavy-ion collisions,” *Phys. Rev.* **C93** no. 2, (2016) 024907, [arXiv:1505.02677 \[hep-ph\]](https://arxiv.org/abs/1505.02677).
- [108] R. Paatelainen, K. J. Eskola, H. Holopainen, and K. Tuominen, “Multiplicities and  $p_T$  spectra in ultrarelativistic heavy ion collisions from a next-to-leading order improved perturbative QCD + saturation + hydrodynamics model,” *Phys. Rev.* **C87** no. 4, (2013) 044904, [arXiv:1211.0461 \[hep-ph\]](https://arxiv.org/abs/1211.0461).
- [109] R. Paatelainen, K. J. Eskola, H. Niemi, and K. Tuominen, “Fluid dynamics with saturated minijet initial conditions in ultrarelativistic heavy-ion collisions,” *Phys. Lett.* **B731** (2014) 126–130, [arXiv:1310.3105 \[hep-ph\]](https://arxiv.org/abs/1310.3105).
- [110] **ALICE** Collaboration, J. Adam *et al.*, “Correlated event-by-event fluctuations of flow harmonics in Pb-Pb collisions at  $\sqrt{s_{\text{NN}}} = 2.76 \text{ TeV}$ ,” *Phys. Rev. Lett.* **117** (2016) 182301, [arXiv:1604.07663 \[nucl-ex\]](https://arxiv.org/abs/1604.07663).
- [111] J. E. Bernhard, J. S. Moreland, S. A. Bass, J. Liu, and U. Heinz, “Applying bayesian parameter estimation to relativistic heavy-ion collisions: Simultaneous characterization of the initial state and quark-gluon plasma medium,” *Phys. Rev. C* **94** (Aug, 2016) 024907.  
<https://link.aps.org/doi/10.1103/PhysRevC.94.024907>.
- [112] **ALICE** Collaboration, S. Acharya *et al.*, “Systematic studies of correlations between different order flow harmonics in Pb-Pb collisions at  $\sqrt{s_{\text{NN}}} = 2.76 \text{ TeV}$ ,” *Phys. Rev.* **C97** no. 2, (2018) 024906, [arXiv:1709.01127 \[nucl-ex\]](https://arxiv.org/abs/1709.01127).
- [113] **ALICE** Collaboration, S. Acharya *et al.*, “Linear and non-linear flow modes in Pb-Pb collisions at  $\sqrt{s_{\text{NN}}} = 2.76 \text{ TeV}$ ,” *Phys. Lett.* **B773** (2017) 68–80, [arXiv:1705.04377 \[nucl-ex\]](https://arxiv.org/abs/1705.04377).

- [114] A. Metz and A. Vossen, “Parton Fragmentation Functions,” *Prog. Part. Nucl. Phys.* **91** (2016) 136–202, [arXiv:1607.02521 \[hep-ex\]](#).
- [115] R. Placakyte, “Parton Distribution Functions,” in *Proceedings, 31st International Conference on Physics in collisions (PIC 2011): Vancouver, Canada, August 28-September 1, 2011.* 2011. [arXiv:1111.5452 \[hep-ph\]](#).
- [116] V. N. Gribov and L. N. Lipatov, “Deep inelastic e p scattering in perturbation theory,” *Sov. J. Nucl. Phys.* **15** (1972) 438–450. [*Yad. Fiz.* **15**, 781(1972)].
- [117] G. Altarelli and G. Parisi, “Asymptotic Freedom in Parton Language,” *Nucl. Phys.* **B126** (1977) 298–318.
- [118] Y. L. Dokshitzer, “Calculation of the Structure Functions for Deep Inelastic Scattering and e+ e- Annihilation by Perturbation Theory in Quantum Chromodynamics.,” *Sov. Phys. JETP* **46** (1977) 641–653. [*Zh. Eksp. Teor. Fiz.* **73**, 1216(1977)].
- [119] J. Pumplin, D. R. Stump, J. Huston, H. L. Lai, P. M. Nadolsky, and W. K. Tung, “New generation of parton distributions with uncertainties from global QCD analysis,” *JHEP* **07** (2002) 012, [arXiv:hep-ph/0201195 \[hep-ph\]](#).
- [120] **ZEUS, H1** Collaboration, A. M. Cooper-Sarkar, “PDF Fits at HERA,” *PoS EPS-HEP2011* (2011) 320, [arXiv:1112.2107 \[hep-ph\]](#).
- [121] J. Butterworth *et al.*, “PDF4LHC recommendations for LHC Run II,” *J. Phys.* **G43** (2016) 023001, [arXiv:1510.03865 \[hep-ph\]](#).
- [122] T. Sjöstrand and P. Z. Skands, “Transverse-momentum-ordered showers and interleaved multiple interactions,” *Eur. Phys. J.* **C39** (2005) 129–154, [arXiv:hep-ph/0408302 \[hep-ph\]](#).
- [123] T. Sjöstrand, S. Ask, J. R. Christiansen, R. Corke, N. Desai, P. Ilten, S. Mrenna, S. Prestel, C. O. Rasmussen, and P. Z. Skands, “An Introduction to PYTHIA 8.2,” *Comput. Phys. Commun.* **191** (2015) 159–177, [arXiv:1410.3012 \[hep-ph\]](#).
- [124] M. Bahr *et al.*, “Herwig++ Physics and Manual,” *Eur. Phys. J.* **C58** (2008) 639–707, [arXiv:0803.0883 \[hep-ph\]](#).
- [125] A. Buckley *et al.*, “General-purpose event generators for LHC physics,” *Phys. Rept.* **504** (2011) 145–233, [arXiv:1101.2599 \[hep-ph\]](#).

- [126] Y. L. Dokshitzer, V. A. Khoze, A. H. Müller, and S. I. Troian, *Basics of Perturbative QCD*. Editions Frontières, Gif-sur-Yvette, France, 1991.
- [127] Y. I. Azimov, Y. L. Dokshitzer, V. A. Khoze, and S. I. Trovan, “Similarity of parton and hadron spectra in qcd jets,” *Zeitschrift für Physik C Particles and Fields* **27** no. 1, (Mar, 1985) 65–72.  
<https://doi.org/10.1007/BF01642482>.
- [128] B. Andersson, G. Gustafson, G. Ingelman, and T. Sjöstrand, “Parton fragmentation and string dynamics,” *Physics Reports* **97** no. 2, (1983) 31 – 145. <http://www.sciencedirect.com/science/article/pii/0370157383900807>.
- [129] **ALICE Collaboration** Collaboration, K. Aamodt *et al.*, “Suppression of Charged Particle Production at Large Transverse Momentum in Central Pb–Pb Collisions at  $\sqrt{s_{NN}} = 2.76$  TeV,” *Phys.Lett.* **B696** (2011) 30–39, [arXiv:1012.1004 \[nucl-ex\]](https://arxiv.org/abs/1012.1004).
- [130] **WA98 Collaboration** Collaboration, M. Aggarwal *et al.*, “Transverse mass distributions of neutral pions from Pb-208 induced reactions at 158-A-GeV,” *Eur.Phys.J.* **C23** (2002) 225–236, [arXiv:nucl-ex/0108006 \[nucl-ex\]](https://arxiv.org/abs/nucl-ex/0108006).
- [131] D. G. d’Enterria, “Indications of suppressed high p(T) hadron production in nucleus - nucleus collisions at CERN-SPS,” *Phys.Lett.* **B596** (2004) 32–43, [arXiv:nucl-ex/0403055 \[nucl-ex\]](https://arxiv.org/abs/nucl-ex/0403055).
- [132] **PHENIX Collaboration** Collaboration, A. Adare *et al.*, “Suppression pattern of neutral pions at high transverse momentum in Au + Au collisions at  $s(\text{NN})^{**}(1/2) = 200$ -GeV and constraints on medium transport coefficients,” *Phys.Rev.Lett.* **101** (2008) 232301, [arXiv:0801.4020 \[nucl-ex\]](https://arxiv.org/abs/0801.4020).
- [133] **STAR Collaboration** Collaboration, J. Adams *et al.*, “Transverse momentum and collision energy dependence of high p(T) hadron suppression in Au+Au collisions at ultrarelativistic energies,” *Phys.Rev.Lett.* **91** (2003) 172302, [arXiv:nucl-ex/0305015 \[nucl-ex\]](https://arxiv.org/abs/nucl-ex/0305015).
- [134] **CMS Collaboration** Collaboration, S. Chatrchyan *et al.*, “Study of high-pT charged particle suppression in PbPb compared to  $pp$  collisions at  $\sqrt{s_{NN}} = 2.76$  TeV,” *Eur.Phys.J.* **C72** (2012) 1945, [arXiv:1202.2554 \[nucl-ex\]](https://arxiv.org/abs/1202.2554).

- [135] A. Dainese, C. Loizides, and G. Paic, “Leading-particle suppression in high energy nucleus-nucleus collisions,” *Eur.Phys.J.* **C38** (2005) 461–474, [arXiv:hep-ph/0406201 \[hep-ph\]](#).
- [136] I. Vitev, “Jet tomography,” *J.Phys.* **G30** (2004) S791–S800, [arXiv:hep-ph/0403089 \[hep-ph\]](#).
- [137] C. A. Salgado and U. A. Wiedemann, “Calculating quenching weights,” *Phys.Rev.* **D68** (2003) 014008, [arXiv:hep-ph/0302184 \[hep-ph\]](#).
- [138] N. Armesto, A. Dainese, C. A. Salgado, and U. A. Wiedemann, “Testing the color charge and mass dependence of parton energy loss with heavy-to-light ratios at RHIC and CERN LHC,” *Phys.Rev.* **D71** (2005) 054027, [arXiv:hep-ph/0501225 \[hep-ph\]](#).
- [139] T. Renk, H. Holopainen, R. Paatelainen, and K. J. Eskola, “Systematics of the charged-hadron  $p_T$  spectrum and the nuclear suppression factor in heavy-ion collisions from  $\sqrt{s} = 200$  GeV to  $\sqrt{s} = 2.76$  TeV,” *Phys.Rev.* **C84** (2011) 014906, [arXiv:1103.5308 \[hep-ph\]](#).
- [140] **PHENIX** Collaboration, S. S. Adler *et al.*, “A Detailed Study of High-p(T) Neutral Pion Suppression and Azimuthal Anisotropy in Au+Au Collisions at  $s(\text{NN})^{**}(1/2) = 200$ -GeV,” *Phys. Rev.* **C76** (2007) 034904, [arXiv:nucl-ex/0611007 \[nucl-ex\]](#).
- [141] **PHENIX** Collaboration, A. Adare *et al.*, “Azimuthal anisotropy of  $\pi^0$  and  $\eta$  mesons in Au + Au collisions at  $\sqrt{s_{NN}} = 200$  GeV,” *Phys. Rev.* **C88** no. 6, (2013) 064910, [arXiv:1309.4437 \[nucl-ex\]](#).
- [142] **ALICE** Collaboration, B. Abelev *et al.*, “Anisotropic flow of charged hadrons, pions and (anti-)protons measured at high transverse momentum in Pb-Pb collisions at  $\sqrt{s_{NN}}=2.76$  TeV,” *Phys. Lett.* **B719** (2013) 18–28, [arXiv:1205.5761 \[nucl-ex\]](#).
- [143] **CMS** Collaboration, S. Chatrchyan *et al.*, “Azimuthal anisotropy of charged particles at high transverse momenta in PbPb collisions at  $\sqrt{s_{NN}} = 2.76$  TeV,” *Phys. Rev. Lett.* **109** (2012) 022301, [arXiv:1204.1850 \[nucl-ex\]](#).
- [144] W. H. H. Bethe and, “On the stopping of fast particles and on the creation of positive electrons,” *Proc.Roy.Soc.Lond.* **A146** (1934) .
- [145] L. D. Landau and I. Pomeranchuk, “Limits of applicability of the theory of bremsstrahlung electrons and pair production at high-energies,” *Dokl. Akad. Nauk Ser. Fiz.* **92** (1953) 535–536.

- [146] A. B. Migdal, “Bremsstrahlung and pair production in condensed media at high-energies,” *Phys. Rev.* **103** (1956) 1811–1820.
- [147] R. Baier, Y. L. Dokshitzer, A. H. Mueller, S. Peigne, and D. Schiff, “Radiative energy loss and p(T) broadening of high-energy partons in nuclei,” *Nucl. Phys.* **B484** (1997) 265–282, [arXiv:hep-ph/9608322 \[hep-ph\]](#).
- [148] A. Majumder and M. Van Leeuwen, “The Theory and Phenomenology of Perturbative QCD Based Jet Quenching,” *Prog.Part.Nucl.Phys.* **A66** (2011) 41–92, [arXiv:1002.2206 \[hep-ph\]](#).
- [149] F. Dominguez, C. Marquet, A. Mueller, B. Wu, and B.-W. Xiao, “Comparing energy loss and p-perpendicular - broadening in perturbative QCD with strong coupling N = 4 SYM theory,” *Nucl.Phys.* **A811** (2008) 197–222, [arXiv:0803.3234 \[nucl-th\]](#).
- [150] M. Gyulassy, P. Levai, and I. Vitev, “Jet quenching in thin quark gluon plasmas. 1. Formalism,” *Nucl.Phys.* **B571** (2000) 197–233, [arXiv:hep-ph/9907461 \[hep-ph\]](#).
- [151] U. A. Wiedemann, “Gluon radiation off hard quarks in a nuclear environment: Opacity expansion,” *Nucl.Phys.* **B588** (2000) 303–344, [arXiv:hep-ph/0005129 \[hep-ph\]](#).
- [152] P. B. Arnold, G. D. Moore, and L. G. Yaffe, “Photon emission from quark gluon plasma: Complete leading order results,” *JHEP* **0112** (2001) 009, [arXiv:hep-ph/0111107 \[hep-ph\]](#).
- [153] X.-N. Wang and X.-f. Guo, “Multiple parton scattering in nuclei: Parton energy loss,” *Nucl.Phys.* **A696** (2001) 788–832, [arXiv:hep-ph/0102230 \[hep-ph\]](#).
- [154] T. Sjostrand, S. Mrenna, and P. Z. Skands, “A Brief Introduction to PYTHIA 8.1,” *Comput.Phys.Commun.* **178** (2008) 852–867, [arXiv:0710.3820 \[hep-ph\]](#).
- [155] C. Bierlich, G. Gustafson, L. Lönnblad, and H. Shah, “The Angantyr model for Heavy-Ion Collisions in PYTHIA8,” *JHEP* **10** (2018) 134, [arXiv:1806.10820 \[hep-ph\]](#).
- [156] I. Lokhtin and A. Snigirev, “A Model of jet quenching in ultrarelativistic heavy ion collisions and high-p(T) hadron spectra at RHIC,” *Eur.Phys.J.* **C45** (2006) 211–217, [arXiv:hep-ph/0506189 \[hep-ph\]](#).

- [157] N. Armesto, L. Cunqueiro, and C. A. Salgado, “Monte Carlo for Jet Showers in the Medium,” *Nucl. Phys.* **A830** (2009) 271C–274C, [arXiv:0907.4706 \[hep-ph\]](#).
- [158] K. Zapp, G. Ingelman, J. Rathsman, J. Stachel, and U. A. Wiedemann, “A Monte Carlo Model for ‘Jet Quenching’,” *Eur. Phys. J.* **C60** (2009) 617–632, [arXiv:0804.3568 \[hep-ph\]](#).
- [159] T. Renk, “A Comparison study of medium-modified QCD shower evolution scenarios,” *Phys. Rev.* **C79** (2009) 054906, [arXiv:0901.2818 \[hep-ph\]](#).
- [160] **ALICE** Collaboration, J. Adam *et al.*, “Measurement of jet suppression in central Pb-Pb collisions at  $\sqrt{s_{NN}} = 2.76$  TeV,” *Phys. Lett.* **B746** (2015) 1–14, [arXiv:1502.01689 \[nucl-ex\]](#).
- [161] **ATLAS** Collaboration, G. Aad *et al.*, “Measurements of the Nuclear Modification Factor for Jets in Pb+Pb Collisions at  $\sqrt{s_{NN}} = 2.76$  TeV with the ATLAS Detector,” *Phys. Rev. Lett.* **114** no. 7, (2015) 072302, [arXiv:1411.2357 \[hep-ex\]](#).
- [162] **CMS** Collaboration, V. Khachatryan *et al.*, “Measurement of inclusive jet cross sections in  $pp$  and PbPb collisions at  $\sqrt{s_{NN}} = 2.76$  TeV,” *Phys. Rev.* **C96** no. 1, (2017) 015202, [arXiv:1609.05383 \[nucl-ex\]](#).
- [163] **STAR** Collaboration, L. Adamczyk *et al.*, “Jet-Hadron Correlations in  $\sqrt{s_{NN}} = 200$  GeV  $p + p$  and Central  $Au + Au$  Collisions,” *Phys. Rev. Lett.* **112** no. 12, (2014) 122301, [arXiv:1302.6184 \[nucl-ex\]](#).
- [164] **CMS** Collaboration, V. Khachatryan *et al.*, “Correlations between jets and charged particles in PbPb and pp collisions at  $\sqrt{s_{NN}} = 2.76$  TeV,” *JHEP* **02** (2016) 156, [arXiv:1601.00079 \[nucl-ex\]](#).
- [165] A. Kurkela and U. A. Wiedemann, “Picturing perturbative parton cascades in QCD matter,” *Phys. Lett.* **B740** (2015) 172–178, [arXiv:1407.0293 \[hep-ph\]](#).
- [166] **JETSCAPE** Collaboration, Y. Tachibana *et al.*, “Jet substructure modification in a QGP from a multi-scale description of jet evolution with JETSCAPE,” 2018. [arXiv:1812.06366 \[nucl-th\]](#).
- [167] P. Aurenche and B. G. Zakharov, “Jet color chemistry and anomalous baryon production in  $AA$ -collisions,” *Eur. Phys. J.* **C71** (2011) 1829, [arXiv:1109.6819 \[hep-ph\]](#).

- [168] A. Beraudo, J. G. Milhano, and U. A. Wiedemann, “Medium-induced color flow softens hadronization,” *Phys. Rev.* **C85** (2012) 031901, [arXiv:1109.5025 \[hep-ph\]](#).
- [169] A. Beraudo, J. G. Milhano, and U. A. Wiedemann, “The Contribution of Medium-Modified Color Flow to Jet Quenching,” *JHEP* **07** (2012) 144, [arXiv:1204.4342 \[hep-ph\]](#).
- [170] J. Casalderrey-Solana, Y. Mehtar-Tani, C. A. Salgado, and K. Tywoniuk, “New picture of jet quenching dictated by color coherence,” *Phys. Lett. B* **725** (2013) 357–360, [arXiv:1210.7765 \[hep-ph\]](#).
- [171] F. D’Eramo, M. Lekaveckas, H. Liu, and K. Rajagopal, “Momentum Broadening in Weakly Coupled Quark-Gluon Plasma (with a view to finding the quasiparticles within liquid quark-gluon plasma),” *JHEP* **05** (2013) 031, [arXiv:1211.1922 \[hep-ph\]](#).
- [172] A. Ayala, I. Dominguez, J. Jalilian-Marian, and M. E. Tejeda-Yeomans, “Relating  $\hat{q}$ ,  $\eta/s$  and  $\Delta E$  in an expanding quark-gluon plasma,” *Phys. Rev. C* **94** no. 2, (2016) 024913, [arXiv:1603.09296 \[hep-ph\]](#).
- [173] G. Moliere, “Theorie der Streuung schneller geladener Teilchen I. Einzelstreuung am abgeschirmten Coulomb-Feld,” *Z. Naturforsch. A* **2** (1947) 133.
- [174] CMS Collaboration, S. Chatrchyan *et al.*, “Observation and studies of jet quenching in PbPb collisions at nucleon-nucleon center-of-mass energy = 2.76 TeV,” *Phys. Rev. C* **84** (2011) 024906, [arXiv:1102.1957 \[nucl-ex\]](#).
- [175] C. Aidala *et al.*, “Measurement of long-range angular correlations and azimuthal anisotropies in high-multiplicity  $p+\text{Au}$  collisions at  $\sqrt{s_{NN}} = 200$  GeV,” *Phys. Rev. C* **95** no. 3, (2017) 034910, [arXiv:1609.02894 \[nucl-ex\]](#).
- [176] PHENIX Collaboration, S. S. Adler *et al.*, “Absence of suppression in particle production at large transverse momentum in  $S(\text{NN})^{**}(1/2) = 200\text{-GeV}$   $d + \text{Au}$  collisions,” *Phys. Rev. Lett.* **91** (2003) 072303, [arXiv:nucl-ex/0306021 \[nucl-ex\]](#).
- [177] BRAHMS Collaboration, I. Arsene *et al.*, “Transverse momentum spectra in  $\text{Au}+\text{Au}$  and  $d+\text{Au}$  collisions at  $s^{**}(1/2) = 200\text{-GeV}$  and the pseudorapidity dependence of high  $p(T)$  suppression,” *Phys. Rev. Lett.* **91** (2003) 072305, [arXiv:nucl-ex/0307003 \[nucl-ex\]](#).

- [178] **PHOBOS** Collaboration, B. B. Back *et al.*, “Centrality dependence of charged hadron transverse momentum spectra in d + Au collisions at  $S(NN)^{**1/2} = 200$  GeV,” *Phys. Rev. Lett.* **91** (2003) 072302, [arXiv:nucl-ex/0306025 \[nucl-ex\]](#).
- [179] **STAR** Collaboration, J. Adams *et al.*, “Evidence from d + Au measurements for final state suppression of high p(T) hadrons in Au+Au collisions at RHIC,” *Phys. Rev. Lett.* **91** (2003) 072304, [arXiv:nucl-ex/0306024 \[nucl-ex\]](#).
- [180] **PHENIX** Collaboration, A. Adare *et al.*, “Measurements of elliptic and triangular flow in high-multiplicity  ${}^3\text{He}+\text{Au}$  collisions at  $\sqrt{s_{NN}} = 200$  GeV,” *Phys. Rev. Lett.* **115** no. 14, (2015) 142301, [arXiv:1507.06273 \[nucl-ex\]](#).
- [181] **E735** Collaboration, T. Alexopoulos *et al.*, “Mass identified particle production in  $p\bar{p}$  collisions at  $\sqrt{s} = 300$ -GeV, 540-GeV, 1000-GeV, and 1800-GeV,” *Phys. Rev.* **D48** (1993) 984–997.
- [182] **MiniMax** Collaboration, T. C. Brooks *et al.*, “A Search for disoriented chiral condensate at the Fermilab Tevatron,” *Phys. Rev.* **D61** (2000) 032003, [arXiv:hep-ex/9906026 \[hep-ex\]](#).
- [183] C. Shen, Z. Qiu, and U. Heinz, “Shape and flow fluctuations in ultracentral Pb + Pb collisions at the energies available at the CERN Large Hadron Collider,” *Phys. Rev.* **C92** no. 1, (2015) 014901, [arXiv:1502.04636 \[nucl-th\]](#).
- [184] **PHENIX** Collaboration, A. Adare *et al.*, “Azimuthally anisotropic emission of low-momentum direct photons in Au+Au collisions at  $\sqrt{s_{NN}} = 200$  GeV,” *Phys. Rev.* **C94** no. 6, (2016) 064901, [arXiv:1509.07758 \[nucl-ex\]](#).
- [185] **CMS** Collaboration, V. Khachatryan *et al.*, “Observation of Long-Range Near-Side Angular Correlations in Proton-Proton Collisions at the LHC,” *JHEP* **09** (2010) 091, [arXiv:1009.4122 \[hep-ex\]](#).
- [186] C. A. Salgado and J. P. Wessels, “Proton–Lead Collisions at the CERN LHC,” *Ann. Rev. Nucl. Part. Sci.* **66** (2016) 449–473.
- [187] **ATLAS** Collaboration, G. Aad *et al.*, “Observation of Long-Range Elliptic Azimuthal Anisotropies in  $\sqrt{s} = 13$  and 2.76 TeV  $pp$  Collisions with the ATLAS Detector,” *Phys. Rev. Lett.* **116** no. 17, (2016) 172301, [arXiv:1509.04776 \[hep-ex\]](#).

- [188] **ALICE** Collaboration, S. Acharya *et al.*, “Searches for transverse momentum dependent flow vector fluctuations in Pb-Pb and p-Pb collisions at the LHC,” *JHEP* **09** (2017) 032, [arXiv:1707.05690 \[nucl-ex\]](#).
- [189] C. Shen, J.-F. Paquet, G. S. Denicol, S. Jeon, and C. Gale, “Collectivity and electromagnetic radiation in small systems,” *Phys. Rev.* **C95** no. 1, (2017) 014906, [arXiv:1609.02590 \[nucl-th\]](#).
- [190] H. Niemi and G. S. Denicol, “How large is the Knudsen number reached in fluid dynamical simulations of ultrarelativistic heavy ion collisions?,” [arXiv:1404.7327 \[nucl-th\]](#).
- [191] **PHENIX** Collaboration, C. Aidala *et al.*, “Creation of quark-gluon plasma droplets with three distinct geometries,” *Nature Phys.* **15** no. 3, (2019) 214–220, [arXiv:1805.02973 \[nucl-ex\]](#).
- [192] **CMS** Collaboration, C. Collaboration, “Elliptic flow of charm and strange hadrons in high-multiplicity pPb collisions at  $\sqrt{s_{NN}} = 8.16$  TeV,”
- [193] **CMS** Collaboration, V. Khachatryan *et al.*, “Charged-particle nuclear modification factors in PbPb and pPb collisions at  $\sqrt{s_{NN}} = 5.02$  TeV,” *JHEP* **04** (2017) 039, [arXiv:1611.01664 \[nucl-ex\]](#).
- [194] **ATLAS** Collaboration, G. Aad *et al.*, “Measurement of long-range pseudorapidity correlations and azimuthal harmonics in  $\sqrt{s_{NN}} = 5.02$  TeV proton-lead collisions with the ATLAS detector,” *Phys. Rev.* **C90** no. 4, (2014) 044906, [arXiv:1409.1792 \[hep-ex\]](#).
- [195] X. Zhang and J. Liao, “Jet Quenching and Its Azimuthal Anisotropy in AA and possibly High Multiplicity pA and dA Collisions,” [arXiv:1311.5463 \[nucl-th\]](#).
- [196] C. Park, C. Shen, S. Jeon, and C. Gale, “Rapidity-dependent jet energy loss in small systems with finite-size effects and running coupling,” *Nucl. Part. Phys. Proc.* **289-290** (2017) 289–292, [arXiv:1612.06754 \[nucl-th\]](#).
- [197] K. Tywoniuk, “Is there jet quenching in pPb?,” *Nucl. Phys.* **A926** (2014) 85–91.
- [198] **CMS** Collaboration, A. M. Sirunyan *et al.*, “Azimuthal anisotropy of charged particles with transverse momentum up to 100 GeV/ c in PbPb collisions at  $\sqrt{s_{NN}}=5.02$  TeV,” *Phys. Lett.* **B776** (2018) 195–216, [arXiv:1702.00630 \[hep-ex\]](#).

- [199] **ALICE** Collaboration, J. Adam *et al.*, “Centrality dependence of particle production in p-Pb collisions at  $\sqrt{s_{\text{NN}}} = 5.02$  TeV,” *Phys. Rev.* **C91** no. 6, (2015) 064905, [arXiv:1412.6828 \[nucl-ex\]](https://arxiv.org/abs/1412.6828).
- [200] F. Sikler, “Centrality control of hadron nucleus interactions by detection of slow nucleons,” [arXiv:hep-ph/0304065 \[hep-ph\]](https://arxiv.org/abs/hep-ph/0304065).
- [201] “Cern.” <https://home.cern/>. Accessed: Wed. 17 Apr 2019.
- [202] 2019. <http://cds.cern.ch/record/2197559/>.
- [203] P. M. Watkins, “DISCOVERY OF THE W AND Z BOSONS,” *Contemp. Phys.* **27** (1986) 291–324.
- [204] **COMPASS** Collaboration, O. M. Kouznetsov, “The COMPASS experiment at CERN,” in *Proceedings, 18th International Seminar on High Energy Physics (Quarks 2014): Suzdal, Russia, June 2-8, 2014*. <http://quarks.inr.ac.ru/2014/proceedings/www/p2/Kouznetsov1.pdf>.
- [205] **NA61/SHINE** Collaboration, A. Laszlo, “The NA61/SHINE Experiment at the CERN SPS,” *Nucl. Phys.* **A830** (2009) 559C–562C, [arXiv:0907.4493 \[nucl-ex\]](https://arxiv.org/abs/0907.4493).
- [206] **NA62** **Collaboration** Collaboration, F. Hahn, F. Ambrosino, A. Ceccucci, H. Danielsson, N. Doble, F. Fantechi, A. Kluge, C. Lazzeroni, M. Lenti, G. Ruggiero, M. Sozzi, P. Valente, and R. Wanke, “NA62: Technical Design Document,” Tech. Rep. NA62-10-07, CERN, Geneva, Dec, 2010. <https://cds.cern.ch/record/1404985>.
- [207] **NA63** **Collaboration** Collaboration, R. Mikkelsen, U. Uggerhoj, and T. Wistisen, “Technical Design Report, CERN NA63,” Tech. Rep. CERN-SPSC-2014-033. SPSC-SR-146, CERN, Geneva, Oct, 2014. <https://cds.cern.ch/record/1955391>.
- [208] **AWAKE** Collaboration, S. Döbert, “The Proton Driven Advanced Wake Field Acceleration Experiment (AWAKE) at CERN,”. <https://cds.cern.ch/record/2669231>.
- [209] R. Losito, E. Lafage, and W. Scandale, “The UA9 Experiment at the CERN-SPS,”. <https://cds.cern.ch/record/1223625>.
- [210] **DIRAC** Collaboration, C. P. Schuetz, “The Dirac experiment at CERN,” in *Proceedings, 38th Rencontres de Moriond on QCD and High-Energy Hadronic Interactions: Les Arcs, France, March 22-29, 2003*. 2003. [arXiv:hep-ph/0305121 \[hep-ph\]](https://arxiv.org/abs/hep-ph/0305121).

- [211] E. M. Dunne *et al.*, “Global atmospheric particle formation from cern cloud measurements,” *Science* **354** no. 6316, (2016) 1119–1124.  
<https://science.sciencemag.org/content/354/6316/1119>.
- [212] **n\_TOF** Collaboration, P. M. Milazzo *et al.*, “Neutron Capture Measurements at the n\_TOF Facility,” *AIP Conf. Proc.* **1109** no. 1, (2009) 84.
- [213] “Cern experiments,” 2019. <https://home.cern/science/experiments>.
- [214] O. S. Brüning, P. Collier, P. Lebrun, S. Myers, R. Ostojic, J. Poole, and P. Proudlock, *LHC Design Report*. CERN Yellow Reports: Monographs. CERN, Geneva, 2004. <https://cds.cern.ch/record/782076>.
- [215] L. Evans and P. Bryant, “LHC Machine,” *JINST* **3** (2008) S08001.
- [216] **ALICE** Collaboration, K. Aamodt *et al.*, “The ALICE experiment at the CERN LHC,” *JINST* **3** (2008) S08002.
- [217] **ATLAS** Collaboration, G. Aad *et al.*, “The ATLAS Experiment at the CERN Large Hadron Collider,” *JINST* **3** (2008) S08003.
- [218] **CMS** Collaboration, S. Chatrchyan *et al.*, “The CMS Experiment at the CERN LHC,” *JINST* **3** (2008) S08004.
- [219] **LHCb** Collaboration, A. A. Alves, Jr. *et al.*, “The LHCb Detector at the LHC,” *JINST* **3** (2008) S08005.
- [220] **LHCf** Collaboration, O. Adriani *et al.*, “The LHCf detector at the CERN Large Hadron Collider,” *JINST* **3** (2008) S08006.
- [221] **TOTEM** Collaboration, G. Anelli *et al.*, “The TOTEM experiment at the CERN Large Hadron Collider,” *JINST* **3** (2008) S08007.
- [222] **MoEDAL** Collaboration, B. Acharya *et al.*, “Search for magnetic monopoles with the MoEDAL prototype trapping detector in 8 TeV proton-proton collisions at the LHC,” *JHEP* **08** (2016) 067, [arXiv:1604.06645 \[hep-ex\]](https://arxiv.org/abs/1604.06645).
- [223] **ATLAS** Collaboration, G. Aad *et al.*, “Observation of a new particle in the search for the Standard Model Higgs boson with the ATLAS detector at the LHC,” *Phys. Lett.* **B716** (2012) 1–29, [arXiv:1207.7214 \[hep-ex\]](https://arxiv.org/abs/1207.7214).
- [224] **CMS** Collaboration, S. Chatrchyan *et al.*, “Observation of a new boson at a mass of 125 GeV with the CMS experiment at the LHC,” *Phys. Lett.* **B716** (2012) 30–61, [arXiv:1207.7235 \[hep-ex\]](https://arxiv.org/abs/1207.7235).

- [225] **LHCb** Collaboration, R. Aaij *et al.*, “First Evidence for the Decay  $B_s^0 \rightarrow \mu^+ \mu^-$ ,” *Phys. Rev. Lett.* **110** no. 2, (2013) 021801  
CERN-PH-EP-2012-335, LHCb-PAPER-2012-043, arXiv:1211.2674 [hep-ex].
- [226] **LHCb** Collaboration, R. Aaij *et al.*, “Measurement of the  $B_s^0 \rightarrow \mu^+ \mu^-$  branching fraction and effective lifetime and search for  $B^0 \rightarrow \mu^+ \mu^-$  decays,” *Phys. Rev. Lett.* **118** no. 19, (2017) 191801 CERN-EP-2017-041, LHCb-PAPER-2017-001, arXiv:1703.05747 [hep-ex].
- [227] **ALICE** Collaboration, K. Aamodt *et al.*, “Charged-particle multiplicity density at mid-rapidity in central Pb-Pb collisions at  $\sqrt{s_{NN}} = 2.76$  TeV,” *Phys. Rev. Lett.* **105** (2010) 252301, arXiv:1011.3916 [nucl-ex].
- [228] **ALICE** Collaboration, G. Dellacasa *et al.*, “ALICE: Technical design report of the time projection chamber,” CERN-OPEN-2000-183, CERN-LHCC-2000-001.
- [229] **ALICE** Collaboration, G. Dellacasa *et al.*, “ALICE technical design report of the inner tracking system (ITS),” CERN-LHCC-99-12.
- [230] **ALICE** Collaboration, I. Belikov, “Upgrade of the ALICE Inner Tracking System,” *EPJ Web Conf.* **125** (2016) 01004, arXiv:1607.01171 [physics.ins-det].
- [231] J. Alme *et al.*, “The ALICE TPC, a large 3-dimensional tracking device with fast readout for ultra-high multiplicity events,” *Nucl. Instrum. Meth. A* **622** (2010) 316–367, arXiv:1001.1950 [physics.ins-det].
- [232] for the **ALICE** Collaboration, C. Zampolli, “Particle Identification with the ALICE detector at the LHC,” in *Proceedings, PLHC2012: Physics at the LHC 2012 (PLHC2012): Vancouver, BC, Canada, June 4-9, 2012*. 2012. arXiv:1209.5637 [hep-ex].
- [233] **ALICE Collaboration** Collaboration, P. Cortese, *ALICE transition-radiation detector: Technical Design Report*. Technical Design Report ALICE. CERN, Geneva, 2001.  
<https://cds.cern.ch/record/519145>.
- [234] **ALICE** Collaboration, G. Dellacasa *et al.*, “ALICE technical design report of the time-of-flight system (TOF),” CERN-LHCC-2000-012.
- [235] **ALICE** Collaboration, S. Beole *et al.*, “ALICE technical design report: Detector for high momentum PID,” CERN-LHCC-98-19.

- [236] **ALICE** Collaboration, B. Abelev *et al.*, “Neutral pion and  $\eta$  meson production in proton-proton collisions at  $\sqrt{s} = 0.9$  TeV and  $\sqrt{s} = 7$  TeV,” *Phys. Lett.* **B717** (2012) 162–172, [arXiv:1205.5724 \[hep-ex\]](https://arxiv.org/abs/1205.5724).
- [237] **ALICE** Collaboration, J. Adam *et al.*, “Direct photon production in Pb-Pb collisions at  $\sqrt{s_{\text{NN}}} = 2.76$  TeV,” *Phys. Lett.* **B754** (2016) 235–248, [arXiv:1509.07324 \[nucl-ex\]](https://arxiv.org/abs/1509.07324).
- [238] **ALICE** Collaboration, R. Reed, “Full Jet Reconstruction in 2.76 TeV pp and Pb-Pb collisions in the ALICE experiment,” *J. Phys. Conf. Ser.* **446** (2013) 012006, [arXiv:1304.5945 \[nucl-ex\]](https://arxiv.org/abs/1304.5945).
- [239] **ALICE** Collaboration, G. Dellacasa *et al.*, “ALICE technical design report of the photon spectrometer (PHOS),” CERN-LHCC-99-04.
- [240] **ALICE** Collaboration, P. Cortese *et al.*, “ALICE electromagnetic calorimeter technical design report,” CERN-LHCC-2008-014, CERN-ALICE-TDR-014.
- [241] J. Allen *et al.*, “ALICE DCal: An Addendum to the EMCal Technical Design Report Di-Jet and Hadron-Jet correlation measurements in ALICE,” Tech. Rep. CERN-LHCC-2010-011. ALICE-TDR-14-add-1, Jun, 2010. <https://cds.cern.ch/record/1272952>.
- [242] **ALICE** Collaboration, P. Cortese *et al.*, “ALICE technical design report on forward detectors: FMD, T0 and V0,” CERN-LHCC-2004-025.
- [243] **ALICE** Collaboration, A. I. Maevskaya, “Fast Interaction Trigger for the upgrade of the ALICE experiment at CERN: design and performance,” [arXiv:1812.00594 \[physics.ins-det\]](https://arxiv.org/abs/1812.00594).
- [244] **ALICE Collaboration** Collaboration, *ALICE Photon Multiplicity Detector (PMD): Technical Design Report*. Technical Design Report ALICE. CERN, Geneva, 1999. <https://cds.cern.ch/record/451099>.
- [245] **ALICE** Collaboration, G. Dellacasa *et al.*, “ALICE technical design report of the zero degree calorimeter (ZDC),” CERN-LHCC-99-05.
- [246] A. Villatoro Tello, “Ad, the alice diffractive detector,” *AIP Conference Proceedings* **1819** (03, 2017) .
- [247] **ACORDE** Collaboration, A. Fernández *et al.*, “ACORDE a Cosmic Ray Detector for ALICE,” *Nucl. Instrum. Meth.* **A572** (2007) 102–103, [arXiv:physics/0606051 \[physics.ins-det\]](https://arxiv.org/abs/physics/0606051).

- [248] **ALICE** Collaboration, S. Beole *et al.*, “The forward muon spectrometer of ALICE,”.
- [249] **ALICE** Collaboration, M. Krivda, D. Alexandre, L. S. Barnby, D. Evans, P. G. Jones, A. Jusko, R. Lietava, J. Pospíšil, and O. V. Baillie, “The ALICE Central Trigger Processor (CTP) upgrade,” *JINST* **11** no. 03, (2016) C03051.
- [250] J. Král, *Intrinsic transverse momentum distribution of jet constituents in p-Pb collisions at ALICE*. PhD thesis, University of Jyväskylä, August, 2014. <http://urn.fi/URN:ISBN:978-951-39-5741-4>.
- [251] J. Kral, T. Awes, H. Muller, J. Rak, and J. Schambach, “L0 trigger for the emcal detector of the alice experiment,” *Nuclear Instruments and Methods in Physics Research Section A: Accelerators, Spectrometers, Detectors and Associated Equipment* **693** (2012) 261 – 267. <http://www.sciencedirect.com/science/article/pii/S0168900212007681>.
- [252] **ALICE Collaboration** Collaboration, B. Abelev *et al.*, “Upgrade of the ALICE Experiment: Letter of Intent,” Tech. Rep. CERN-LHCC-2012-012. LHCC-I-022. ALICE-UG-002, CERN, Geneva, Aug, 2012. <https://cds.cern.ch/record/1475243>.
- [253] A. Maevskaya, “Fast Interaction Trigger for the upgrade of the ALICE experiment at CERN: design and performance,” *EPJ Web Conf.* **204** (2019) 11003.
- [254] “Technical Design Report for the Muon Forward Tracker,” Tech. Rep. CERN-LHCC-2015-001. ALICE-TDR-018, Jan, 2015. <https://cds.cern.ch/record/1981898>.
- [255] F. Sauli, L. Ropelewski, and P. Everaerts, “Ion feedback suppression in time projection chambers,” *Nucl. Instrum. Meth.* **A560** (2006) 269–277.
- [256] **ALICE TPC** Collaboration, M. Ball, K. Eckstein, and T. Gunji, “Ion backflow studies for the ALICE TPC upgrade with GEMs,” *JINST* **9** (2014) C04025.
- [257] **The ALICE Collaboration** Collaboration, “Upgrade of the ALICE Time Projection Chamber,” Tech. Rep. CERN-LHCC-2013-020. ALICE-TDR-016, Oct, 2013. <http://cds.cern.ch/record/1622286>.
- [258] P. F. Little, *Secondary Effects*, pp. 574–662. Springer Berlin Heidelberg, Berlin, Heidelberg, 1956. [https://doi.org/10.1007/978-3-642-45844-6\\_9](https://doi.org/10.1007/978-3-642-45844-6_9).

- [259] M. Vargyas, *Jet shape modification in Pb-Pb collisions at  $\sqrt{s_{NN}} = 2.76$  TeV using two-particle correlations*. PhD thesis, University of Jyväskylä, November, 2018. <http://urn.fi/URN:ISBN:978-951-39-7610-1>.
- [260] **ALICE TPC upgrade** Collaboration, J. E. Brücken and T. E. Hildén, “The GEM QA Protocol of the ALICE TPC Upgrade Project,” in *5th International Conference on Micro Pattern Gas Detectors (MPGD2017) Temple University, Philadelphia, USA, May 22-26, 2017*. 2018. [arXiv:1811.07043](https://arxiv.org/abs/1811.07043) [physics.ins-det].
- [261] T. Hildén, E. Brücken, J. Heino, M. Kalliokoski, A. Karadzhinova, R. Lauhakangas, E. Tuominen, and R. Turpeinen, “Optical quality assurance of GEM foils,” *Nucl. Instrum. Meth.* **A770** (2015) 113–122, [arXiv:1704.06691](https://arxiv.org/abs/1704.06691) [physics.ins-det].
- [262] **ALICE** Collaboration, B. B. Abelev *et al.*, “Performance of the ALICE Experiment at the CERN LHC,” *Int. J. Mod. Phys.* **A29** (2014) 1430044, [arXiv:1402.4476](https://arxiv.org/abs/1402.4476) [nucl-ex].
- [263] **ALICE** Collaboration, K. Aamodt *et al.*, “Alignment of the ALICE Inner Tracking System with cosmic-ray tracks,” *JINST* **5** (2010) P03003, [arXiv:1001.0502](https://arxiv.org/abs/1001.0502) [physics.ins-det].
- [264] R. Fruhwirth, “Application of Kalman filtering to track and vertex fitting,” *Nucl. Instrum. Meth.* **A262** (1987) 444–450.
- [265] A. Maire, “Track reconstruction principle in ALICE for LHC run I and run II. Principes de reconstruction de traces dans ALICE pour les runs I et II du LHC.” General Photo, Oct, 2011.
- [266] **ALICE** Collaboration, B. Abelev *et al.*, “Measurement of Event Background Fluctuations for Charged Particle Jet Reconstruction in Pb-Pb collisions at  $\sqrt{s_{NN}} = 2.76$  TeV,” *JHEP* **03** (2012) 053, [arXiv:1201.2423](https://arxiv.org/abs/1201.2423) [hep-ex].
- [267] **ALICE** Collaboration, B. Abelev *et al.*, “Long-range angular correlations on the near and away side in  $p$ -Pb collisions at  $\sqrt{s_{NN}} = 5.02$  TeV,” *Phys. Lett.* **B719** (2013) 29–41, [arXiv:1212.2001](https://arxiv.org/abs/1212.2001) [nucl-ex].
- [268] M. Cacciari, G. P. Salam, and G. Soyez, “FastJet User Manual,” *Eur. Phys. J.* **C72** (2012) 1896, [arXiv:1111.6097](https://arxiv.org/abs/1111.6097) [hep-ph].
- [269] M. Cacciari, G. P. Salam, and G. Soyez, “The anti- $k_t$  jet clustering algorithm,” *JHEP* **04** (2008) 063, [arXiv:0802.1189](https://arxiv.org/abs/0802.1189) [hep-ph].

- [270] T. Sjöstrand, S. Mrenna, and P. Z. Skands, “A Brief Introduction to PYTHIA 8.1,” *Comput. Phys. Commun.* **178** (2008) 852–867, [arXiv:0710.3820 \[hep-ph\]](https://arxiv.org/abs/0710.3820).
- [271] G. Upton and I. Cook, *A Dictionary of Statistics*. 01, 2008. <http://www.oxfordreference.com/view/10.1093/acref/9780199541454.001.0001/acref-9780199541454>.
- [272] “Roounfold: Root unfolding framework.” <http://hepunx.rl.ac.uk/~adye/software/unfold/RooUnfold.html>, 2013. <http://hepunx.rl.ac.uk/~adye/software/unfold/RooUnfold.html>.
- [273] A. Hocker and V. Kartvelishvili, “SVD approach to data unfolding,” *Nucl. Instrum. Meth.* **A372** (1996) 469–481, [arXiv:hep-ph/9509307 \[hep-ph\]](https://arxiv.org/abs/hep-ph/9509307).
- [274] P. Z. Skands, “Tuning Monte Carlo Generators: The Perugia Tunes,” *Phys. Rev.* **D82** (2010) 074018, [arXiv:1005.3457 \[hep-ph\]](https://arxiv.org/abs/1005.3457).
- [275] R. Brun, R. Hagelberg, M. Hansroul, and J. C. Lassalle, *Simulation program for particle physics experiments, GEANT: user guide and reference manual*. CERN, Geneva, 1978. <https://cds.cern.ch/record/118715>.
- [276] R. Brun, F. Bruyant, F. Carminati, S. Giani, M. Maire, A. McPherson, G. Patrick, and L. Urban, “GEANT Detector Description and Simulation Tool.” [http://cds.cern.ch/record/1082634](https://cds.cern.ch/record/1082634).
- [277] **ALICE** Collaboration, S. Acharya *et al.*, “Jet fragmentation transverse momentum measurements from di-hadron correlations in  $\sqrt{s} = 7$  TeV pp and  $\sqrt{s_{NN}} = 5.02$  TeV p-Pb collisions,” *JHEP* **03** (2019) 169, [arXiv:1811.09742 \[nucl-ex\]](https://arxiv.org/abs/1811.09742).
- [278] Y.-T. Chien and I. Vitev, “Towards the understanding of jet shapes and cross sections in heavy ion collisions using soft-collinear effective theory,” *JHEP* **05** (2016) 023, [arXiv:1509.07257 \[hep-ph\]](https://arxiv.org/abs/1509.07257).